Summer 8-23-2019

Characterization of Nano-Cellulose Based Composites For Biomedical Applications

Mitchell P. Chesley
University of Maine, mitchell.chesley@maine.edu

CHARACTERIZATION OF NANO-CELLULOSE BASED COMPOSITES FOR BIOMEDICAL APPLICATIONS

By

Mitchell P. Chesley

B.S University of Maine, 2017

A THESIS

Submitted in Partial Fulfillment of the

Requirement for the Degree of

Master of Science

(in Biomedical Engineering)

The Graduate School
The University of Maine
August 2019

Advisory Committee:

Dr. Michael Mason, Professor of Biomedical and Chemical Engineering, Advisor

Dr. Paul Millard, Professor of Biomedical and Chemical Engineering

Dr. Mehdi Tajvidi, Assistant Professor of Renewable Nanomaterials

Dr. Ian Dicky, Orthopedic Oncologist at Colorado Limb Consultants in Denver, Colorado

CHARACTERIZATION OF NANO-CELLULOSE BASED COMPOSITES FOR BIOMEDICAL APPLICATIONS

By: Mitchell Chesley

Thesis Advisor: Dr. Michael D. Mason

An Abstract of the Thesis Presented
In Partial Fulfillment of the Requirements for the
Degree of Master of Science
(in Biomedical Engineering)
August 2019

The number of orthopedic surgeries performed globally has steadily increased over the past decade due to the standardization of procedures as well as technological advancements. During this time orthopedic devices have been composed predominantly of metals, such as Titanium, Vanadium, Molybdenum, and Stainless steel, as well as their alloys, due to the high strength and durability of these materials. However, metals may, in fact, be suboptimal for orthopedic devices. For example, metals exhibit Young's modulus much greater than the surrounding bone, inducing localized stress-shielding promoting cortical atrophy, which can lead to osteoporosis. In recent years polymers have been successfully explored as a potential substitute for metals in non-load bearing locations. Some of these polymers were designed to be bio-absorbable overtime. Unfortunately, this chemical breakdown results in local acidification, which can leach into proximal bone, causing demineralization and weakening of the surrounding bone, along with increased degradation of the implant itself. In other cases, the resorbed device leaves a "mushy" non-calcified mass that is never fully regrown as a structural bone.

Our proposed solution is a cellulose nanofibril (CNF) composite-based platform material for non-load bearing surgical devices (plates, pins, screws). This composite has the potential to be safely bio-resorbable while providing sufficient stiffness during initial implantation, eventually softening overtime promoting the natural formation of strong bone. The method of making composites is adaptive allowing a host of material additives to be introduced during the CNF formation process.

Physical properties of the produced composites were analyzed and compared, in particular, flexural modulus, porosity, and Shore D hardness. Which are the primary physical assessments for many orthopedic devices and materials. Additionally, the use of ceramic synthesized biomimetic hydroxyapatite was used in making composites of CNF, this potentially adding a degree of osteoinduction to the CNF. Lastly, aqueous degradation of CNF was monitored and recorded in two separate tests, long period and short hour periods. Flexural modulus, water content increase, volume increase, and Shore D hardness was measured for all samples, with the material loss being monitored solely with long period testing. For use in material degradation, an apparatus was established and utilized for long term testing. Short term testing demonstrated initially drier specimens resistances to water gain, volume gain, and flexural decay over hydrated specimens which showed less resistance to all three parameters. Long term trials displayed the longevity of the materials in an aqueous solution with minimal material loss, however, specimens had high flexural decay, water gain, and volume gain after 24 hours. Recent results and recommendations are presented.

ACKNOWLEDGMENTS

First and foremost, I would like to thank my advisor Dr. Michael Mason for allowing me to partake in such an influential project, and for giving me the experience needed to continue in the research field. I would also like to thank him for the enthusiasm and encouragement he has given me throughout these challenging years. I give thanks to Dr. Paul Millard, Dr. Mehdi Tajvidi, and Dr. Ian Dicky, who have given me insight into the many different aspects of researching materials for biomedical engineering. I also am grateful for everyone in my research group who has helped me and supported me through my graduate career. I would also like to thank David Holomakoff for setting the groundwork for this project and for mentoring me during the beginning of my scientist career.

I would like to acknowledge all the friends and family who have supported me throughout this endeavor, especially my mother and father who helped me push myself past any boundaries that have been placed in front of my path and encouraging me to achieve my pursuits.

TABLE OF CONTENTS

LIST OF TABLES

LIST OF FIGURES

LIST OF ABBREVIATIONS

BM - Ball Milled

BMP - Bone Morphogenic Proteins

CNF - Cellulose Nano-fibrils

DL-PLA - Poly (D, L-Lactic Acid)

FTIR - Fourier Transform IR Spectrometry

HA - Hydroxyapatite

NPs - Iron oxide nanoparticles

PLA - Poly(Lactic Acid)

PGA - Poly(Glycolic Acid)

PLLA - Poly(L-Lactic Acid)

PDLA - Poly (D-Lactic Acid)

SEM - Scanning Electron Microscopy

XRD - X-ray Diffraction

Wt% - Weight Percent

CHAPTER 1

INTRODUCTION

The number of orthopedic surgeries performed globally has steadily increased over the past decade due to the standardization of procedures as well as technological advancements. During this time orthopedic devices have been composed predominantly of metals, such as Titanium, Vanadium, Molybdenum, and Stainless steel, as well as their alloys, due to the high strength and durability of these materials. However, metals may, in fact, be suboptimal for orthopedic devices. For example, metals exhibit Young's modulus much greater than the surrounding bone, inducing localized stress-shielding promoting cortical atrophy, which can lead to osteoporosis. In recent years polymers have been successfully explored as a potential substitute for metals in non-load bearing locations. Some of these polymers were designed to be bio-absorbable overtime. Unfortunately, this chemical breakdown results in local acidification, which can leach into proximal bone, causing demineralization and weakening of the surrounding bone, along with increased degradation of the implant itself. In other cases, the resorbed device leaves a "mushy" non-calcified mass that is never fully regrown as a structural bone.

Our proposed solution is a cellulose nanofibril (CNF) composite-based platform material for non-load bearing surgical devices (plates, pins, screws). As CNF has been shown to be memetic in collagen flexural moduli, it is suitable to use as a substitute for this abundant fibrous matrix within natural bone. This composite has the potential to be safely bio-resorbable while providing sufficient stiffness during initial implantation, eventually softening overtime promoting the natural formation of strong bone. The method of making composites is adaptive allowing a host of material additives to be introduced during the CNF formation process.

Physical properties of the produced composites were analyzed and compared, in particular, flexural modulus, porosity, and Shore D hardness which is the primary physical assessment for many orthopedic devices and materials. Within Chapter 2 background of human bone anatomy, healing, and function is explained. Chapter 3 explores mineral oxide composites and suspensions, while Chapter 4 explores the physical properties of these composites. Mechanical mixing manipulation of CNF is shown in Chapter 5. The use of synthesized ceramic biomimetic hydroxyapatite was used in composites of CNF, potentially adding a degree of osteoinduction to the CNF and increased mechanical properties are investigated in Chapter 6. Lastly in Chapter 7, aqueous degradation of CNF was monitored and recorded in two separate tests, long period and short hour periods. Flexural modulus, water content increase, volume increase, and Shore D hardness was measured for all samples, with the material loss being monitored solely with long period testing. For use in material degradation, an apparatus was established and utilized for long term testing. Recent results and recommendations are presented.

CHAPTER 2

LITERATURE REVIEW

2.1 Introduction

2.1.1 Human Bone

The adult human skeleton has a total of 213 bones, separated into 126 bones in the appendicular skeleton, 74 axial skeleton bones, and six auditory ossicles bones[1]. The human body is comprised of 80% cortical bone and 20% trabecular bone[1]. Bone mass is comprised of 50-70% mineral content with the majority of the mineral being hydroxyapatite (HA $Ca_{10}(PO^4)_6(OH)_2$) which is a naturally occurring bone mineral, 20-40% is collagen (primarily Collagen type I), and 5-10% water[1–4]. Up to 8 percent of HA found in bone is found in the form of carbonated hydroxyapatite (CHA)[1,5,6], along with some other trace minerals such as magnesium and acid

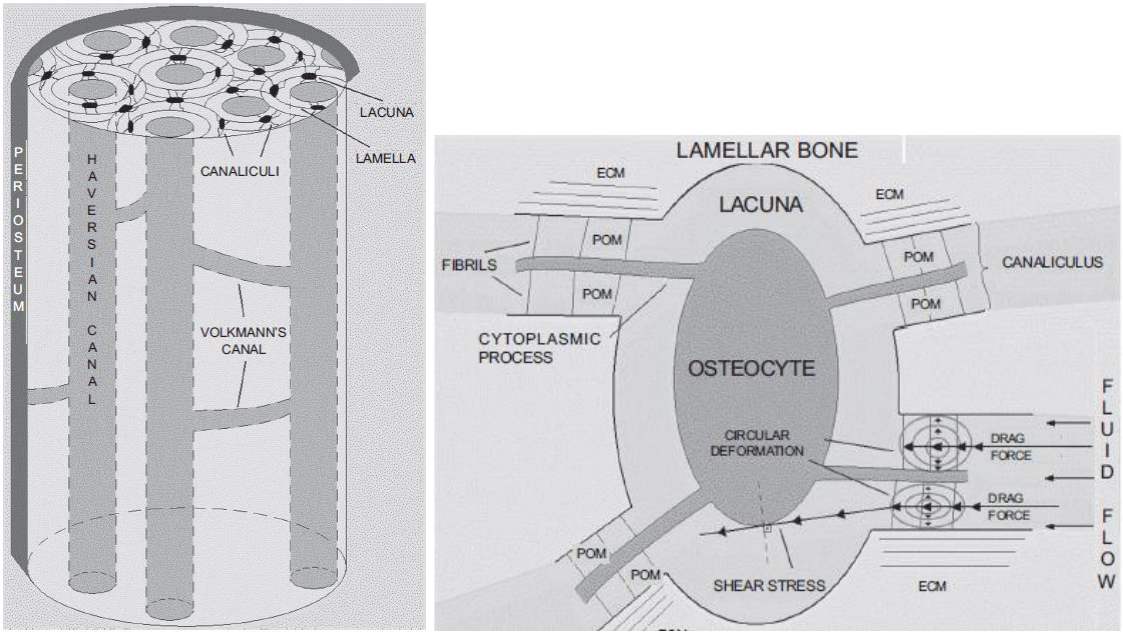

Figure 2.1: Interior structure of bone (left), image of fluid flow and interaction with osteocyte(right), from ref (7)

phosphate[1]. HA provides mechanical rigidity and load-bearing strength to bone, whereas collagen provides elasticity and flexibility[1,7].

Bones consist of two parts, cortical bone and trabecular bone, which are both roughly comprised of a similar ceramic polymer composite as described above[1,3]. Cortical bone primary structural unit is an Osteon, also known as a Haversian system. Osteons consist of cylindrical shaped lamellar bone that surrounds channels called Haversian canals. Cortical Osteons provides its stiffness and rigidity depending on the tight packing of the cortical Osteons. Cortical bone has an outer periosteal surface and an inner endosteal surface, periosteal surfaces activity is important for apatite growth and fracture repair. Endosteal surface is responsible for higher remodeling activity when compared to periosteal surfaces, as it is in contact with bone marrow space, trabecular bone, and blood vessel canals[1].

Both cortical and trabecular bone are normally found in a lamellar pattern in which collagen fibers are laid down in alternating orientations, which has been shown to provide significant strength[1]. While cortical bone is dense and stiff, trabecular is bone porous and less dense. Trabecular bone is composed of plates and rods trabecula that form a network in between long bone, which facilitates the space for blood vessels and red bone marrow as well as provides additional structural support[1,7]. Trabecular bone also has a high turnover rate, which is higher than required for maintenance of mechanical strength indicating that turnover rate of trabecular bone is important for mineral metabolism and can possibly explain trabecular bones lower tissue density when compared to cortical bone[1,3].

Throughout bone cylindric networks called Haversian canals can be found. When bone experiences stress or strain through everyday activity it deforms and creates a pressure gradient throughout, this results in a fluid flow within the pericellular space of cytoplasmic processes

resulting in drag forces[8,9]. These drag forces then cause shear stress on osteocytes within the canals as displayed in Figure 2.1 from ref 7. Osteocytes, which make up about 90-95% off all bone cells[9], are then the primary mechanosensory cells of the bone. Osteocytes use extracellular membrane receptors such as integrins and CD44 receptors as mechanotransducers[8], osteocytes then direct osteoblasts and osteoclasts in bone remodeling[8,9].

Along with osteocytes, proteins are involved with bone growth such as bone morphogenic proteins (BMP). BMP-2 acts as a disulfide-linked homodimer and induces bone and cartilage formation. It is a candidate mediator and plays a key role in osteoblast diffraction. BMP-7 plays a key role in osteoblast differentiation. It also induces production of SMDAI. Also, key in renal development and repair[10]. Additionally, BMP-4, -5, -6 also how the greatest osteogenic capacity. BMP-4 regulates the formation of teeth, limbs, and bone from mesoderm, as well as plays a role in fracture repair. BMP-5 performs functions in cartilage development. BMP-6 key role is in joint integrity in adults[10]. BMP-2 and BMP-7 have been shown to have significant importance in bone development and the development of a wide array of tissues outside of bone[10].

When a traumatic bone injury such as a break, occurs, a complex process of healing event results. Bone growth and healing occur over a period of 3 to 6 months post-injury. The 1st two weeks of bone healing is critical due to inflammation and revascularization that occurs. Proceeding the inflammation stage, the repair stage begins. This stage involves fibroblasts laying down a stroma that supports vascular ingrowth. Within the first 4 to 6 weeks of healing the callus is very weak in terms of movement, hence an adequate form of protection such as a brace and or an internal fixation is typically used. Finally, fracture healing is completed during the remodeling stage, this stage is where the bone is restored to original shape, structure, and mechanical properties.

Remodeling of bone occurs over a slower period, preceding over months to years, this process is facilitated by mechanical stress placed on the bone[7].

After bone healing, normal mechanical properties of cortical and trabecular bone are re-established. However, discrepancies in flexural modulus can be found throughout literature, as such normal bone growth stiffness over time is approximated within each healing stage. With inflammation stage possessing the lowest moduli due to the weak callus, into a higher modulus within repair stages as more collagen is placed down and mineralized overtime until bone begins remodeling based off stimuli responses. These discrepancies are mainly due to testing methods, samples conditioning (wet or dry), and location of testing specimens. Trabecular bone has been reported to be in the range of 0.76-20 GPa for Youngs modulus[11–14]. This range is established using three-point bending, ultrasonic testing, tensile testing, and nanoindentation with overestimation occurring when fully drying bone material[11–14]. While cortical bone has Young's modulus range of 10-30 GPa[11–14], acquired through similar testing methods as trabecular bone.

2.1.2 Medical Implants and Biomaterials

Over the past century, advancements in technology have reached new heights never thought possible. One such advancement is that of biomaterials and implants. Orthopedic devices range from standard bone fixation plates and screws to total joint replacement devices. The main purpose of fixation devices is just that, to fix bone together at the fraction site and reduce movement to facilitate proper healing. As movement can disrupt healing within the first month due to soft callus and vascularization taking place. Therefore, ideal fixture devices should be made with certain characteristics, which promote bone healing as well as long term function. These properties include osteoinduction, osteoconduction, biocompatibility, corrosion-resistant, initial mechanical stiffness, and mechanical decay.

Biomaterials are a classification of materials with the intention of being integrated with biological systems. When developing a new biomaterial certain parameters must be met; first and foremost the material should exhibit a reasonable amount of biocompatibility. Biocompatibility can be defined in a multitude of ways, however, some of these definitions fail to address the key aspects associated with the term. The official definition comes from the consensus that "biocompatibility is the ability of a material to perform with an appropriate host response in a specific application"[15]. This definition holds true when considering current materials used within orthopedics and the medical field[16]. Orthopedic (the branch of medicine pertaining to correcting deformities of bones and muscles) devices should display osteoinductive and osteoconductive properties, to facilitate bone regeneration around and in most cases throughout the orthopedic device.

Mechanical decay over time beneficial for bone growth, as this enables bone to regain their stimulus needed during bone remodeling to form healthy strong bone. The timeline of an optimum bioabsorbable orthopedics mechanical degradation (flexural modulus) vs bone regeneration is displayed in Figure 2.2. Initially, orthopedics should have elevated moduli when compared to load-bearing cortical bone, in order to keep bone immobilized during the beginning stages of bone healing. As this is within the inflammation stage, vascularization is taken place with bone exhibiting low stiffness, with collagen being laid down while octoid is secreted and mineralized to form a soft callus around the repair site[7]. Following these 2 weeks, during the repair and remodeling stage (over 10 weeks), a dramatic drop in fixation stiffness followed by a prolonged drop is observed. After 20 weeks healed bone begins to exhibit modulus similar to that of load-bearing cortical bone due to ossification of the callus[7], as such fixation devices modulus become

irrelevant and devices can degrade over time while maintaining a structure for cells to proliferate through and grow.

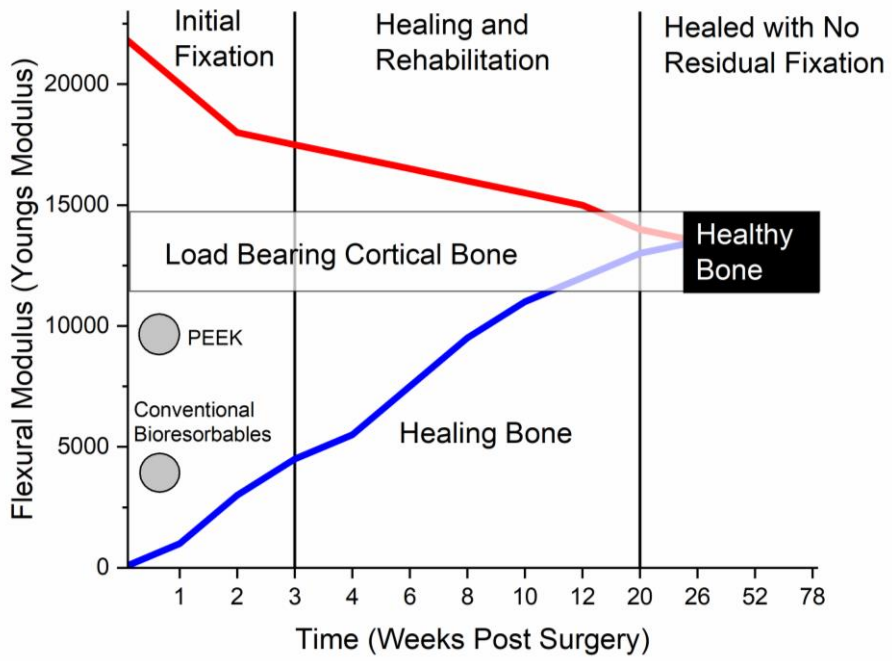

Figure 2.2: Optimum bioabsorbable bone fixation plate degradation vs. bone healing

Commonly used orthopedics devices for bone fixation plates and screws primarily consist of metals. However, current orthopedics do not go without their series of flaws. Metallic orthopedics used are alloys such as stainless steel 613L (205-210 GPa), CoCrMoF75 (220-230 GPa), Ti4Al6V (110 GPa)[17–22], and Nitinol (20-113)[17,19,23]. All of these are exceedingly stiff when compared to natural human trabecular (average 13.4 GPa) and cortical bone (average 22.5 GPa)[12,16]. Comparison between ideal bone healing and metallic fixations flexural modulus difference and known total strength loss and degradation of materials are shown in Figure 2.3 and Table 2.1, respectively. As literature focuses mainly on metallic orthopedic immune response, adequate data on bone healing while fixed with a metallic fixation is scarce to find, and in many cases, proprietary information for companies. As such a normal bone healing under preferred conditions is used, in which bone gradually heals within 26 weeks, regaining cortical bones

mechanical properties. Again, the ideal situation for a bioabsorbable fixation degradation rate is displayed alongside metallic orthopedics. Initially starting at sufficient stiffness then sharply decreasing in fixation flexural moduli, before beginning a slow decay of flexure over multiple months.

From stiffness displayed that are significantly higher than normal bone, some reaching 100

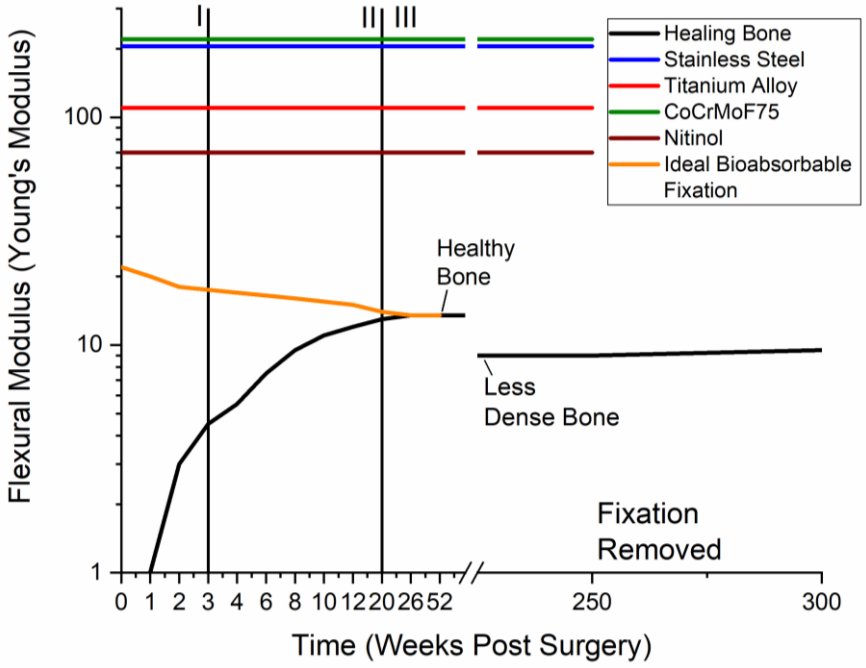

Figure 2.3: Metallic orthopedic materials vs bone healing. I) Initial Fixation, II) Healing and Rehabilitation, III) Healed bone

times higher. There is a potential that overtime localized atrophy of bone can occur through means of localized stress shielding. This consequently can lead to inflammation, potential aseptic loosening of the implant, and secondary surgery removal of devices[17,24,25]. Additionally, if these materials yield due to the stress subjected to them, catastrophic failures can occur through fixation breaks[26–29]. These failures can cause significant injury to the host, along with added infection and leaching of material into the surrounding tissue. Corrosion of the metallic materials can also occur, mainly through electrochemical dissolution phenomena, and wear or synergistic combinations of the two. This can further decrease the integrity of the implant and potentially elicit an adverse

effect on the surrounding tissue[16,27,29,30]. As such, the tendency with many metallic orthopedics is a secondary operation to remove the metal device, due to either device failure or personal preference of the patient[31].

In a study performed by Kadir B.M.D *et al.*[32] on patients post orthopedic operations over a five-year period from 2007 to 2011 found that 44 patients had metallic hardware removed. Among these, the most common hardware location was the femur (54.2%), followed by the radius (20.8%), tibia (16.7%), and ankle (8.3%). 54.2 percent of all hardware removed were: fixation plates and screws. Indications leading to the removal were the following, infection (41.7%), patient's request (25%), hardware failure (12.5%), pain (12.5%), surgeons decision (4.2%), and incorrect hardware placement (4.2%)[32]. The potential end result of metal fixation removal is exhibited in Figure 2.3 where the Young's modulus of bone decreases after time to a level below that of normal load-bearing cortical bone. However, there is the potential for the bone to regain its strength after fixations removal due to regular use and stress applied to the bone required for bone remodeling.

Table 2.1: Orthopedic materials flexural modulus vs degradation/strength loss

Material	Flexure Modulus (GPa)	Loss of strength (Months)	Degradation of material (Months)
Bone	10-40	NA	NA
Stainless Steel	180-205	NA (Unless fixation break)	NA
Titanium Alloy	110-127	NA (Unless fixation break)	NA
CoCrMoF75	220-230	NA (Unless fixation break)	NA
Nitinol	20-130	NA	NA
PGA	7	1	6-12
PLLA	2	3	>24

Plastic orthopedics devices have been making headway into many orthopedic applications. Devices made from these materials are used primarily for non-load bearing operations and provide

a biodegradability aspect to orthopedics. With many of these devices, the degradation rate is known to be precipitated. Failure of mechanical properties occurring typically before full recovery of bone, along with local acidic decalcification brought by the cleavage and excretion of acid from the plastic as it breaks down[17,31,33–35]. Degradation of the plastic fixation is primarily facilitated by nonspecific hydrolytic scission of ester groups. Fixations devices that are less porous have been shown to increase the degradation rate of fixations due to its inability to expel acidic breakdown due to the hydrolysis[31]. This increase in acidic byproducts within the fixation results in an increase of degradation of the bulk material through byproducts interacting with carboxylic end groups which act as autocatalysts[17,35,36].

Additionally in the first two weeks of implantation into hard tissue pH decreases to ~5.2 before reestablishing to 7.4 causing further increased degradation[30]. Most commonly used plastics for orthopedics are Poly(Glycolic Acid) (PGA), and Poly(Lactic Acid) (PLA). With different isomers of PLA being created such as, L-PLA (mostly crystalline), D-PLA and DL-PLA which is mostly amorphous and leads to increased sensitivity to hydrolysis[31]. Another commonly practiced bioabsorbable is a copolymer between PGA and PLA. As the modulus of PGA is known to be high about 13 GPa, however, PGA degrades fast in aqueous solutions[36,37]. PLA and its isomers possess low flexural modulus but exhibit prolonged stability in aqueous solutions. These properties lead to further developments of these PLA and PLA isomers with PGA. Thus, combines the modulus of PGA with the longevity of PLA and its isomers. Consequently, with this copolymer issues are still noticed when degradation of the device does occur, mainly from leaching and accumulation of acids into the surrounding environment[17,35,36].

2.1.3 Cellulose Nano-Fibril

Cellulose-based materials are gaining attention as candidate materials for a host of biomedical applications. These include soft-tissue implants and cartilage replacement, tissue engineering, antibacterial/ antimicrobial activity, cardiovascular, cancer-targeting, cornea replacement, biological detection, and biology-device interfaces[38]. Unlike other materials, which are thermoplastics held together by molecular entanglement, CNF materials are held together by a combination of entanglement and hydrogen bonding between cellulose fibrils and can include short- and long-range order fibers.

Cellulose is comprised of ß-1,4-linked D-glucopyranose rings, monomer units are arranged in a way that glucosidic oxygens occur in opposite directions. Repeating units of the cellulose chain are made up of two ß-D-glucopyranose rings rotated with respect to each other to form a cellobiose unit. As a result of equatorial-equatorial glycosidic linkage, cellulose chains have units positioned so adjacent rings can form hydrogen bonds between rings oxygen atoms of one glycosil unit and the hydrogen of the C-3 hydroxyl group of the receding ring. The presence of many

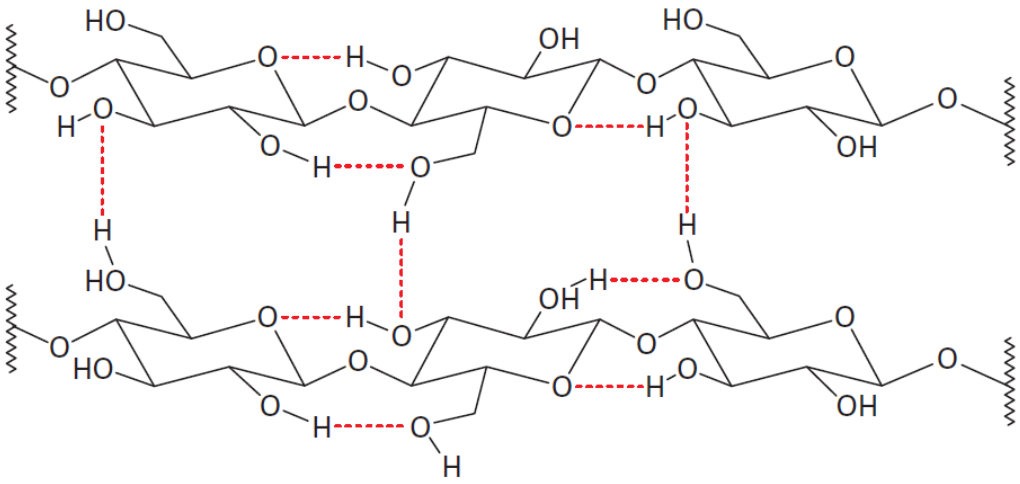

Figure 2.4: Schematic of intra and intermolecular hydrogen bonds from ref (34)

hydroxyl groups along the chains results in the formation of a network of intra- and intermolecular hydrogen bonds, along with a network of van der Walls connections established between the chains layers[39]. Hydrogen bonding both intra- and intermolecular can be seen in Figure 2.4.

Cellulose Nano-Fibrils (CNF) is relatively new abundant platform material with a plethora of use such as filtration and separation membranes, oil separation from water, drug delivery, wound dressing, sensors[40], and numerous other biomedical applications[38,40–42]. As such the research into this naturally abundant polymer has become commonplace in the scientific community. CNF can be derived from numerous sources such as bast fibers (flax, hemp, jute, ramie, *etc.*), grasses (bagasse, bamboo, *etc.*), seed fibers (cotton, coir, *etc.*), wood (hardwood, and softwood), marine animals (tunicate, algae, fungi, invertebrates, and bacteria[43]. Generally, production of CNF uses a mechanically induced breakdown strategy involving high-pressure homogenization and/ or grinding before and after chemical or enzymatic treatment[41].

CNF based on its sources is inherently biodegradable and hydrophilic. It has also been shown in recent studies that CNF displays low cytotoxicity and high biocompatibility[38,41,42] which is a keystone to the material being researched for biomedical applications. Additionally, the structure of CNF is structurally similar to that of collagen found in bone. A comparison of CNF and other collagen substitute materials is shown in Table 2.2.

Table 2.2: Materials source, structure, positives & negatives

Type	**Source**	**Structure**	**Pro**	**Con**
Collagen	Natural	H-bonded Triple helix	Strong but flexible No inflammation Hydrophilic, compatible with biominerals	Costly excepts where it already exists
Acellular Collagen[44]	Biological Collagen	Triple helix Aggregation of fibers.	De-cellularized collagen Preferred material use	Time consuming process of production demineralized
Alginate[45–47]	Brown algae Ionically linked or covalently linked	Copolymer cross-linked fibers	Abundant, cheap Easy to manipulate Can be crosslinked	Low mechanical properties Low dimensional stability Limited cell attachment
Chitin[48–50]	Arthropods Exoskeleton Cell wall of Fungi and Yeast	Linear polymer of amino sugar	Non-toxic Antibacterial Biodegradable Biocompatible Second abundant polymer	Inherently low mechanical properties Require mechanical improvement through materials (HA, Bioactive Glass)
CNF	Plant-based cellular walls	Mono polymer cross-linked hydrogen fibers	Most abundant polymer Antibacterial Biodegradable Biocompatible Hydrogen bond-related degradation	Not been study for orthopedic applications Strength, time properties not known

From compared materials, CNF presents itself as a suitable polymer to investigate for potential orthopedics application, due to its abundance, fibrous morphology, and tunable mechanical properties. Access to abundant amounts of material allowed for multiple testing

specimens to be made at a relatively rapid pace, providing reliable results per test. Fibrous structure and tunable surface hydroxyl groups allowed for chemical modification and integration of minerals to CNF. Along with its known biocompatible traits, CNF is known to break down in aqueous solutions due to disruption of intra and intermolecular hydrogen bonds of CNF by water. This degradation would make it ideal within bioabsorbable fixations as there would be no byproducts related to the passive degradation of CNF.

2.1.4 CNF Manufacturing Process

Previous work performed by Holomakoff *et al.*[51] explored many different de-watering techniques of the CNF. All methods used a similar mold with a ceramic microporous brick system to allow capillary action. Ambient drying and accelerated drying using an industrial convection oven to facilitate drying were used to dewater the CNF.

Figure 2.5: Ridged foam CNF vial lyophilization

The mechanical properties of CNF were evaluated such as Young's Modulus, compression, and tensile, following the drying process. Previously CNF specimens were medially porous and mainly smooth due to the flow of material during reduced manufacturing. Additionally, bulk specimens

of CNF were manufactured with the capacity of being highly porous with low density, via a lyophilization process seen in Figure 2.5. With many low-density CNF displaying flexural modulus within the range of trabecular bone as displayed in Figure 2.6.

From previous and patented (WO201765465A1[52]) work performed dewatering methods of CNF have been explored, with the most effective method being a ceramic mold system utilizing convection oven for expedient drying. However, with current drying molds flaws were discovered

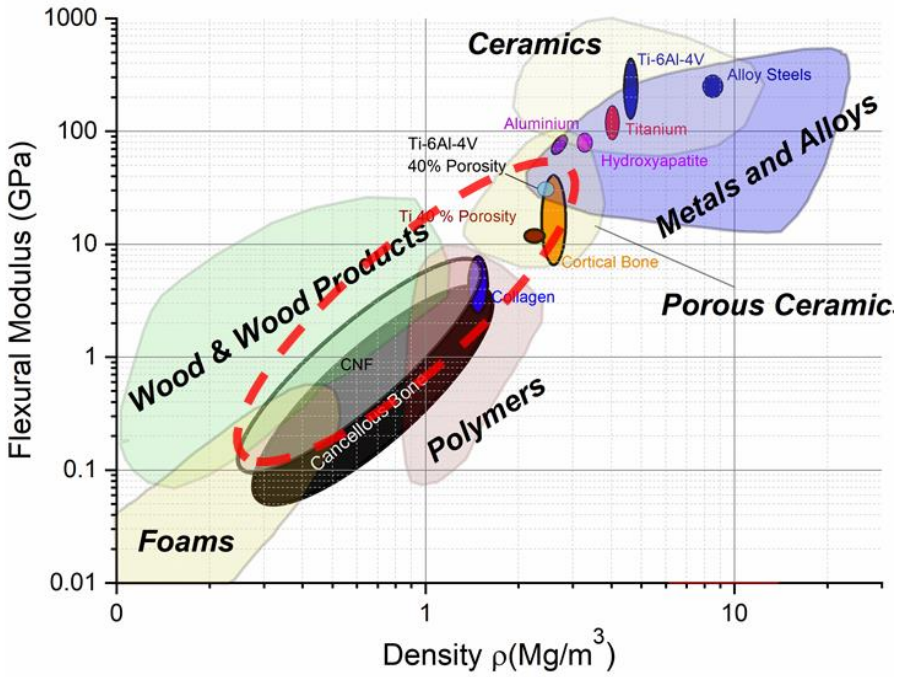

Figure 2.6: Ashby plot of materials, with subset of materials used in orthopedics. Red outline projected modulus after composite addition

and addressed. Overextended use, ceramic brick material deteriorated preventing proper friction to be formed between bricks. With the addition of CNF into the molds, this would consequently allow the bricks to be kicked out, spilling a large amount of the CNF housed inside. This was solved with the addition of a small aluminum bar across the bottom of the molds. This effectively prevented the bricks from shifting, minimizing loss of CNF material.

Owing to the demand for bone healing techniques and devices, and the limitations of current materials used for said techniques and devices. CNF presents its self as a suitable material to investigate with intentions to be used in orthopedic medicine. As the CNF is structurally similar to that of collagen, including the ability to incorporate minerals, the ability to form pores for biology integration, and the potential to degrade and go away over time, the viability of this material for bone healing should be investigated. Which is done in this thesis presented. Specifically, the physical properties of CNF and CNF mineral composites are explored with the express purpose of characterizing CNF for use as a bioabsorbable orthopedic device.

CHAPTER 3

CELLULOSE NANO-FIBRIL BASED COMPOSITE MANUFACTURING

3.1 Cellulose Nano-Fibril/ Mineral Oxide Composites

3.1.1 Prevalence for Mineral Composites Cellulose Nanofibers

With considerations of previously designed orthopedics and a basic understanding of additive strengths of composite materials, mineral oxide material composites were investigated. Minerals chosen were done so from Figure 2.3, which also corresponded to currently used minerals within orthopedics. Mineral oxides chosen were titanium dioxide (TiO_2), silicon dioxide (SiO_2), iron oxide (Fe_2O_3), and aluminum oxide (Al_2O_3). The initial theory for the use of metal oxide nanoparticles was to use them as "boiling chips" within the CNF, as metals and ceramics would heat faster than surrounding CNF, thereby producing locations with a higher volume of air pockets. These air pockets would create a network of macro and nanopores voids within the CNF bulk when dried. This is ideal for their inevitable use within the orthopedic field because it allows cell proliferation into the device and promotes a scaffolding into which cells can differentiate. Additionally, mineral oxides possess oxygen which can be utilized for hydrogen bonding to the CNF, which allows for the easy passive implementation of materials into the CNF matrix. For the preliminary study of CNF composites mixtures were previously manufactured by hand, however, this procedure leads to human error and inconsistent samples that were not reliable for use when tested. To mitigate this an industrial mechanical mixer (Hobart Model: H600T) was implemented, with a whisking attachment to provide proper mixing of the viscous CNF.

3.1.2 Iron Oxide/CNF Composite

CNF's biologically favorable mechanical properties, apparent cellular ambivalence and non-cytotoxicity[53–55], and the biocompatiblity[55] suggests capabilities and characteristics that are typically seen in biomedical plastics. However, a possible medical concern of CNF medical devices is the ability to image the CNF structure while *in vivo*. A proposed solution to this complication is the use of ferromagnetic iron oxide nanoparticles (γ-Fe_3O_2). Iron oxide nanoparticles (NPs) are a recently used colloidal technology within the biomedical field. Common applications consist of magnetic cell labeling, separation, tracking, drug delivery, diagnostics i.e. contrast agent for magnetic resonance imaging (MRI)[56–58], tissue repair, hyperthermia, and mafnetofection[57].

With the addition of NPs into the CNF system, proper contrasting could be achieved and as a result. MRI and X-ray imaging could now be an effective method for monitoring dissolution characteristics *in vivo* and condition of devices, which includes possible failures or complications that could occur with the composite material over time. NPs were synthesized using a coprecipitation technique from a modified procedure from Kunz *et al* [59] This used Iron (II) Chloride Tetrahydrate and Iron (III) Chloride Hexahydrate with ammonia dropwise, added under nitrogen gas. This was then separated using a magnet, attracting the nanoparticles to the bottom of the flask allowing the top waste layer to be decanted. After decanting, 2M nitric acid and ferric nitrate were added to the co-precipitate and the solution is again placed under nitrogen and refluxed at 90°C with a condenser for an hour. The solution is then magnetically separated and decanted again before it is washed with separate 2M nitric acid and acetone wash steps. Once the final wash solution is decanted, the nanoparticles are finely dispersed in deionized water (DI). The suspended

nanoparticle system is measured for pH and particle size using a pH probe and dynamic light scattering method (DLS), respectively.

3.2 Materials

3.2.1 Iron Oxide Nanoparticles

Sample Name:	iron 0827 3		
SOP Name:	mansettings.nano		
File Name:	iron 0827.dts	**Dispersant Name:**	Water
Record Number:	3	**Dispersant RI:**	1.330
Material RI:	2.23	**Viscosity (cP):**	1.0031
Material Absorbtion:	1.00	**Measurement Date and Time:**	Monday, August 27, 2018 3:22:47 PM

Temperature (°C):	20.0	**Duration Used (s):**	75
Count Rate (kcps):	157.4	**Measurement Position (mm):**	0.45
Cell Description:	Low volume disposable sizing cuv...	**Attenuator:**	7

			Diam. (nm)	% Volume	Width (nm)
Z-Average (d.nm):	46.71	**Peak 1:**	26.65	98.2	13.00
PdI:	0.348	**Peak 2:**	342.1	1.8	154.9
Intercept:	0.967	**Peak 3:**	0.000	0.0	0.000
Result quality :	Good				

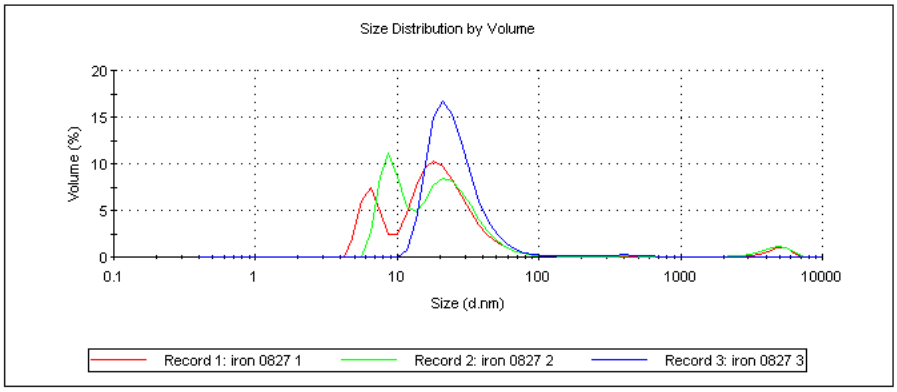

Figure 3.1: Dynamic Light Scattering Measurement of Synthesized Iron NPs Size Distribution vs Volume Percent

For use in this experiment, the size of the synthesized NPs system ranged from 10-40 nm in diameter. With the clear majority of the particles residing around the 20 nm range (Figure 3.1), particles were synthesized via coprecipitation method and dispersed in DI for storage. After storage, the pH was measured resulting in an average pH level of 3. The Zeta potential of NPs

suspended in DI of various pH (2-12) was measured using a Zetasizer (Model: Zen360) as seen in Figure 3.2. It was observed that a pH of 4 resulted in the greatest average positive Zeta potential within the colloidal system, while the greatest negative value was observed at a pH of 10. No

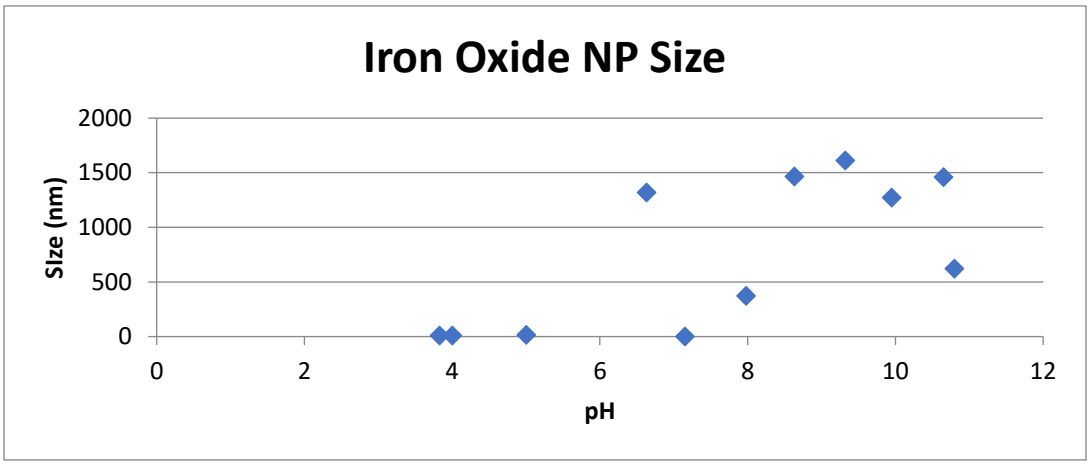

Figure 3.2: Iron Oxide NP size at different pH levels

observed changes in Zeta values occurred above and below values of 12 and 3, respectively, as the pH of solution ceased to have a significant effect on NPs surface charges.

Utilizing the Zetasizer once more, the same NPs samples were sized using dynamic light scattering (DLS), monitoring for particle aggregation and instability (Figure 3.3). Starting at a pH of 4 particle sizes were considerably small, as the pH is increased the size of particles increase due to the aggregation of the particles. Aggregation is caused by changes in surface charge of the NPs, therefore, at low pH values, particles are highly charged preventing them from aggregating due to the repulsiveness of the particles. As the pH increases the effective surface charge of the NPs decrease weakening the repulsion forces of the iron NPs[60]. When a pH of 10 is applied particle size is slightly re-established, however, the degree of size increase produces NPs that are 30 times

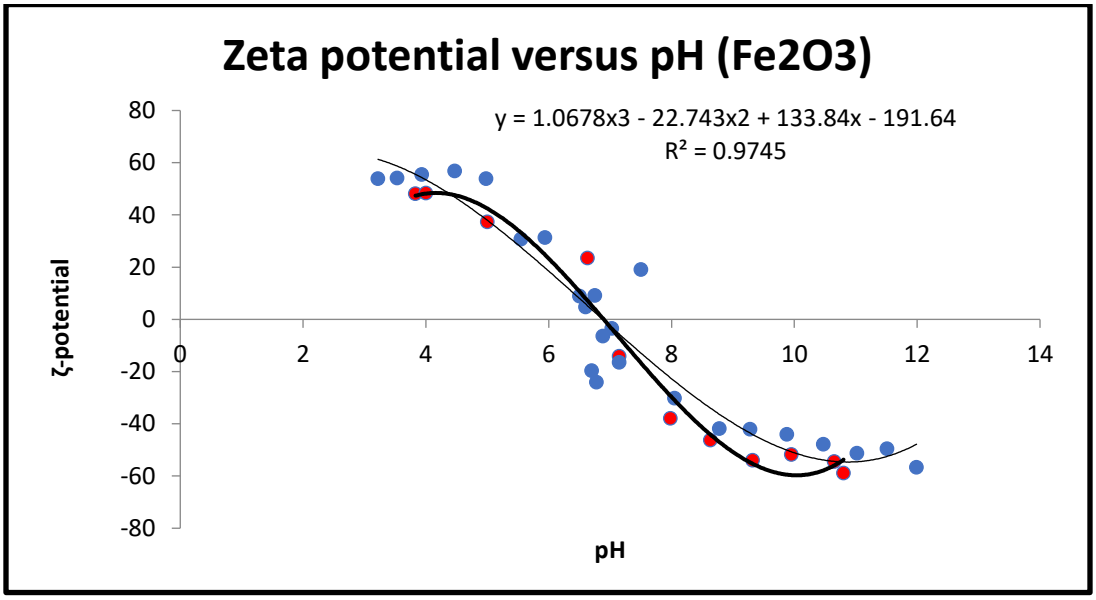

Figure 3.3: Zeta potential vs pH (Iron Oxide NPs)

bigger than NPs at pH 4. This could be because the surfaces of the nanoparticles reestablish their high positive charge resulting in some repulsion of other NPs[60].

To further characterize particle size and morphology, Transmission Electron Microscopy (TEM) was performed on the NPs with a Philips CM10 TEM at 13.5kX and 180kX magnification, the results can be seen in Figure 3.4. Particles were dispersed in DI at a concentration of 1:800. Observed particle diameters were primarily dispersed within the range of 10-20 nm.

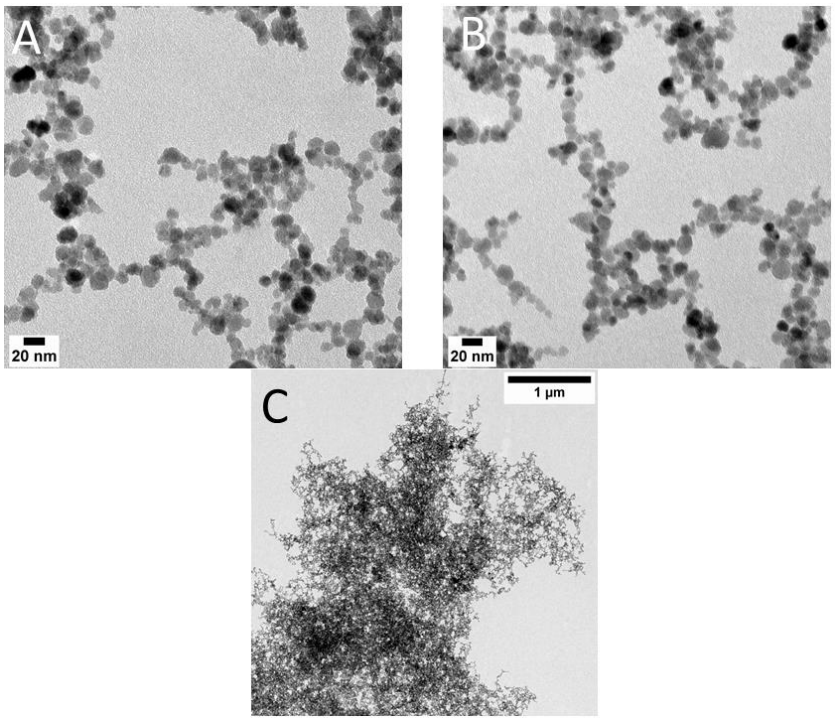

Figure 3.4: TEM imaging of two different locations of Iron Oxide samples.
180Kx (scale 20 nm) (A, B), larger section of Iron NPs 13.5kX (C)

3.2.2 Cellulose Nano-Fibrils

CNF was obtained from the Process Development Center (PDC) at the University of Maine. The obtained CNF is a 3-weight percent (Wt%) aqueous suspension, which we commonly call a "slurry", of cellulose proceeding mechanical break down into nanofibrils (<200 nm diameter) via a supermasscoloider. The end resultant material displays a wide range of characteristics depending on methods of dewatering. For example, freeze-dried CNF creates a rigid foam. Furthermore, the mechanical properties and pore size is dependent on the water content of the slurry before the lyophilization process. When dried to completion using various methods of air drying, it creates a hard-bulk source with higher mechanical capabilities. The 3D structural mixture of these various CNF materials is held together through hydrogen bonding.

3.3 Procedure

The as-obtained CNF is placed into a large volume 60-liter Hobart mixing machine, the mixer is ran at a speed gear of 2 (124 rpm) for 3 minutes. With a 1-inch diameter stainless steel whisk attachment, the addition of NPs is followed and repeated for all sample percents. The number of NPs added is dependent on the desired Wt% of the composite produced. For example, to produce the range of samples for this experiment, 1.6-6.3 grams of NPs were added. 25mL of 2M nitric acid is added to the CNF matrix of NPs Wt% of 0.01, 0.1, 0.25, 1, and 5. Similarly, additional films of these 4 Wt% composites were made without the addition of the nitric acid leaving the CNF environment at a pH range from 5-7. The CNF composite mixtures were then poured into molds for a proprietary drying technique. The end result of this process is thin-film samples for imaging. The thin films received scanning electron microscope (SEM) imaging to determine the size and aggregation size of NPs on the cellulose fibers. Additionally, thin films were produced using similar mixing and drying methods without the addition of acid and NPs to produce controls. The resulting films being 1-5% NPs compositions and control of CNF.

3.4 Results

3.4.1 Resulting pH of Iron Oxide/CNF Suspension

Shown in Figure 3.5 is the resulting pH measurements as they correspond to NPs Wt% of the composite. Note the final pH of CNF/NPs composites lacking acid treatment is around 5.5-7 pH range, while CNF/NPs composites treated with acid had a pH within the 3-3.4 range. As shown from Figure 3.3, the size of a particle within non-treated suspensions aggregate due to particle decreasing surface charge, whereas the particles within the CNF environment treated with nitric

acid remain similar in size as they maintain their high surface charge and large particle repulsion characteristics.

3.4.2 SEM Imaging

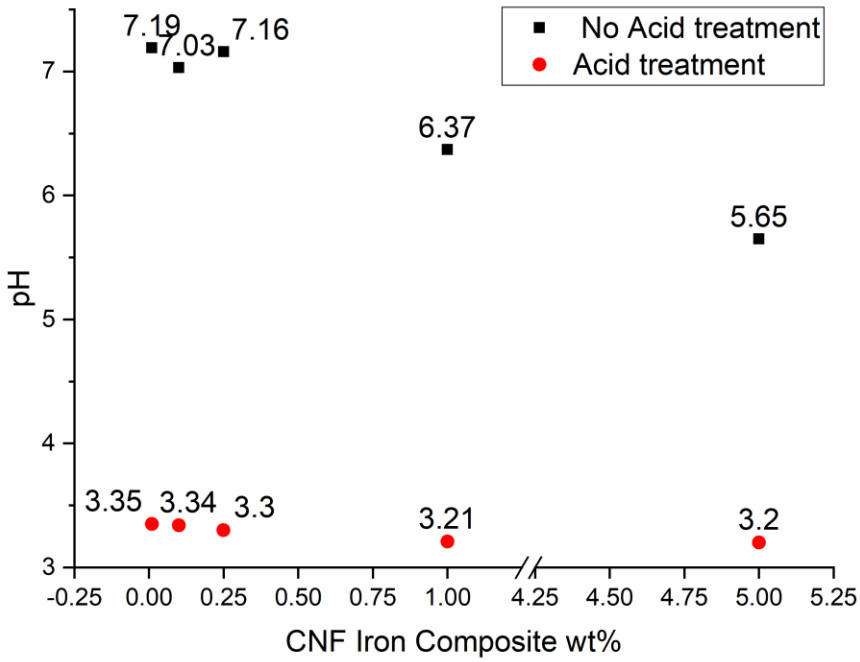

Figure 3.5: pH of acid and non-acid treated CNF suspensions

SEM imaging was performed using a Zeiss NVision 40 Microscope, along a thin ripped edge of the produced films, obtaining a view of fibrous matrix impregnated with NPs. The resulting images had their contrast increased using ImageJ[61] image analysis software to allow better visualization of NPs on the background CNF matrix. In Figure 3.6 (A) image of control, CNF can be observed, and one can note the 20 nm diameter of single CNF fibrils in the middle of the image. On the perimeter of the image, multiple fibrils of adhered CNF form bundles, these bundles have diameter sizes within the range of 20 nm to well over 200 nm. Adherence of fibrils is a result of

hydrogen bonding between the fibers. The optimal focus was difficult to obtain when imaging due to the three-dimensional fibrous matrix creating a significant depth of field.

Due to small amounts of iron oxide present in the 0.01, 0.1, and 0.25 Wt% samples, imaging was difficult to obtain and was ultimately not used. Through the process, 1 percent films and 5 percent films were found to hold sufficient NPs, that was easily located and identified using SEM. In (B) 1 Wt.% NPs can be viewed. Because these films were acidly treated, you can observe homogeneously sized particles embedded within the fibers. When compared to (C), presenting the 1 Wt% CNF/NPs composite film untreated with acid, aggregation of NPs on the fibers that are heterogeneous in size ranges is noticeably observed.

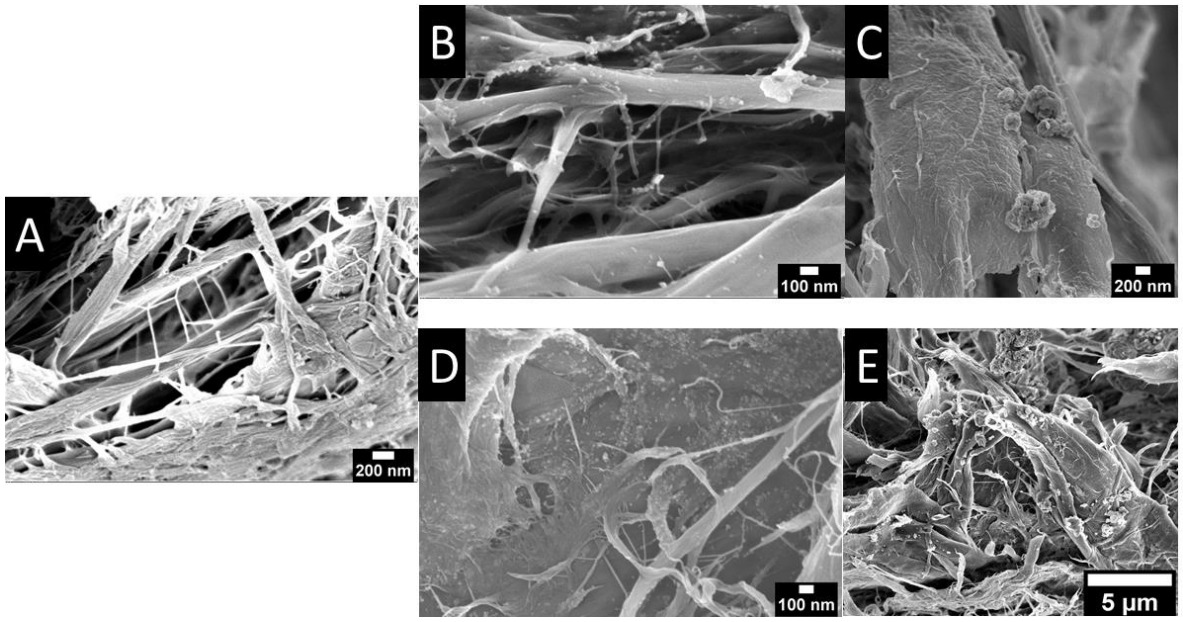

Figure 3.6: SEM imaging of Iron Oxide CNF films.

A) Control CNF no acid or iron NPs added (2kV, 30.34KX), B) 1% Iron oxide NPs film acid treated (3kv, 50.71KX), C) 1% iron oxide NPs film no acid treatment (3kV, 19.28KX), D) 5% Iron oxide NPs film acid treatment (3kV, 40.40KX), E) 5% Iron oxide NPs film no acid treatment (4kV, 3.08KX).

This is also present with the 5 Wt% CNF/NPs films, displaying more NPs throughout the films providing confirmation. (D), (E) show these films. Homogeneously sized nanoparticles are

dispersed in the acid-treated film and range in size distribution around 20 nm (D). In contrast, the film untreated with acid displays NPs aggregation estimated at 1 micron in diameter (E) on average. Separately displayed by mineral oxide composites were their optical variations as displayed in Figure 3.7. Each specimen shown was at a concentration of 1 Wt%, with titanium dioxide and iron oxide displaying most significant visual optical differences than that of pure CNF. Titanium dioxide becomes a milky white composite, while iron oxide becomes a dark brown color.

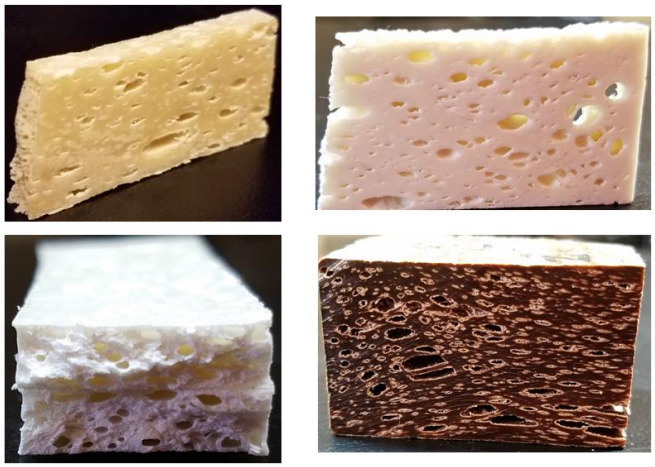

Figure 3.7: Image of all mineral oxide final products

Top right Aluminum Oxide, Top right Titanium Dioxide, Lower left Silicon Dioxide, lower right Iron Oxide

3.5 Discussion

Based on the results from iron oxide CNF suspensions and dried films it was concluded that pH treatment of the CNF prior to loading of metal oxides was critical in maintaining the repulsive properties between the particles. This has been shown to be a promising composite system, providing adequate additional physical and radiological properties to the CNF system. Subsequently, further testing on the CNF metal oxide composites is required to determine if acid treatment of the CNF causes any adverse effects to local tissue of the potential host. Along with considerations to how this metal oxide could react with the tissue of the host, and how the metal

oxide after subsequent orthopedic degradation will be excreted from the host. Additionally, the composite still requires advanced physical and chemical studies. As it is not yet determined if the mineral oxide is binding through hydrogen bonding or if the mineral oxide is simply adhered due to the de-watering process. These tests hold true for all mineral oxides used within these composites, while they have been shown to be promising it is still unknown if the particles are binding to the CNF or simply passively coating it.

Another identified flaw with incorporating these minerals is that many of them have a high affinity for water. Subsequently, within the 3 Wt% slurry, mineral oxides have a tendency to be drawn to the drying capillary bricks due to the pressure change and heavily coat the CNF that is dried there. Additionally, characteristics of these mineral oxides at higher weight percent has not been viewed. With higher Wt% possible problems could arise with the repulsion of NPs as space is limited within the CNF, along with potential aggregates to occur with other low repulsion minerals. Through this work ideally, next steps would introduce a mixed composite CNF system, which would require studying interactions in a slurry of different composite materials, binding and placement upon CNF, and their behavior upon degradation into an aqueous solution.

CHAPTER 4

PHYSICAL ASSESSMENT OF MANUFACTURED MINERAL OXIDE CNF COMPOSITES

4.1 Modulus of Elasticity, Porosity, And Shore D Hardness

When designing biodegradable orthopedic devices three prominent physical characteristics must be analyzed and adhered to a standard set throughout the industry. These three characteristics are mechanical properties, porosity, and durability. Mechanical properties of orthopedic devices are usually characterized through modulus of elasticity or Young's modulus (E_f) (eq 4.1).

$$E_f = \frac{L^3 * m}{4 * w * d^3} \tag{4.1}$$

E_f = Elastic modulus

L = Support length (mm)

m = Slope of stress-strain curve

w = Width of specimen

d = Thickness of specimen

This modulus is formed through the Stress vs Strain curve or the amount of force per cubic feet vs the deflection of the rectangle testing beam. When performing three-point bending a standard is followed for many metallic bone fixation plates, this standard is ASTM F382-17[62]. However, for this specific material, ASTM D790-17[63] was used, which is for unreinforced and reinforced plastics. Similarly, to flexural modulus, Shore D hardness is a standard measurement is taken form material planned for implantation. This gives value to how hard the material is and how

likely it is to be permanently indented, this measurement is a standard with many polymers used in orthopedics. Finally, porosity is a defining characteristic, as it determines how well cells can proliferate into the device, providing it with osteoinductive and osteoconductive properties. With implantable devices interconnecting pore structures showing improved penetration of cells, therefore, this property is a lucrative property to achieve.

4.2 Method

Each mineral oxide composite was prepared in a similar fashion where it was, cleaned, dried, cut into a proportional specimen, dried again, and then finally tested. To measure flexural modulus an INSTRON 5942 was implemented, with appropriate software (INSTRON Bluehill). A three-point bending apparatus is attached to the INSTRON, which consists of a support span that is set to 70 mm and a rounded tip triangle wedge placed in the center. This rounded tip acts as the third point within the bending. Width and thickness are entered into the program and the test is run with the CNF specimen on the support. The test then ran with the triangular head descending at a rate of 5 mm/min. Tests are ended either when catastrophic failure is meet or when a plateauing

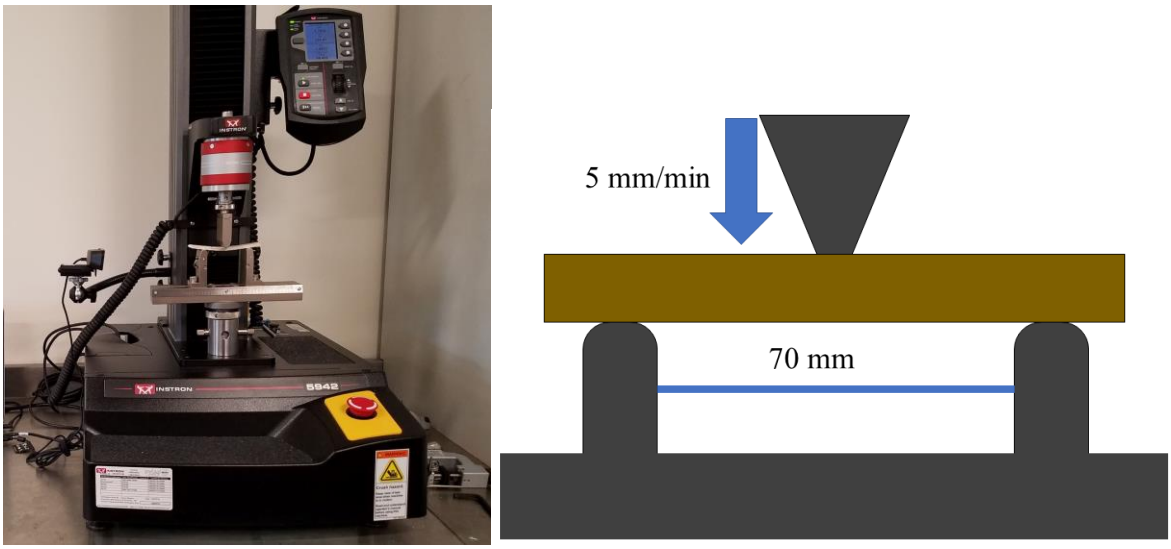

Figure 4.1: INSTRON 5942 (left), diagram of INSTRON during testing (right)

or negative stress/strain slope is achieved. Image and flow of INSTRON testing are shown in Figure 4.1.

$$V=\left(1-\left(\frac{\rho s}{\rho c}\right)\right)*100 \qquad (4.2)$$

V =Void percent

ρ_S = Density of specimen

ρ_C= Density of known CNF

In additionally to Young's modulus, porosity is recorded for all testing specimens. Due to the limitation in present equipment, both economically and specimen size, mainly with mercury porosimetry, the total pore distributions were not measured. With this limitation noted porosity percent of testing specimens were calculated to give apparent porosity of the testing specimens as a whole (Eq 4.2). This was done using the volume of testing specimens made and mass with additives creating a density, as additives were assumed to be negligible for the calculation within a 1% error. The calculated densities were then compared to the known density of CNF, 1500 Kg/m^3, using the equation the percent of porosity was calculated for the specimens. This percent porosity gave a general estimation of the void spaces within specimens, however, did not give estimations of pore size or pore distributions including interconnectivity of pores.

Testing of the specimens for durability was done so using a durometer, measuring Shore D, as seen in Figure 4.2. This device acts like a micro indenter applying a force onto the testing sample which is resisted by the force of the test specimen, this resisted force is then measured

through a spring inside of the device. Shore D hardness is rated from 0-100 with the specificity of 0.5 D with 100 being extremely hard and 0 being extremely soft or no force applied.

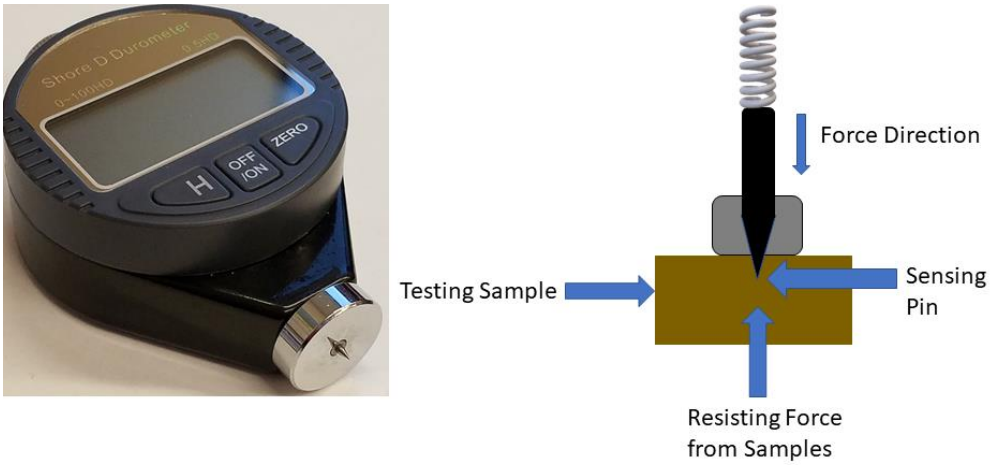

Figure 4.2: Shore D Durometer (left), schematic of Durometer in use (right)

From previous and patented work performed dewatering methods of CNF have been explored, with the most effective method being a ceramic mold system utilizing convection oven for expedient drying. However, with current drying molds flaws were discovered and addressed. Overextended use, ceramic brick material deteriorated preventing proper friction to be formed between bricks. With the addition of CNF into the molds, this would consequently allow the bricks to be kicked out, spilling a large amount of the CNF housed inside. This was solved with the addition of a small aluminum bar across the bottom of the molds. This effectively prevented the bricks from shifting, minimizing loss of CNF material.

Effective drying of CNF ingots was done over a period of seven days, the stepwise process displayed in Figure 4.3. First CNF was obtained from containers, mixed, then added into molds, CNF was undisturbed in ambient conditions for ~24hr with the top uncovered, proceeding this 24 hour time point molds were placed into an industrial convection oven (Wisconsin Oven Corporation model: SW-66-6E) at 158°F for 48 hours with a ceramic interface placed on top of the mold, every 24 hours this interface was monitored. After the additional 48 hours, CNF was removed from the molds and placed onto a metal grate with a ceramic interface on both the top and bottom of the CNF (3). Heating was continued for 72 hours until hornification was achieved and conventional oven drying proved ineffective for the internal layers of CNF.

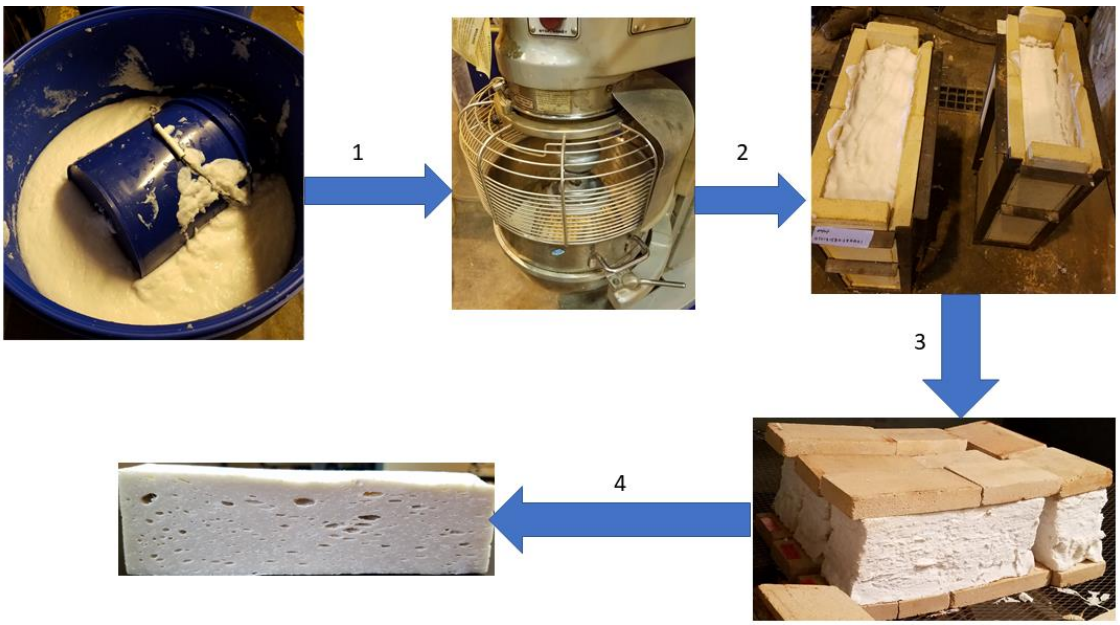

Figure 4.3: Flow chart of CNF bulk manufacturing

Dewatered CNF ingots were taken and machined down into bricks and specimen tabs as shown in Figure 4.4, dimensions T X W X L, with initial clean-cut bricks (1) estimating dimensions of ~22.92 mm X ~45.97 mm X ~203.2 mm, bricks were then cut in half along the length axis to provide 2 individual long rectangles with identical dimensions to the brick above with the width being halved (2). They were then dried further for 24 hours then cut in half along the width axis to provide rectangles (3) of dimensions ~22.92 mm X ~22.99 mm X 101.6 mm. These were then machined down into testing specimens (4) with dimensions ~4.37 mm X ~22.99 mm X ~101.6 mm. Throughout this thesis, the investigation of CNF and manufactured CNF composites for the potential use in orthopedics is presented.

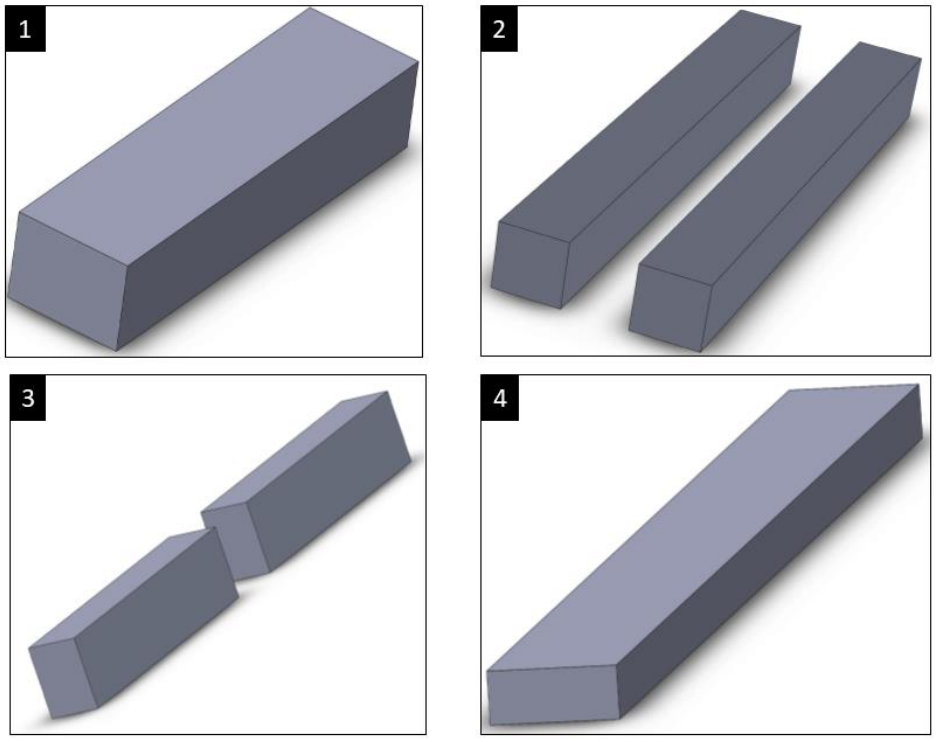

Figure 4.4: Stepwise process of CNF specimen subtractive manufacturing

4.3 Results

4.3.1 Iron Oxide

The as-synthesized iron oxide CNF composite were the first of the oxides to be tested. As this composite was initially investigated for its potential to add contrast to CNF orthopedics allowing radiology techniques to be implemented to observe the CNF device over time. Four weight percent of composites were made for flexural testing. Averages of each Wt% were taken and compiled to present a better understanding of the material system. Pore placement played a pivotal part in premature failure of CNF specimens as this void space would not have fibers reinforcing the load placed on them. However, because pore placement augmentation has not been achieved with current systems, the samples are taken as-is. With initial testing of iron oxide composites, wide variations were noted, these modulus variations were thought to be caused by an increased water content within the CNF composites as seen in Figure 4.5.

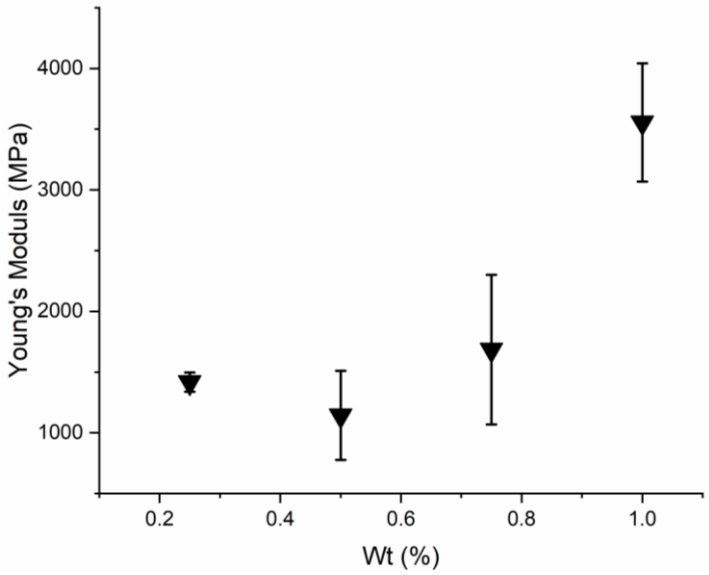

Figure 4.5. Initial test prep method of Iron oxide CNF composite Wt% vs Young's Modulus

Likely due to humidity in the atmosphere or the lack of full dehydration of testing specimens. This increased water content would lead to the samples becoming more plastic, tearing

the material instead of fracturing and yielding. As such samples were dried for an extended 24 hours at 80°C and placed into bags with desiccant packets. With additional steps, composite moduli

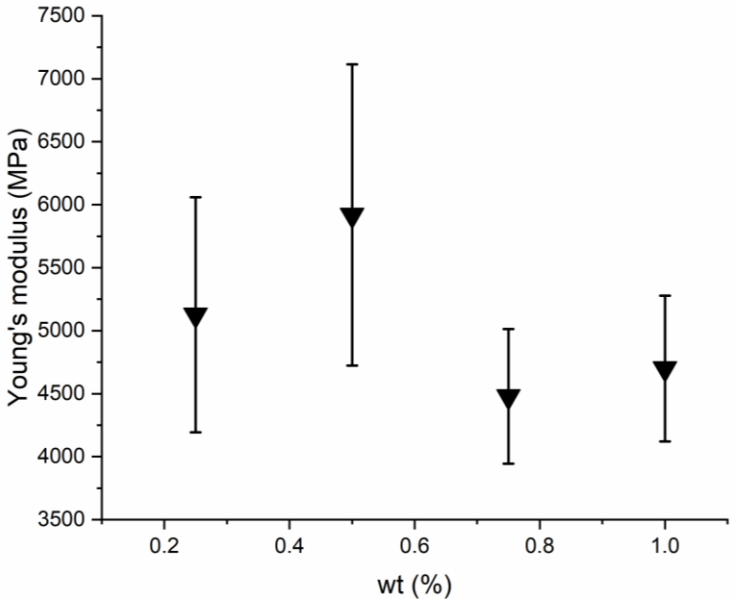

Figure 4.6: New test prep method of Iron Oxide CNF composite Wt% vs Young's Modulus

were shown to increase and reach failure at a more expedited rate, without material tearing. Improved modulus can be seen in Figure 4.6.

After this change in prepping method of specimens, an increase in Young's modulus was noticed for all Wt%'s seen in Figure 4.7. This increase was significant for Wt% 0.25-0.75, increasing from 1500 MPa to around 5000 MPa. With 1Wt% iron oxide composites this increase was not shown to be as significant as the other Wt% composites, with Young's modulus only increasing by about 1000 MPa. From the trend obtained it would appear that the two different drying methods would seem to converge with higher weight percent of iron oxide present in the CNF system. However, whether this is due to water absorption of the new dryer specimens or if this is, in fact, a characterization of the newly manufactured composite material is still undetermined.

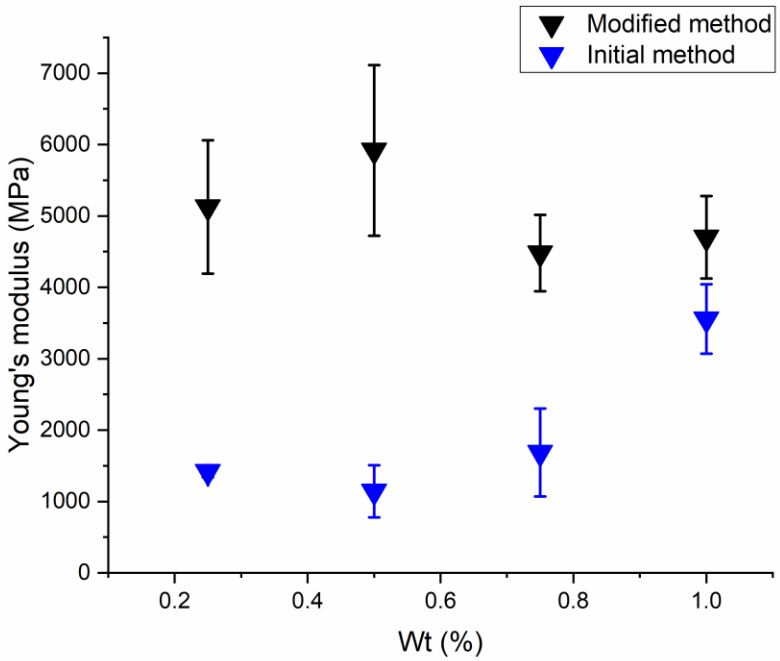

Figure 4.7: Old prep method vs new prep method, Young's Modulus vs iron oxide Wt%

Shore D hardness of the specimens was conducted, this was done using a durometer. As expected, shore D hardness increases initially with the addition of more particles, however with a higher percent of iron oxide present in the composite it was shown to decrease steadily with each Wt%. Additionally, 1 Wt% iron had a significant variation between individual testing specimens resulting in a low mean shore D and a large standard deviation, Figure 4.8.

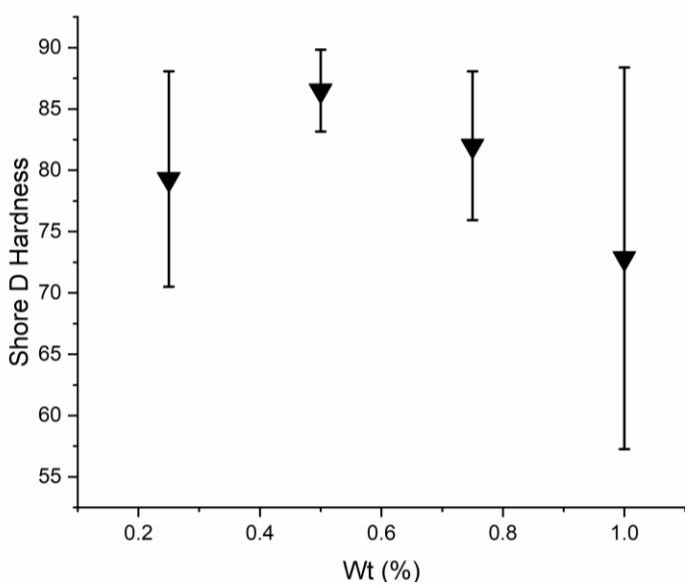

Figure 4.8: Shore D hardness of iron oxide composites

The porosity of iron oxide composites was calculated using (Eq 4.2), displayed in Figure 4.9. When comparing Wt% Young's modulus to porosity a correlation is noticed, as 0.5% iron oxide composite shows the highest Young's modulus it would coincide with the composite having a lower porosity. Meaning there would be more fibers located at the bending location to allow for higher resistance. However, conversely, this does not seem true for 1% iron oxide as its modulus is still relatively low, with porosity % that is also relatively low. This could have been the cause of countless conditions with the 1% sample, mainly with the equation not being able to confirm for the higher Wt% composites. Though it is more likely this is due to water being in the system making the composite heavier than it should be.

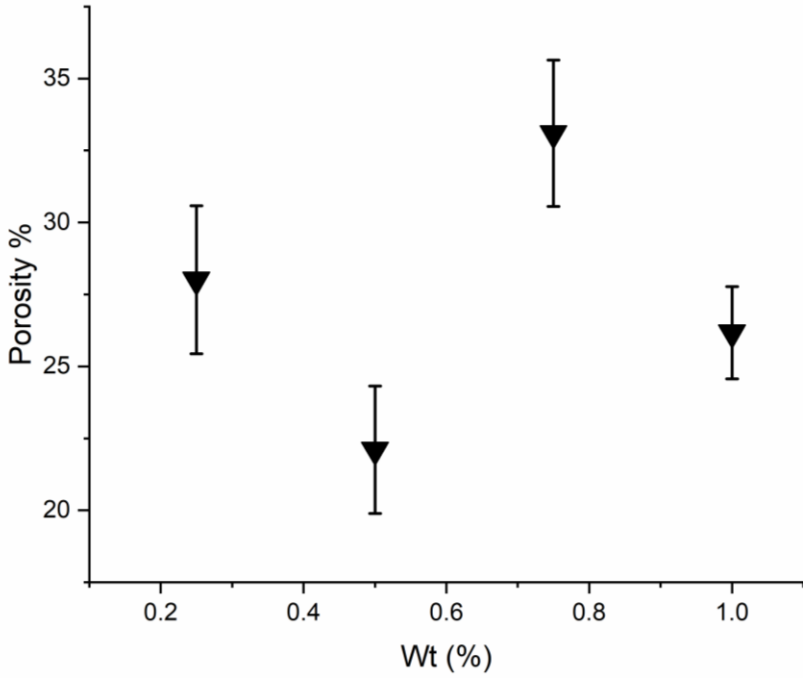

Figure 4.9: Porosity of various Wt% iron oxide composites

4.3.2 Titanium Dioxide

Following iron oxide CNF composites, titanium dioxide CNF composites were investigated. As one of the more common metals used within orthopedics, its effects within the material system was of interest. However, after early-stage trails with titanium composites, utilizing early methods of specimen preparation, materials were found to be extremely plastic and malleable. This was thought to be due to titanium dioxides affinity for water. As such result within early-stage trials of titanium were taken with little enthusiasm, leading to the modified test prepping method, similar to iron oxide and thus adapted henceforth for all other composite specimens. First desiccant packs were added into the containment of the titanium CNF specimens, results of titanium composites with and without desiccant packs can be seen in Figure 4.10.

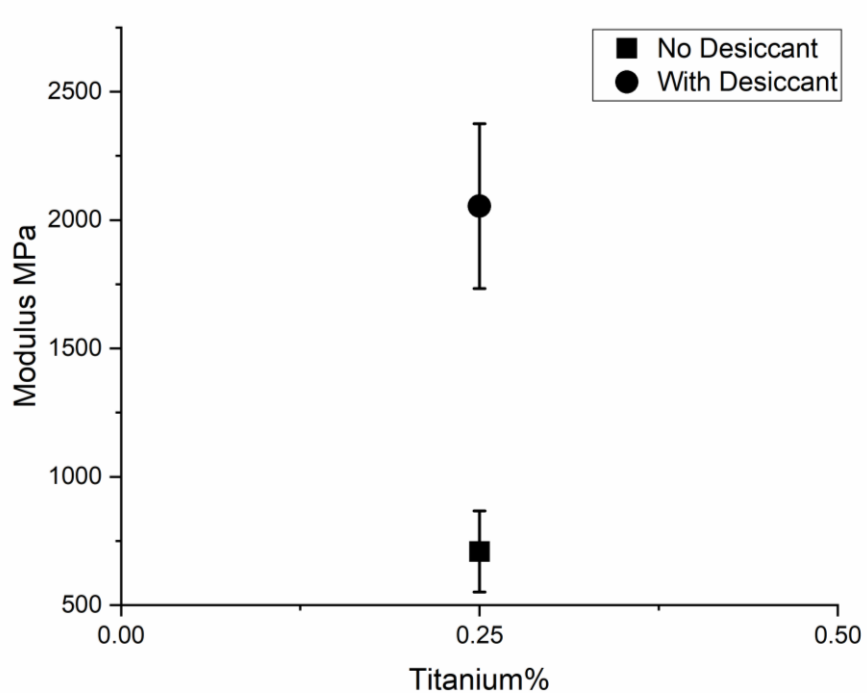

Figure 4.10: Titanium dioxide composite,

No desiccant packet vs addition of desiccant packet

Proceeding this modified preparation method titanium dioxide specimens displayed the most promise with 1 Wt %, with some individual data specimens reaching a modulus around 9 GPa, however, as a whole this testing point had a large range of moduli exhibited. Mainly due to the location of pours and homogeny of titanium through the composite. As expected through the additive property the modulus of titanium dioxide composites increased from 0.5Wt% to 1Wt%, however unexpectedly there was shown to be a loss in modulus initially with 0.5 and 0.75%, but it was then re-established with 1% and carried on to 2%, this can be seen in Figure 4.11, along with individual testing specimens for each testing Wt%, demonstrating the wide range of flexural modulus exhibited by the 1 Wt% titanium specimens.

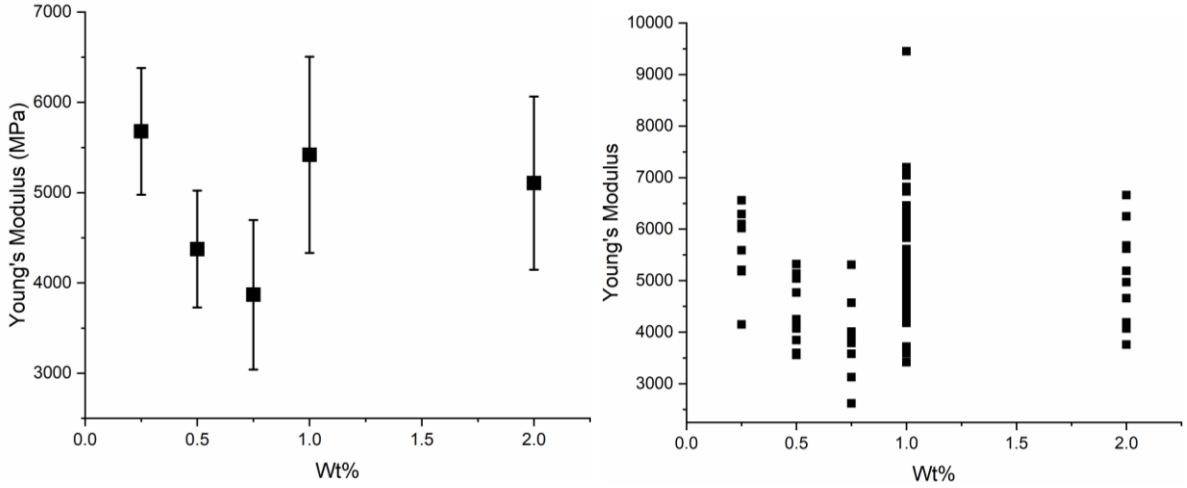

Figure 4.11: Young's modulus vs Wt% of titania specimens

New preparation method of titanium dioxide, Young's Modulus vs weight percent (Wt%) (left), Figure of compiled individual titanium dioxide specimens vs flexural modulus (right)

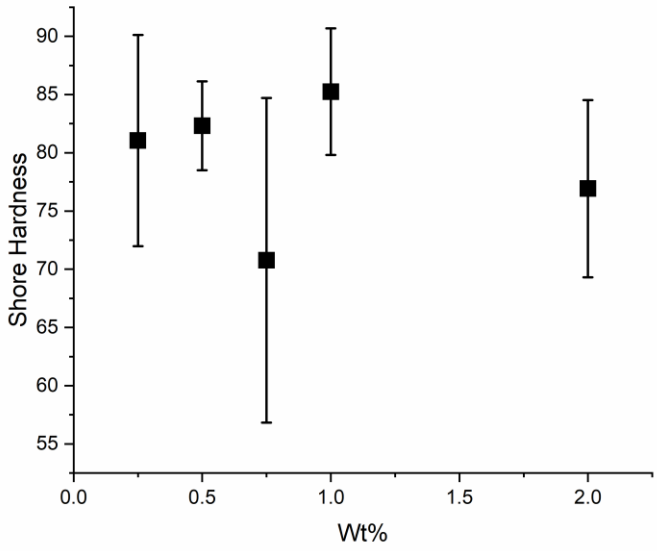

Figure 4.12: Shore D hardness of titanium dioxide composite

Proceeding flexural modulus testing, the durometer was used to measure Shore D hardness, Figure 4.12. Shore D hardness of titanium specimens was shown on average to be higher than that iron

oxide, with 0.25% at 82 and 1 Wt% reaching the highest Shore D hardness at 86. Conversely to the previous testing of Shore D hardness 0.75% was shown to be on average much lower than that of 0.25, reaching a Shore D hardness of 75. Porosities of titanium composites were shown to increase with each increase in Wt% and are shown in Figure 4.13. Excluding 2Wt% which demonstrates a flaw in eq 4.2, when Wt% exceed a 1% offset. Regardless of this, an increase in porosity at 1 Wt% is extremely encouraging for the material, considering the flexural modulus that can be displayed by this material system.

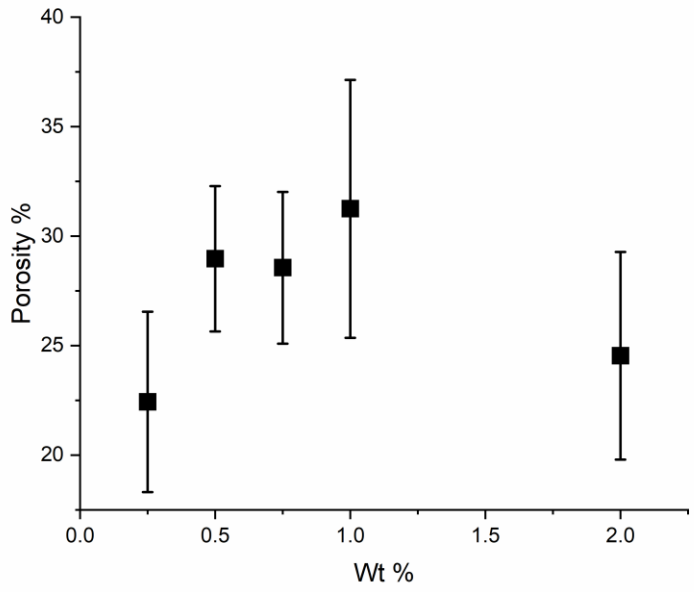

Figure 4.13: Porosity of varying Wt% titanium dioxide composites

4.2.3 Silicon Dioxide

Silicon dioxide was another material of interest as it is used currently in many orthopedics as an additive and is known to be in the bone as a trace element. 60 angstrom, silica gel was purchased from Sigma-Aldrich and used in experiments of Silicon dioxide CNF composites. As with previously made composites a 25 mL treatment of 2M nitric acid was performed, along with

the use of the Hobart mixer with whisking attachment. Similarly, for comparison 0.25, 0.5, 0.75, and 1% specimens were manufactured and tested both with a three-point bending and with the Shore D hardness device. The results of three-point bending can be seen in Figure 4.14, unlike other composites, it was noticed that specimens modulus began to lessen with a higher percentage of silica added, with 0.25% displaying a flexural modulus within 5000 MPa and 1% silica displaying a flexural modulus within 4000 MPa.

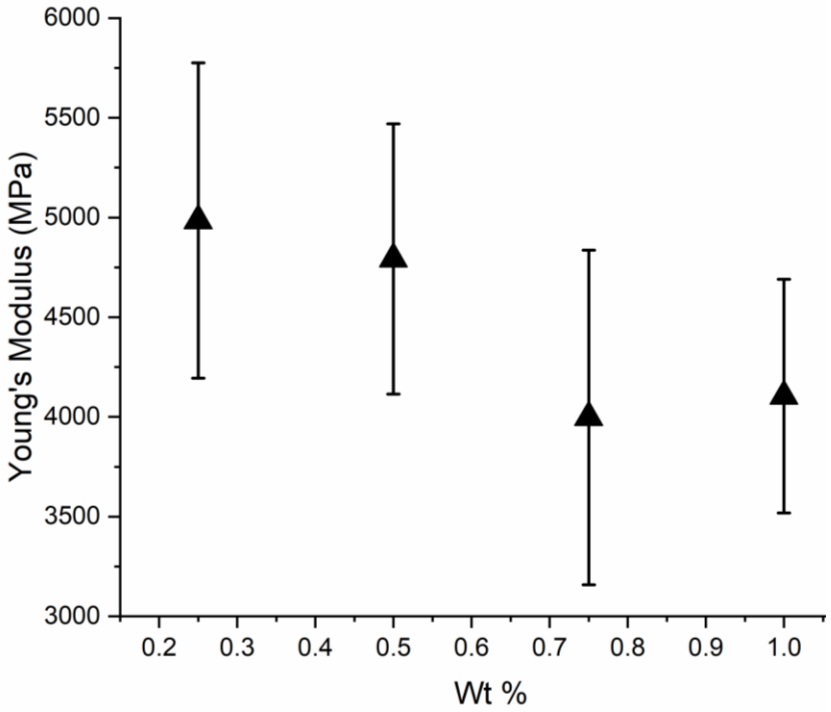

Figure 4.14: Young's modulus of silicon dioxide composites

This decrease in modulus was believed to be due to the silica's hydrophilic nature, as silica is a choice material used for desiccants. Meaning the more concentrated the composites become with silica the more hydrophilic they become. This effect also could be changed depending on the type of silica used, as different vitiations have different interactions with water, one such material is silica glass.

Following three-point bending, Shore D hardness was recorded for each composite Wt%, as seen in Figure 4.15. Following results from the three-point bending hardness of the specimens also decreased with higher Wt% of silica added after an initial increase in Shore D hardness at 0.5 and 0.75%. 0.25% had a hardness of 79, the large standard deviation being caused by both pore location and thickness of specimens tested. As the tester would penetrate void spaces causing a discrepancy in tests. When compared on average with composites of higher Wt% showed hardness below 77, showing that the system would become soft.

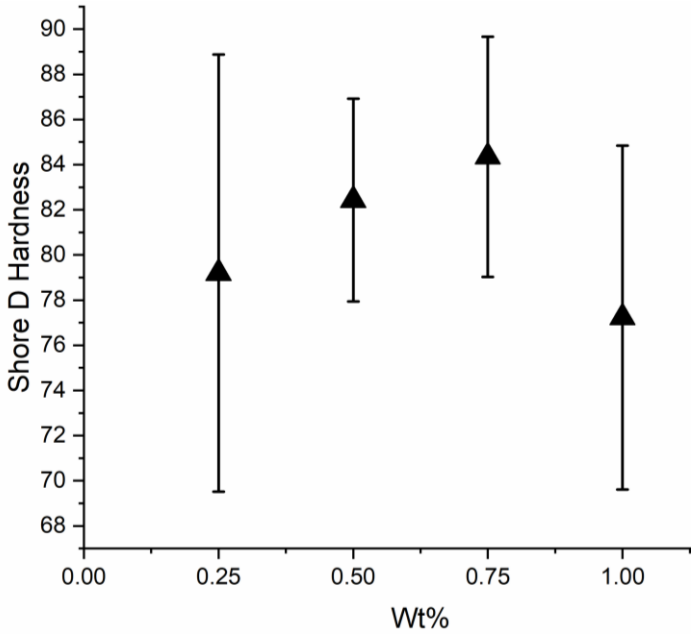

Figure 4.15: Shore D hardness of silicon dioxide composites

Due to samples not being recorded for weights when initially tested 1% silica porosity data, and humid conditions currently preventing a repeat trial with 1% silica, it was ultimately omitted from this thesis. 0.25, 0.5, and 0.75 are shown below in Figure 4.16, as shown porosity of these specimens did not show high variation, with each Wt% maintaining around 27-28% porosity.

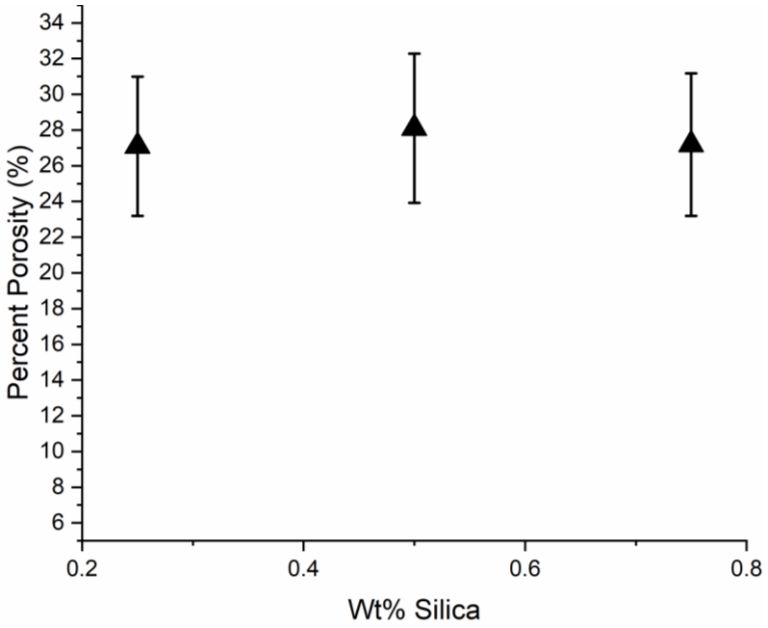

Figure 4.16: Porosity of various silicon dioxide composites

4.2.4 Aluminum Oxide

Additionally, used with implants currently is Aluminum oxide, as such testing began with this metal oxide to determine its effects on the system at low weight percent. Aluminum oxide composites were prepared identically to previously made composites. After drying and cleaning the ingots were processed into testing specimens and dried again to completion. After three-point bending was performed on each of the specimens, the flexural modulus of each Wt% can be seen in Figure 4.17. Unlike previously tested mineral oxides, aluminum oxide displayed a gradual increase in modulus for each concurrent increase in Wt%, with the exception of the slight decrease ay 0.5%. Modulus increased from 0.25% to 1% with a mean modulus of 5100 MPa to 5500 MPa, respectively.

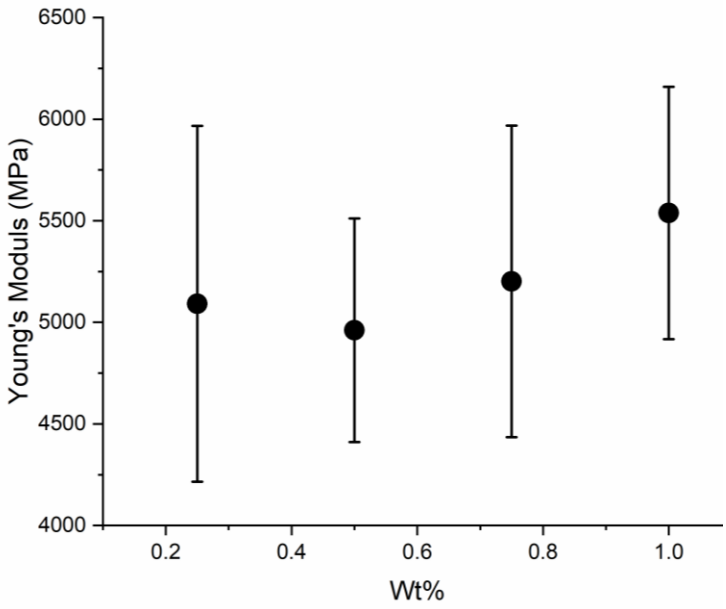

Figure 4.17: Young's modulus of aluminum oxide composites

Again, Shore D hardness was tested for all Wt% specimens of aluminum oxide composites. Unlike suggestions of the flexural modulus, 1% did not show the highest durability, instead, 0.75% showed to have the highest Shore D hardness reaching 85, however, the standard deviation for 1% encompassed most of the region in which 0.75% displayed. All resulting Shore D hardness tests for each Wt% aluminum oxide can be seen in Figure 4.18.

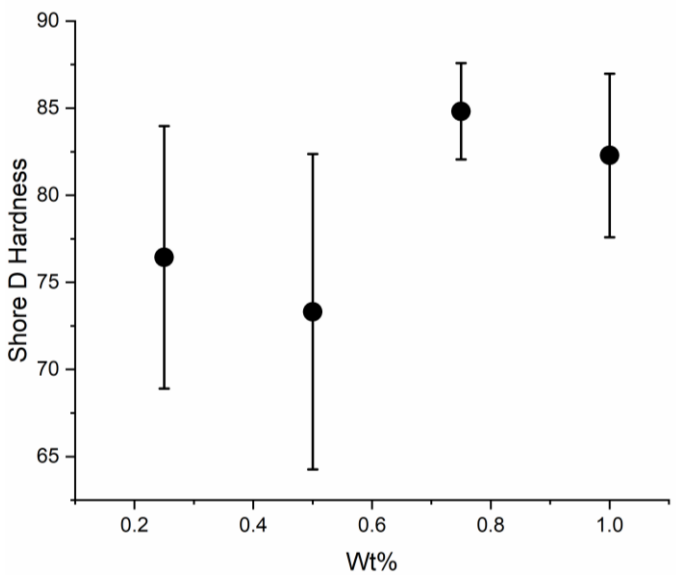

Figure 4.18: Shore D hardness of aluminum oxide composites

Following Shore D hardness porosity percent was calculated for each Wt%, this result showed an increase in porosity for each concurrent increase in Wt% seen in Figure 4.19. With an initial porosity percent at 25 to an increase to 29%. Additionally, 0.75 Wt% showed the highest standard deviation when compared to all other Wt% composites. This could be due to heterogeneous distributions of aluminum oxide throughout the specimens, meaning some specimens could have a higher concentration than other specimens, ergo bringing about the discrepancies in porosities based from the weight, conversely this could be due to water content. However, with 1 Wt% not displaying high variations this is not thought to be the case, for 1 Wt% would display higher hydrophilic effects due to higher concentrations of aluminum oxide present in specimens.

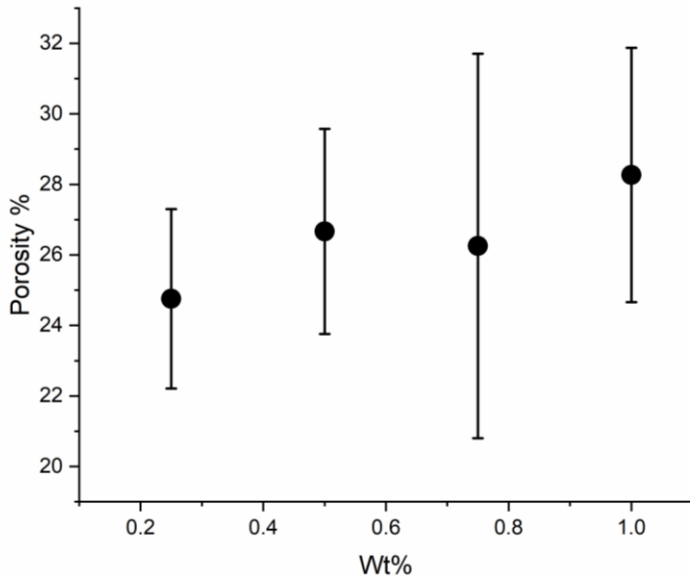

Figure 4.19: Porosity of various aluminum oxide Wt% composites

4.2.5 Collective Physical Properties of All Mineral Oxide Composites

Proceeding individual testing of all composites, results were compiled to gain perspective performance of each mineral oxide, first flexural modulus was compared seen in Figure 4.20. As seen modulus for silicon shows decreased modulus over time, along with silicon it was shown that iron oxide also followed this trend excluding its initial increase in modulus. Titanium dioxide composites and aluminum oxide were shown to be different within initial Wt% and showed a significant difference in modulus at 0.75%. With aluminum oxide composites possessing the highest flexural modulus, with titanium dioxide displaying the lowest modulus. Conversely, at 1% titanium and aluminum oxide modulus were shown to be considerably similar.

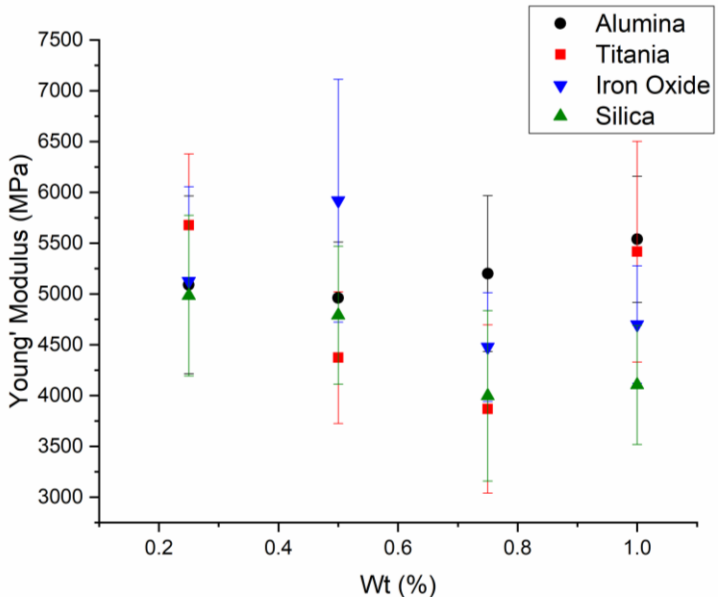

Figure 4.20: Compiled flexural modulus of mineral oxide composites

Shore D hardness of all composites was next compared and shown in Figure 4.21. For 0.25%'s hardness was relatively clustered near 80, proceeding this Wt% Shore D hardness began to spread out. At 0.5 Wt%, composite aluminum oxide composites displayed lowest Shore D hardness while iron oxide composite displayed highest Shore D. At 0.75% aluminum oxide

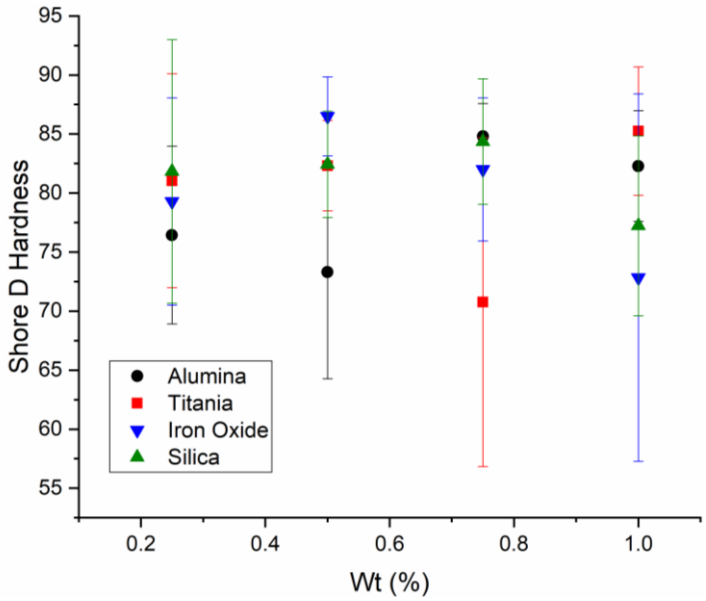

Figure 4.21: Shore D Hardness of all mineral oxide composite

displayed higher hardness than that of silicon, while titanium dioxide displayed the lowest Shore D hardness. At 1 Wt%, composite titanium dioxide displayed highest Shore D hardness, while iron oxide displayed the lowest Shore D hardness. Again, demonstrating some mineral oxide systems hydrophilicity compared to others. The porosity of all composites is shown and compared in Figure 4.22. from this it was shown that porosity of specimens such as alumina and titanium dioxide had an increasing porosity with increasing Wt%, the increase was from 25 to 27 and 13 to 31, respectively. While specimens such as iron oxide displayed a wide range of porosities with each change in Wt%, while silica porosities changed rather minutely when compared to all other composites.

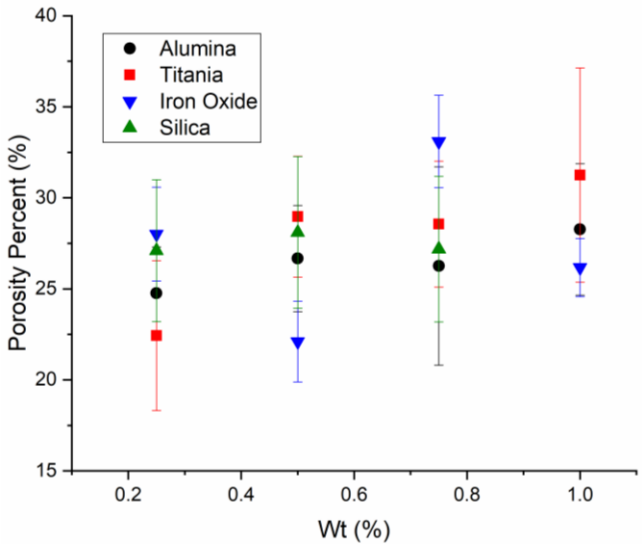

Figure 4.22: Compiled porosity of mineral oxide composites

4.3 Discussion

With the addition of mineral oxides into the CNF variation of physical properties were noticed on a case by case bias, one such physical change was in mechanical properties which would shift drastically from composite to composite. Mainly this was thought to be due from composite materials affinity to water and conditions in which they were tested. As humidity was

not controlled within the room where the INSTRON was located, variations were bound to occur in between testing specimens, which would explain the large uncertainty in certain mineral oxide composites. Ideally, tests would be conducted within a room that is always humidity and temperature-controlled, to minimize any environmental variation between specimens. One such solution would be a bio box attachment for the INSTRON device, which would regulate temperature and humidity around samples placed within the box while having the added benefit of testing specimens at biological temperatures.

Shore D hardness testing of specimens showed that alumina oxide specimens contributed the most consistent Shore D harnesses, while other samples such as silicon dioxide and iron oxide displayed large uncertainty with hardness, especially towards higher weight percent. While results shown are promising for materials human error along with environmental error would contribute to the variation shown between specimens. As explained with modulus, composites hydrophilicity would affect the specimens, this would cause them to become soft and non-resistant to micro indention leading to lower Shore D. Additionally when operating the durometer penetration on different fibers and areas would cause vitiation, along with the location of pores. Future use of the durometer and a Shore D hardness testing location on the specimens should be implemented, as to discourage testing of the whole specimen for favorable outcomes.

Porosity calculations of the specimens yielded relatively similar results, with exceptions to 0.75% iron oxide, and 1% titanium dioxide, which showed slightly increase porosity percent (32%) when compared. Eq 4.2 however useful for pure CNF was flawed when used for composites, as composites weight would affect outcomes of porosity shown and would increasingly become a problem for higher weight percent composites. Additionally, this equation would not provide any

physical information regarding the pore sizes, distributions, and interconnectivity. Taking this into mind new methods of pore characterization should be considered in the future.

All testing specimens thus far have been low in weight percent composites and have been preliminary. In the future, higher weight percent composites along with mixed composites will need to be tested for all three physical characteristics, with additional changes to the testing protocol for all new composite systems. Thus, providing concrete and reliable results from all specimens testing and displaying any composite materials that are unfavorable for end-product specifications.

CHAPTER 5

MECHANICAL MANIPULATION OF CNF

5.1 Introduction

As mineral oxide composites were investigated, consideration was taken from the use of mechanical manipulating the CNF during previously conducted tests. As such it became apparent that manipulation of the pure CNF should be investigated to discover the effects of mechanical mixing speeds and times upon the material system. This, in turn, would warrant further testing of the composites to produce a homogenous mixture of CNF with the composite material, and possibly incorporate additional air pockets, however, this was not investigated in this thesis. These air pockets would stay locked within the system as it dries increasing the number of small void spaces within the CNF. CNF from the previous testing has been shown to be adequately viscus even at 3 Wt% slurry. Additionally, CNF does not settle as quickly and when expedited in drying maintains many of the inner pockets of voids even after prolonged periods of time. This experiment could potentially offer a simplistic and cost-effective means to control base CNF porosity and impact the porosity of new composites in future work.

5.2 Method

CNF has been shown to have high viscosity property at a 3 Wt% slurry, this, in turn, makes the slurry difficult to mix with low surface area mixing tools at high speed, such as paint mixers or small spindles. To mitigate this a large 1-inch diameter stainless steel whisk was used for all mixing operations, this attachment was used in parallel with a stainless steel large 60-liter volume capacity bowl on a Hobart H600. The mixer was used first at a constant time of 3 minutes with various speed gears 1 (70 rpm), 2 (124 rpm), 3 (206 rpm), and 4 (362 rpm). Proceeding mixing the

CNF was poured into molds, dewatered, manufactured, and prepared for testing as previously discussed specimens.

Following speed variation, a set speed was chosen and tested for varying time points 6, 9, 12, and 15 minutes, as time point 3 was already investigated during speed variation testing. Again, mixed CNF was poured into molds, and followed all procedures as previously discussed. Following all manufacturing of the mixing tested CNF 3 point-bending was performed on the rectangular specimens. Along with durability testing and porosity, calculations were done for all specimens both speed and time variations.

5.3 Results

5.3.1 Mixing Speed

As the mixer only had 4 gear speed each was investigated. When tested speed 4 (362 rpm) specimens required a splatter shield to preserve samples as the mixing machine was in use, as the vigorous mixing caused CNF held within to be upheaved out of the device. After drying all samples were tested in a similar fashion to composite samples in chapter 3. Mixing speed variation testing of pure CNF in the Hobart mixer is displayed in Figure 5.1. Highest flexural modulus from tests was shown to be from speed one (72 rpm) specimens at 6000 MPa. With speed 2 (124 rpm) displaying the lowest flexural modulus below 5000 MPa, then a steady increase in flexural modulus is noticed in speeds 3 and 4 with a flexural modulus of 5000 MPa and 5750 MPa, respectively.

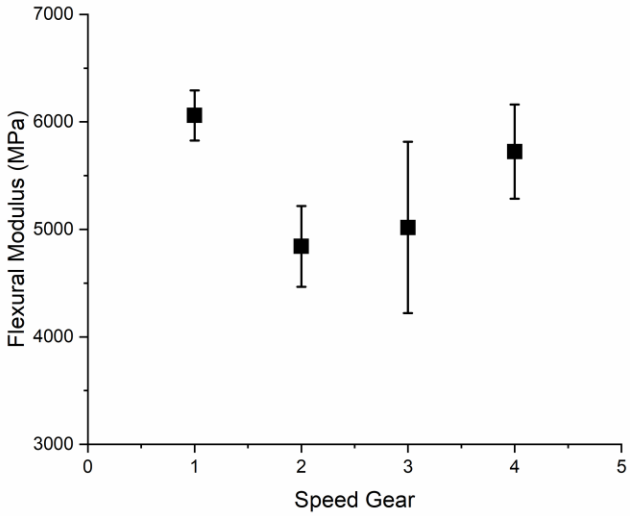

Figure 5.1: Mixing speed vs Flexural modulus (MPa)

These moduli were then compared with calculated porosities shown in Figure 5.2, when compared high modulus of speed one had a concurrent low percent porosity. Speed 2 specimens which had the lowest flexural modulus showed the highest percent porosity around 27%, with speed 3 and 4 having decreased porosities which matched the increase from speed 3 to speed 4. These flexural modulus's and porosities correlation are based on the idea that lower porosity would provide higher flexural modulus for less void space would be present throughout the specimen, whereas lower modulus would be specimens with higher porosity percent.

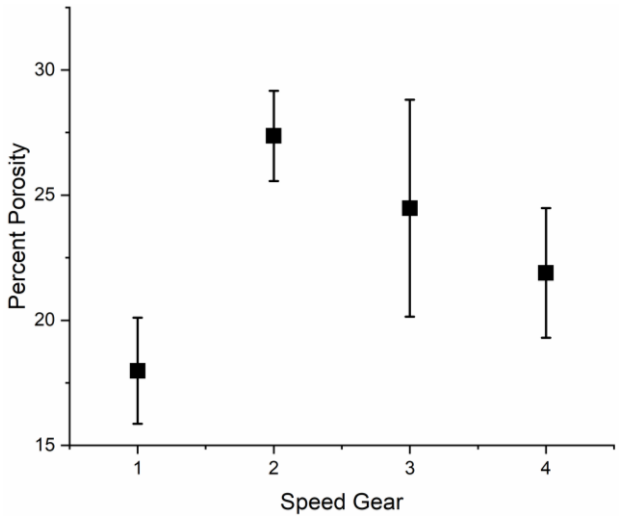

Figure 5.2: Mixing speed percent porosity

Following porosity calculations, Shore D hardness of each specimen was taken, shown in Figure 5.3. From hardness's tested it was shown that samples at a speed of 1 had highest Shore D hardness while that of speed 2 had lowest Shore D hardness, with speed 2 also showing highest variation in between individual specimens, likely due to this samples increased porosity. Speeds at gear 3 and 4 showed very similar Shore D hardness, with speeds 3 and 4 displaying a hardness of 83, however, there was much less variation displayed from speed 3 samples.

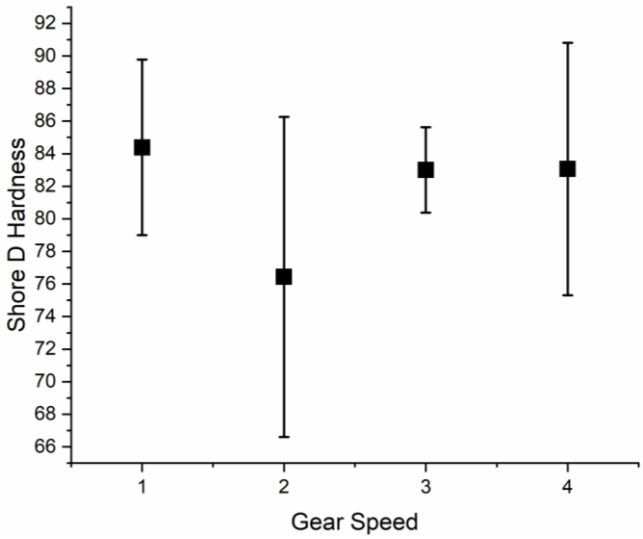

Figure 5.3: Mixing speed specimens Shore D hardness

5.3.2 Time Variation CNF Mixture

Proceeding speed variation testing, mixing times were investigated, for this, it was decided to use a constant speed of 2. As this speed was used previously in composite manufacturing and as displayed above-produced samples with lower flexural modulus and higher porosities. Again, following complete drying samples were tested for flexural modulus and compared, seen in Figure 5.4. At a time of 3 minutes, previous flexural modulus can be seen at 4800 MPa, after mixing for 6 minutes this modulus was shown to increase to a modulus of 5450 MPa. This increase was shown to be constant with samples henceforth with 9 minutes displaying a modulus above 5500 MPa and 12 minutes displaying a modulus slightly below 5500 MPa.

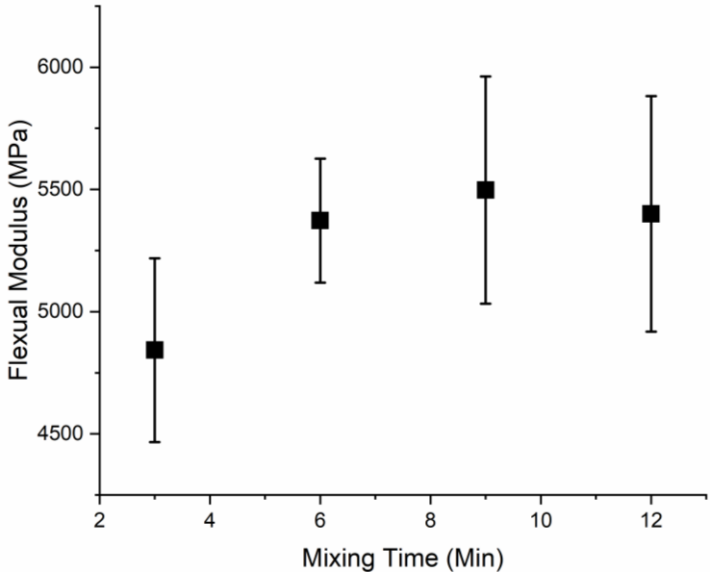

Figure 5.4: Mixing time at gear speed 2 vs Flexural Modulus

Porosities for each of these time-variant specimens were calculated and compared in Figure 5.5. From time 3 to 6 minutes mean porosities were generally the same, with 6 minutes differing in variations shown. This suggests that even with its increased flexural modulus, the porosity of the specimen was preserved. Following these porosities at time 9 and 12 minutes were shown to

be slightly lower than that of shorter times. With 9 minutes displaying a porosity of 25%, while 12 minutes displayed a porosity around 26%, however, 12-minute samples also displayed the highest variation in porosity.

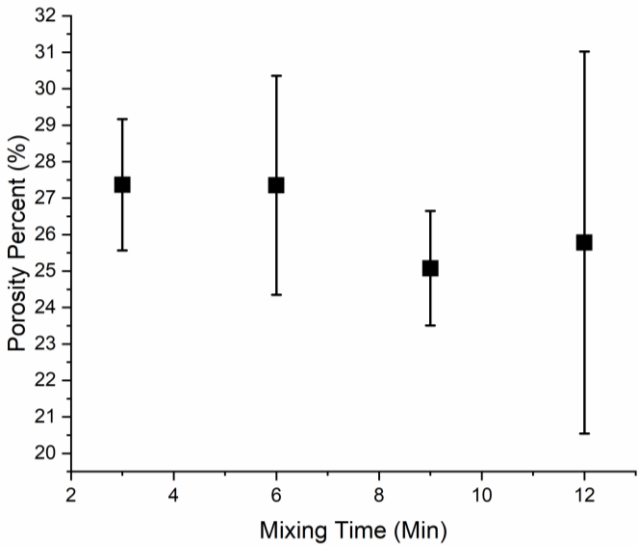

Figure 5.5: Mixing time variation vs percent porosity

Shore D hardness of all-time variation specimens was performed after porosity calculations. The hardness of specimens can be seen in Figure 5.6, interestingly compared to other testing Shore D hardness of time-variant mixed CNF showed a gradual increase in hardness.

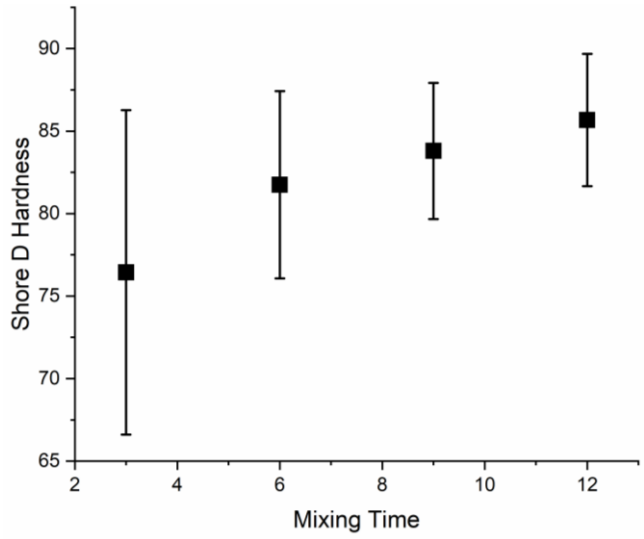

Figure 5.6: Shore D hardness of time variant CNF spenicmens

Initially, at 3 minutes Shore D hardness was 77, whereas specimens at 6 minutes displayed a Shore D hardness of 82. This trend continued with times 9 and 12 showing Shore D hardness of 83 and 85, respectively. Additionally, with this gradual increase in hardness standard deviation between individual specimens was shown to decrease as well over increased mixing times.

5.4 Discussion

From both mixing speed and mixing time variation testing it was shown that physical properties of CNF could be altered without the addition of mineral oxides. With an increase in porosity being shown with specified speeds and flexural modulus being increased with additional mixing times. Additionally, it was shown that hardness of samples could be increased with increased time as well. With many of these physical attribute increases were thought to be brought about with either increased bundling of CNF fibrils, as mixing would increase chances of fibers to bind together through hydrogen bonding, creating stronger denser fibers throughout. Or fibers would be rearranged when mixed, aligning in a fashion that would facilitate higher flexural modulus and durability while not compromising porosities.

While results were positive the necessity of mineral oxide composites still remains clear, as many flexural moduli did not reach that of previously tested composites. With higher flexural modulus pure CNF specimens displayed extremely low porosity when compared to similar flexural modulus of higher percent porosity composite CNF. Following results from experiments testing of time variations at different speeds should be investigated, along with time and speed variation testing of already tested mineral oxide composites to monopolize on any potentially added void spaces or flexural modulus increases it could display.

CHAPTER 6

HYDROXYAPATITE SYNTHESIS AND CNF/HA COMPOSITES PHYSICAL ANALYSIS

6.1 Biological Accurate Hydroxyapatite Synthesis

Up to 70% of natural bone is comprised of modified forms of hydroxyapatite (HA) combined with a number of other trace metals and ions such as magnesium, carbonate ions, and acid phosphates, known as bone minerals[1,64]. Synthetic HA, with the stoichiometric formula of $Ca_5(PO_4)_3OH$ is considered promising bone substitute due to its biocompatibility, osteoconductive behavior and ability to create a firm bond with bone tissue[65–68]. HA can be used to generate a bone-like calcium phosphate coating on the implant surface increasing bone-implant integrity[69]. Although HA can be extracted from natural sources such as fishbone[70], eggshells [71] and bovine bones [72], these processes can be extremely time-consuming and cost-prohibitive. In general, cost-effective forms of synthetic HA demonstrating the metabolic activity, dynamic response to the environment, and the immunogenic response of natural HA [73,74] are not yet readily available. Some of the challenges for creating a synthetic HA are replicating the many chemical and physical properties possessed by biological HA. For instance, the natural HA crystallographic structure and nonstoichiometric composition (Ca:P molar ratio 1.67), with very low solubility HA[5], has been shown to affect its solubility and bioactivity. Natural HA has disordered nanostructures[75] that help to improve bioavailability with application in bone implants, with relatively small crystalline domain sizes ~20 nm[1,74,75] that have been shown to improve the promotion of cell growth[75]. Reportedly, this is at least in part due to the increased physical interaction between cells and the host material that arises as a result of the large surface-to-volume ratio of the nano-sized particles

[6]. Therefore, to create a synthetic HA additive for medical devices and implants that mimic natural HA properties both the chemical and physical properties must be considered.

HA has been synthesized by different methods such as co-precipitation[76], sol-gel[77], hydrothermal processing[78], and solid-state reaction methods[79]. In this study, a modified hydrothermal method was used to synthesize HA with chemical composition and properties found in biologically relevant HA. Several mechanical milling processes were investigated and their effects on HA crystallite size and aggregates were compared to commercially available, biologically relevant HA. Fourier Transform Infrared spectroscopy (FT-IR) was used to determine the optimum reaction time to produce HA with desired chemical composition. FT-IR was also used to confirm that *in situ* and *ex situ* milling did not affect the chemical composition of the synthesized HA. X-ray powder Diffraction (XRD) was used to determine the crystallinity and primary crystallite size of the as-prepared samples. A Malvern dry Mastersizer was used to determine the particle size distributions of the aggregates. Scanning Electron microscopy (SEM) was used to quantify the extent of aggregation and particle morphology.

6.2 Procedure

6.2.1 Material

Calcium Phosphate, monobasic 90%, pure, and Calcium Hydroxide, 98%, (extra pure) reagents were obtained from Fisher Scientific and used without modification. Reagent grade hydroxyapatite was purchased from Sigma-Aldrich (Product number: 289396) for use as an initial standard for FT-IR measurements. A commercially available electric pressure cooker (Greek Chef, Model: YBE60P) with a temperature controller was used as a hydrothermal reactor. A 3 lb capacity ball mill with zirconia milling media (ABmo408, 2 mm diameter) was used to achieve the desired size reduction of both precursors and the final dried HA powders. Additionally, a large shaker

chest was used during synthesis for simultaneous agitation. *In situ* ball milling (BM) was implemented during the simultaneous agitation by the addition of ½-inch and 1-inch chrome stainless steel ball milling media to the hydrothermal reactor.

6.2.2 Experimental Procedure

A simplified hydrothermal synthesis method for HA developed by Liu *et al.*[80] was modified for the production of HA in this study. HA was synthesized using a 200 g total powder mixture, with a 3:7 stoichiometric ratio, of calcium phosphate monobasic to calcium hydroxide, respectively. The mixture was initially placed in the ball mill container along with zirconia milling media, in the ratio of 3:1 milling media to powder, by weight. Samples were milled for 1 hour to ensure homogeneous mixing before being placed into the hydrothermal reactor with 2 L of DI water. Six different HA samples were synthesized varying the reaction time from 1-6 hours, in one-hour increments. The temperature was held constant at 109°C in all cases during the reaction. The resulting solution was left undisturbed overnight allowing the reactor to cool and for the HA particulates to settle. The as-synthesized product was then decanted to remove excess water. The remaining material was washed three times with deionized water to ensure the removal of any unreacted precursors. After washing, the product was oven-dried, in air, at 100°C for 24 hours. The resulting powders were bright white in appearance, and clumpy in nature. Ball milling was again implemented, *ex situ*, here to break apart the larger visible clumps, reduce particulate aggregation, and to refine the particle size distribution. Different milling times were explored and

the effect on particle size determined. A simplified process flow diagram for the entire synthesis is presented in Figure 6.1.

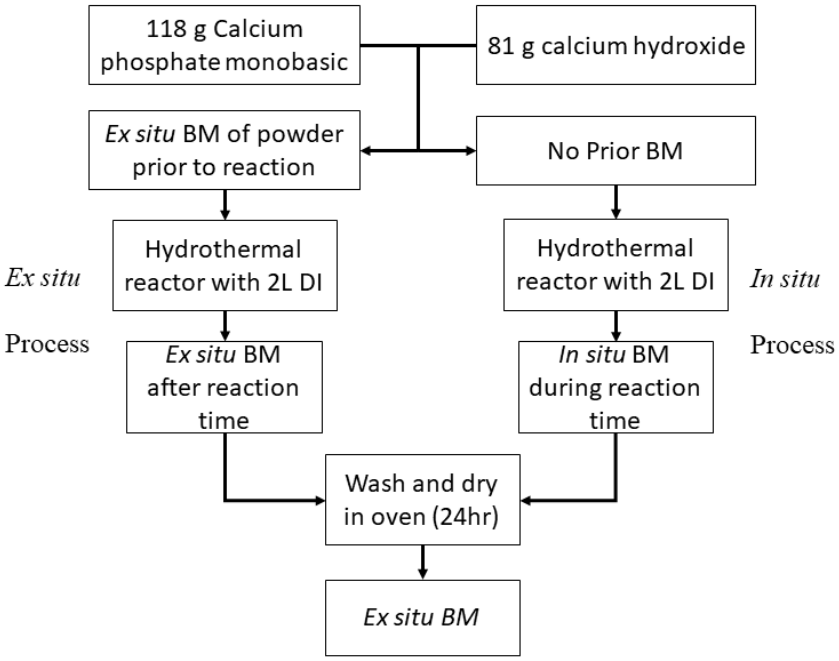

Figure 6.1: Process flow diagram of the hydrothermal synthesis of HA.

As chemical composition and (nanoscale) crystalline grain sizes are both critical for biologically relevant HA, synthesis methods that promote homogeneous reactant dispersion are of interest. In situ methods involving the use of ultrasonic mixing have previously been implemented and shown to reduce reaction times and to promote the production of smaller nano-crystalline particles [81]. This same work, performed by Poinern *et al.*[81], suggests that the use of ultrasound can alter the chemical composition of the product, which may not be desirable. This was mitigated with the use of high thermal post-treatment temperatures (400°C), which affected nanoparticle shape. In order to avoid these effects, while still producing chemically and morphologically relevant HA, simple low-cost *in situ* ball-milling method was investigated. This was achieved by placing the hydrothermal reactor system into a Series 25 Incubator Shaker (New Brunswick

Scientific CO., INC model: G-25). In this setup, the hydrothermal reaction time and shaker rate were held constant at 4-hours and 200 rpm, respectively. With 4 different *in situ* milling variations; no milling media, 1-inch diameter steel milling media only, ½-inch diameter steel milling media only, and a 50:50 mix of 1 and ½-inch steel milling media. The resulting HA samples, once dried as previously described, were analyzed to determine which process created the HA sample with the desired chemical composition, and particle size distribution.

6.2.3 Characterization

Diffuse reflectance Fourier Transform Infrared (FT-IR) was used to analyze the chemical composition of the as-synthesized HA. Here FTIR spectra of each sample were recorded on an FTLA 2000 spectrometer (ABB) using an EasiDrift accessory utilizing a sample to KBr ratio of 20 %w/w *(gain of 1, resolution 4cm^{-1}, 40 scans per spectrum). All diffuse reflectance spectra were converted to absorbance units the using Kubelka-Munk (K-M) model the resulting spectra were filtered using a Savitzky-Golay model to reduce the apparent noise fluctuations in the data to ease the comparison of more significant features between samples. For clarity and ease of comparison, each spectrum was baseline corrected, normalized to the largest peak amplitude, and separated into two spectroscopic regions of interest.

To facilitate the assessment of the chemical quality and biological relevance of the samples, a traceable, widely accessible HA spectrum was used as a reference and target spectrum throughout this study. This spectrum, reported by NIST, extracted from synthesized HA, has been shown to be mimetic, with the exception of the absence of known proteins associated with HA, of naturally occurring bone[82], including Ox femur[83], and fish bone[70]. Relevant spectral features of biological HA should include contributions from phosphate, carbonate, and hydroxyl ions. In contrast, typical high purity reagent grade HA, which is often chosen as a suitable reference, may demonstrate

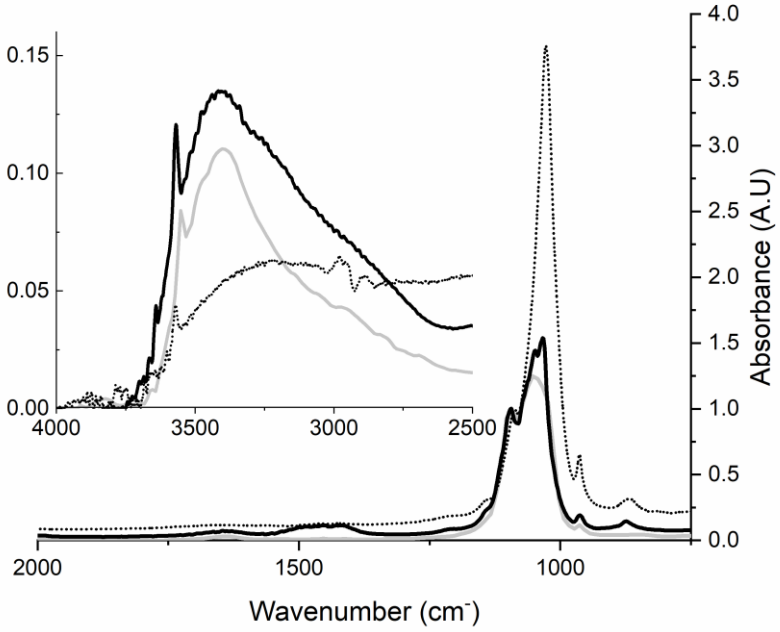

Figure 6.2: Spectra of hydroxyapatite from three sources. Normalized by the 1092 cm-1 phosphate peak following baseline correction. Sigma Aldrich HA (dashed), typical 4hr synthesized HA (black), NIST reported HA (grey).

spectral characteristics not representative of HA found in biology. Figure 6.2 shows the comparison of the HA IR spectrum reported by NIST, with the diffuse reflectance IR spectra of both a commercially available HA sample and a typical 4hr HA sample synthesized by the method presented here. The presence of the relatively weak band at 3570 cm^{-1} can be assigned to the primary absorption of OH^- found within the HA lattice. The strongest absorption bands of phosphate are evident at 1092 cm^{-1} and 1030 cm^{-1}, while the primary absorption bands of carbonate appear at 871 cm^{-1} and 1384 cm^{-1}. Weaker carbonate peaks are also visible at 833 cm^{-1} and 1640 cm^{-1}. The CO_3^{2-} peak is known to result from small amounts of carbonated hydroxyapatite which occurs from PO_4^{3-} reacting with CO_2 in the air[75,78] and is commonly viewed as an impurity in synthetic HA[6,75,81,82]. In fact, as up to 8% of HA found in the naturally occurring bone is in this carbonated form, the presence of some carbonate is desired[1,5,6,73,74].

The resulting as-synthesized HA powder particle size distributions were initially investigated using a Malvern NanoZS dynamic light scattering instrument. However, due to significant sedimentation effects, results were not reliable. As such a Malvern instruments Mastersizer 2000 (Model: APA2000) was used for size analysis of the dried HA. Particle morphology and possible aggregation were investigated by Scanning Electron microscopy (SEM) using both an AMRay 1820 and Zeiss NVision 40 Microscope. SEM micrographs were obtained at 500µm and 10µm scale using the AMRay 1820, (10kV, 40X and 1990X, magnification, respectively). Higher-resolution SEM micrographs (200nm scale) were acquired at 2kV (20,160X magnification) using the Zeiss NVision 40.

X-ray Diffraction (XRD) was used to assess relative quality as well as identify the crystalline phases present in the as-prepared samples. Diffraction data were obtained using a Panalytical Xpert Pro X-ray Diffractometer, with a parabolic mirror and PIXCEL 255 channel solid-state detector. A 2Θ range of 20-60 was used. Crystalline domain sizes were calculated from the XRD data using the Debye-Scherrer equation. Yields were calculated using the mass of fully dried material (120-180 grams) compared to the total mass of precursor reagents and were between 60 and 80%. The variation in yield was attributed to inconsistency during the wash steps, where some material loss was likely.

6.3 Results

6.3.1 Fourier Transform Infrared

FT-IR spectra for samples synthesized with reaction times of 2-6 hours, in one-hour increments, were compared to determine the optimum hydrothermal reaction time. According to the previous work by Giraldo-Betancur *et al.*[82], naturally derived HA is chemically distinct from most synthetic forms of HA, having somewhat elevated hydroxyl levels as seen in the OH^- region

of Figure 6.2. The desired OH^- contribution, arising specifically from incorporation in the material lattice, is visible as a narrow but relatively weak peak around 3570 cm^{-1}. Separately, a broad OH-contribution resulting from adsorbed water, except when aggressive drying or calcination methods are employed, is visible around 3375 cm^{-1}. The relative OH^- content can be quantified, for the purpose of optimization of a given sample, as the OH^- / PO_4^{3-} ratio (R). Stoichiometrically, the OH^- content of the material lattice, relative to PO_4^{3-}, for idealized HA should be around 1:3 (R = 0.33), but is expected to be significantly lower when extracted from IR spectra due to the relatively high absorptivity of OH^- relative to PO_4^{3-}. This disparity does not affect the utility of IR spectroscopy in identifying optimal parameters or the value of the NIST spectrum as a target for this optimization.

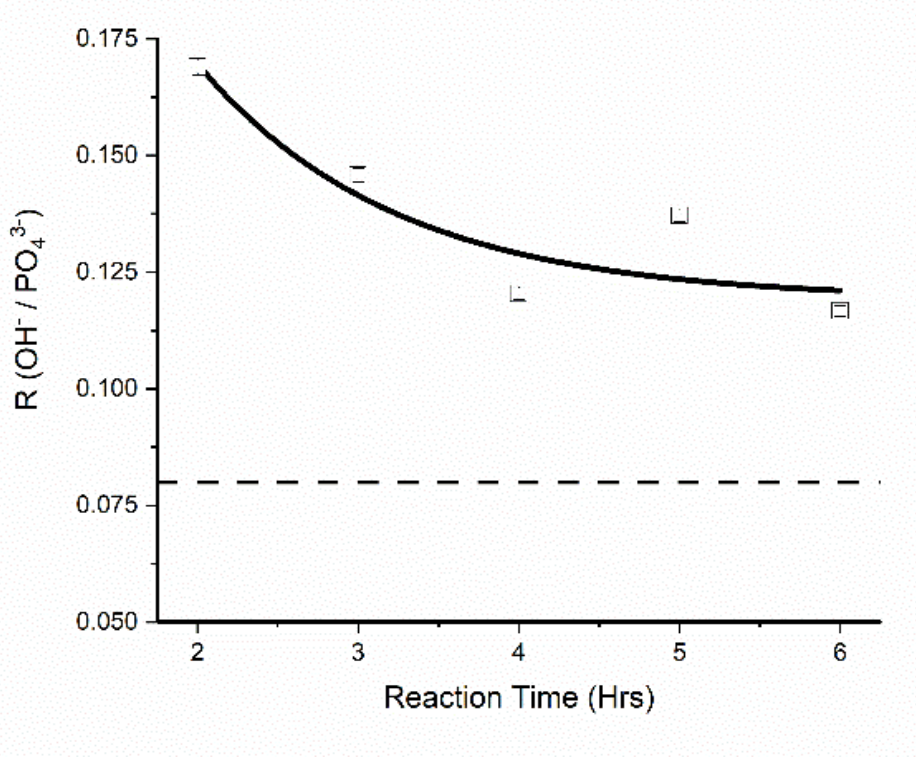

Figure 6.3: OH^- relative to PO_4^{3-} peak amplitudes vs reaction time.

Target value indicated by dashed line. Experimental values, and corresponding variances, are shown as open squares.

In order to extract a meaningful value for the OH^- / PO_4^{3-} ratio (R), the IR spectra were first background subtracted (linear) and then normalized to primary phosphate peak at ~1092 cm^{-1}, which was the only phosphate peak clearly resolved in all spectra. This normalization highlights differences in both the hydroxyl and phosphate regions of the spectra (Figure 6.2). R values could then be readily determined using the incorporated OH^- peak at 3570 cm^{-1}. A target R-value was determined using the NIST spectrum and is visible as the dashed horizontal line shown in Figure 6.3, having an R-value of 0.08. Extracted R-values for all synthesized samples, as a function of hydrothermal reaction time. In all cases, the resulting R-values are significantly above that of the target value, with a weak trend indicating that reaction times above 4 hrs better approach the target value. Based on this result, and for the sake of process efficiency, further studies were performed using a fixed 4-hour hydrothermal reaction time.

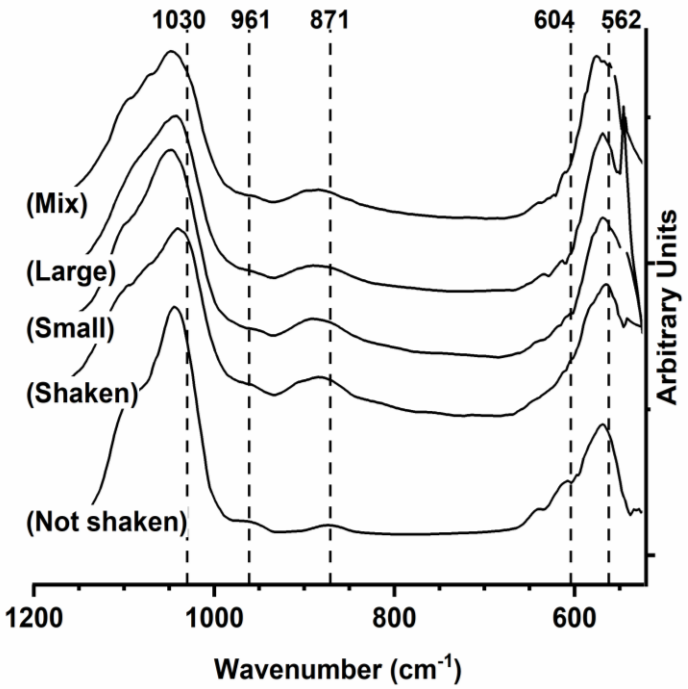

Figure 6.4: FTIR spectra of hydroxyapatite synthesized with a reaction time of 4 hours.

Each of the five samples were prepared under different milling conditions (unmilled, shaken, shaken with small media, shaken with large media, shaken with mixed media). An amplitude offset is used for clarity

To investigate the effects of different milling techniques, and to ensure they have no significant effect on chemical composition, several samples using different milling processes were produced and FT-IR spectra were recorded. Wet and dry milling processes investigated were: *ex situ* dry ball milling, agitation/shaking during synthesis (as a control), shaking with wet *in situ* small steel milling media, shaking with wet *in situ* large steel milling media, and shaking with wet *in situ* mixture of large and small steel milling media. The resulting spectra are shown in Figure 6.4. Predominant expected peak positions are indicated as vertical dashed lines for ease of comparison. While minor variations between spectra are visible, no significant differences are observed indicating that the use of milling can be explored to affect particle size without adversely altering the chemical composition of the HA.

6.3.2 Size Distribution

In addition to composition, biologically relevant HA frequently exhibits specific particle and crystalline grain (domain) sizes. As described previously, accessible crystalline grain sizes on the order of a few tens of nanometers are desirable to promote cell growth. Previous work has reported that crystallinity and grain size are affected by reaction conditions. As such, particle size distributions were obtained for each sample, prepared with different hydrothermal reaction times. The resulting volume-weighted size distributions are shown in Figure 6.5. To help quantify the effects of reaction time and milling resulting particle size, the size distributions were divided into three regions of interest, the second region (II) corresponding to the targeted size region (10-100 nm diameter). In general, the particle size distributions of the as-synthesized HA samples all exhibited polydispersity with significant volume fractions between 20 nm and 1000 μm, and multimodal with predominant sub-populations centered around 20 nm and 300 nm.

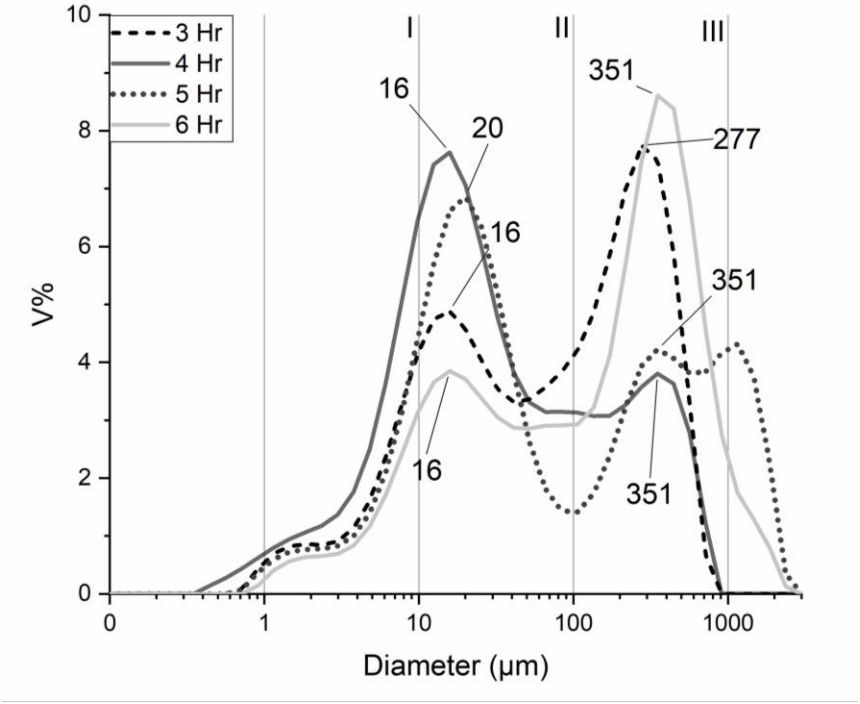

Figure 6.5: Size distributions of unmilled HA with different hydrothermal reaction times

It is immediately evident that the 4-hour reaction time produces the largest volume fraction of material in the target size region. Interestingly, the targeted volume fraction (region II) increases initially with reaction time, then decreases for longer reaction times. This could be a result of continued crystallite growth, agglomeration, or both.

Table 6.1: Comparison of size distribution, by size region, for HA with different *ex situ* milling times

Reaction (hrs) / Milling (hrs)	Vol% (±1%) Region I	Vol% (±1%) Region II	Vol% (±1%) Region III	Total Vol% Region I-III
4 / 0	25	46	28	99
4 / 1	26	53	19	98
4 / 4	22	57	19	98
4 / 24	21	38	30	89

As it is difficult to distinguish between large individual crystallites and aggregates of smaller crystallites using dry particle sizing, a simple mechanical dry milling post-processing step was implemented for each of the as-synthesized samples, in an attempt to break apart aggregates

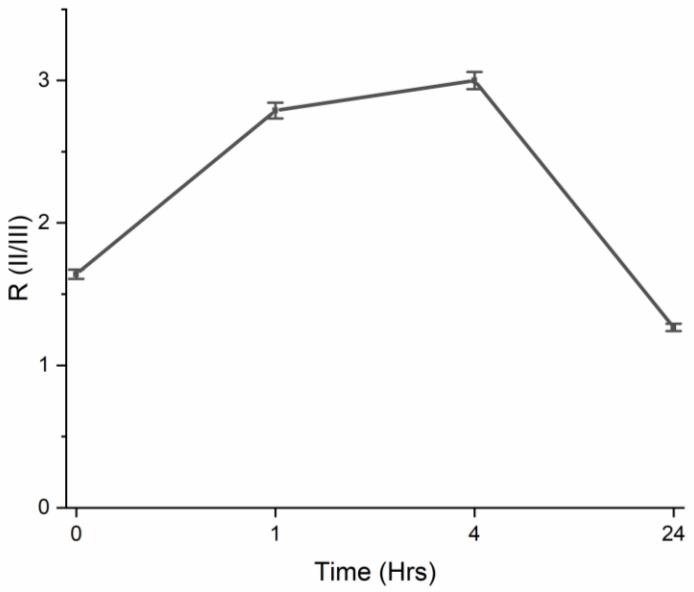

Figure 6.6: Comparison the ratio of the volume fractions vs time

Region II, relative to region III (R = Vol% II / Vol% III), as a function of milling duration.

and further increase the volume fraction in the targeted size region. For this, the as-synthesized dried HA (4 hours hydrothermal reaction time) was placed in a ceramic rotary milling apparatus with a ratio of 3:1 zirconia ball media to HA powder, by weight. Dry milling was implemented under ambient conditions for durations ranging from 1 to 24 hours, after which dry particle size distributions were obtained. The volume fractions for each size region were obtained by integrating the size distribution data. The results are shown in Table 6.1.

Qualitatively, as the duration of ball milling is increased, the target volume fraction (region II) appears to reach a maximum at four hours. This corresponds to a minimum in the volume fraction of region III. This would seem to suggest that, in fact, the larger particles are either aggregates of smaller particles or are effectively refined by the milling process. This is illustrated in Figure 6.6, where the ratio of the volume fractions of region II, relative to region III (R = Vol% II / Vol% III), are plotted as a function of milling duration. At much longer milling times (24 hours), this ratio is again reduced, suggesting that aggregation of smaller particles is significant,

and may be induced by the milling process itself. This is supported by a similar decrease in the smallest size region (region I) which also shows a decrease in the relative volume fraction at longer milling times.

Based on the limited effect of the dry milling experiments on reducing the contribution of the largest volume fraction, an *in situ* wet milling approach was developed based on the work of Kotake *et al.*[84]. This work compared the effects of dry and wet ball milling, including the size and shape distribution of the resulting particles. It is perhaps not surprising that this previous work concluding that wet ball milling conditions produced consistently smaller particle sizes. As such a one-step, one-pot hydrothermal synthesis method, which integrates *in situ* mixing and milling of HA, was explored.

In this approach, various sized milling media were introduced directly into the hydrothermal reactor which itself was affixed within a shaker chest providing the necessary periodic motion to achieve mechanical milling simultaneous with mixing (shaking). Due to their hardness and anti-corrosion properties, spherical stainless-steel media were used. The reactor was then affixed within a closed shaker table chest to provide simultaneous agitation during 4-hour

Table 6.2: Comparison of size distributions, by size region, for 4-hour reaction time with simultaneous shaking and with varying *in situ* milling media.

Milling media	Vol% (±1%) Region I	Vol% (±1%) Region II	Vol% (±1%) Region III	Total Vol% Region I-III
no media	32	45	20	98
small media	40	36	20	96
large media	32	45	20	98
large & small media	41	48	7	96

hydrothermal treatment reaction. Different combinations of milling media sizes were explored, which included: large (1-inch diameter), small (½-inch diameter), and equal parts large/small media (by weight). Following hydrothermal treatment/reaction samples were decanted, washed

and oven-dried. These samples did not receive significant additional post-reaction *ex situ* milling, with small amounts *ex situ* milling and mortar & pestle proceeding oven drying, to break down larger aggregates for size analysis. The size distributions for these samples are shown for comparison in Figure 6.7, while the resulting volume fractions, calculated by integrating across each size region, are presented in Table 6.2.

The influence of constant shaking alone, during the 4-hour hydrothermal reaction, on the resultant particle sizes is evidenced by the significant decrease in the largest HA size fraction as

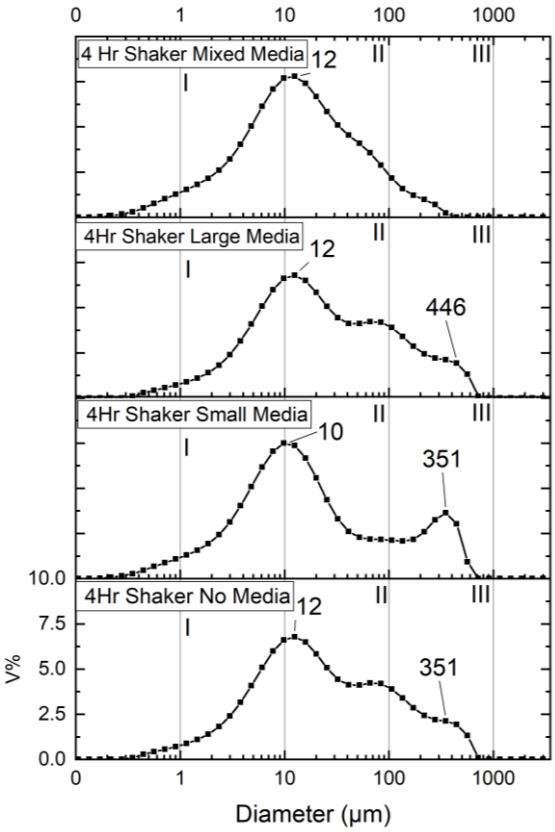

Figure 6.7: Particle size distribution for 4 hours of hydrothermal treatment.

With simultaneous shaking, with no ball bearings, all large, all small, and 50% small and large milling media.

compared to HA produced in a fixed reactor followed by ex situ milling (20% and 28%, respectively). When in situ milling is employed simultaneous with shaking, the results are varied.

For samples prepared using large milling media, the milling process appears to be largely ineffective, as illustrated by the similarities in the size distributions shown in Figure 6.7 and in the integrated volume fractions of Table 3. When only small milling media is used, the volume fraction of region I is increased, region II is reduced, and region III remains unchanged. Each of these results is consistent with a conventional understanding that larger materials require the use of larger media for effective milling. The largest effect on the size distribution, resulted when equal parts of large and small milling media were used, where the volume fraction of region III decreased by 13%, and both regions I and II increased such that their combined fractions accounted for 90% of the total material volume. In this case, the mixed media may act in a kind of stepwise fashion with the large media first breaking apart the larger particles and aggregates, allowing the smaller media to continue the refining process. While prolonged use of mixed media is generally not recommended as it can result in unwanted wear on the (smaller) media, this was not observed possibly due to the relatively short duration of the milling process employed here.

6.3.3 Scanning Electron Microscopy Imaging

Scanning electron microscopy (SEM) was used to help elucidate the makeup of the as-produced and milled HA. Specifically, the extent to which the dried as-synthesized HA particles were aggregated, and the varied particle morphologies present were qualitatively investigated. Representative micrographs, across multiple size scales, are shown without modification in Figure 6.8 for unmilled (A, B, C), and *in situ* milled (mixed media) (D, E, F), HA. The adhesive mounting media used to affix the HA powders is visible as the circular features in the largest area images of Figure 6.8 (A and D). In these same images, only the largest particles or aggregates are visible and appear similar in size regardless of whether *ex situ* or *in situ* milling was used. When viewed at higher magnification (10 μm scale, Figure 6.8, B and E respectively), some subtle changes in

particle size and morphology start to appear. For example, more of the particles in the *in situ* milled materials (Figure 6.8 E) appear to be smaller, while there appear to be fewer very large particles. The *ex situ* particles are also more crystalline in appearance.

At the highest magnification (Figure 6.8, C and F), particles with sizes on the order of tens of nanometers are clearly visible in both sample preparations. While there are qualitative differences in morphology and aggregation visible between the two samples, it is difficult to determine if this is sufficiently representative of the entire sample to warrant any significant conclusions.

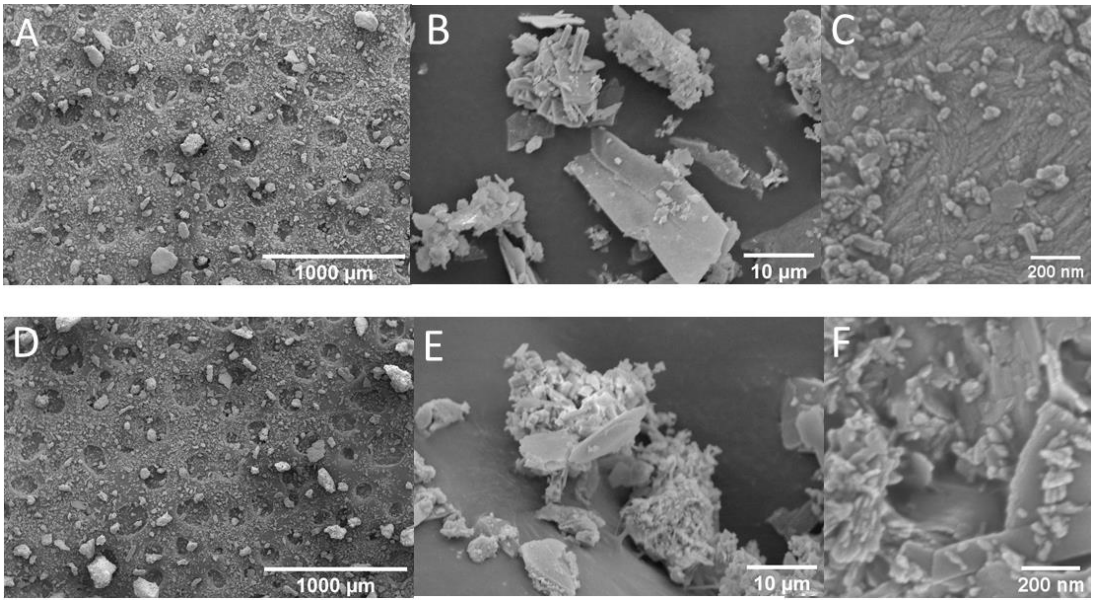

Figure 6.8: SEM Images of HA particles with increasing magnification.
Left to right. A-C) 4 hr synthesis, ex situ ball milling only. D-F) 4hr reaction with in situ milling and shaking.

6.3.4 X-ray Diffraction

X-ray diffraction data were obtained for all samples in order to assess the relative crystallinity of all samples as well as determine the crystalline domain sizes. Unlike the dry particle sizing method, which cannot quantify nanoscale particles near or below the optical diffraction limit or distinguish between nanoparticles and aggregates of nanoparticles, or SEM, which cannot

differentiate between amorphous and crystalline materials, XRD can determine the size of the crystalline domains of the particles, unobscured by aggregation. Representative XRD data across all synthesized HA sample types is shown in Figure 6.9, compared to the commercially available control (Figure 6.9 A), measured on our instrument. Here the primary characteristic HA peaks lie between 25 and 35 degrees and are visible in all samples. Compared to the control, each of the as-synthesized HA samples (B-E) exhibit relatively poor crystallinity as evidenced by the low overall XRD signal. The sample prepared with in situ milling (mixed media), Figure 6.9 E, appears to have the lowest crystallinity, which can be explained in part by smaller particle sizes in this sample. In this case, the smaller particles have more atoms at/near the surface (higher surface-to-volume ratio) which are more amorphous in nature. The crystallinity of this material can be improved by

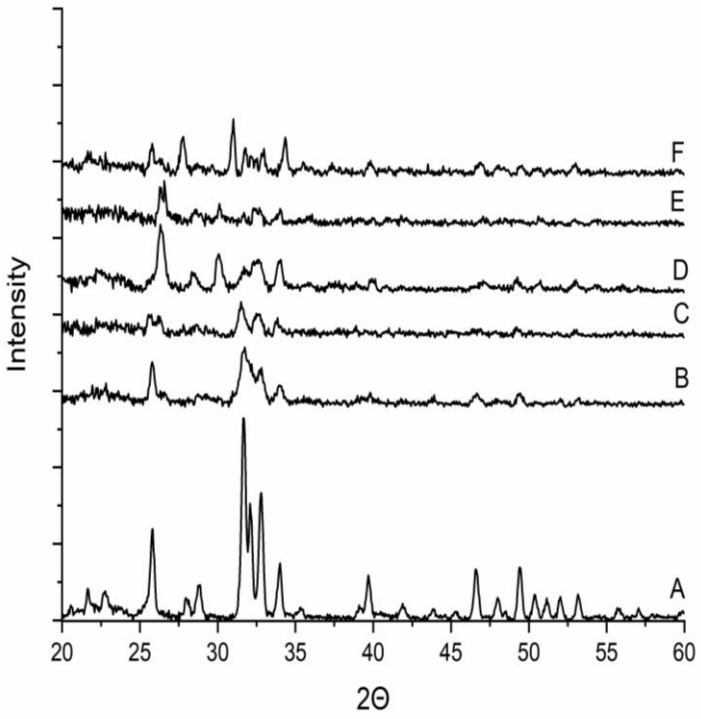

Figure 6.9: Comparison of XRD for HA samples.

A) Sigma, B) unmilled, C) 24hr ex situ milling, D) shaken but unmilled, E) shaken in situ milling with mixed media, F) shaken in situ milling with mixed media followed by sintering.

sintering, during which some of the amorphous surface atoms become part of the ordered lattice. This is illustrated in Figure 6.9 E which shows an increase in crystallinity of the aforementioned sample (Figure 6.9 E), following sintering (3 hrs, 950°C) [85].

$$l = \frac{K*\lambda}{ß*\cos(\Theta)} \qquad \text{(Eq. 6.1)}$$

The predominant size of the particles (or crystalline domain sizes) in each of the HA samples was estimated directly from the XRD data as diffraction analysis is not as susceptible, as the other methods employed here, to the effects of aggregation on determination. Here the Scherrer Eq. 5.1 is employed, where K (shape factor) is assumed to be 1, λ is 1.54 Å, ß is the line broadening coefficient, the actual peak width at half the maximum intensity (FWHM) at the Bragg angle, Θ. The selected Bragg angle in each sample is selected to correspond to well resolved and isolated peak positions, optimizing the confidence of the calculations. All Bragg angles as within the primary characteristic HA region. The Scherrer size analysis shows an average crystallite/grain size of 27.6 nm, across all sample types, with a standard deviation of 4.8 nm. The results for each sample are shown in Table 6.3. The largest sizes were for the Sigma, unmilled and 24 hr milled

Table 6.3: Comparison of calculated HA crystallite size

Using the Scherrer Equation (6.1), as purchased (Sigma) sample is compared to 4hr hydrothermal reactions (4 hr) with various reaction and milling conditions.

Sample / Milling conditions	Bragg angle (2Θ Degrees)	ß (FWHM)	Particle size (nm)
Sigma/ unmilled	25.7	0.3	30.5
4hr / unmilled	25.7	0.3	27.4
4hr / 24 hr *ex situ* milled	25.5	0.3	31.9
4hr / shaken *in situ* mixed media	26.3	0.4	22.1
4hr / shaken but unmilled	36.3	0.4	21.4
4 hr / shaken, *in situ* mixed media, sintered	25.7	0.3	27.5

HA samples at 30.5, 27.4, and 31.9 nm, respectively. The smallest crystallite sizes were calculated for the shaken samples, with sizes for the *in situ* milled (mixed media) and media-free samples of 22.1 nm and 21.4 nm, respectively. This result may suggest that HA crystals formed during synthesis are relatively fragile. It may also indicate that simple agitation through shaking is an effective intermediate step for size reduction.

6.4 Hydroxyapatite / Cellulose Nanofiber Composite

Proceeding synthesis, characterization of HA CNF composites followed. Composites were manufactured similarly to mineral oxide composites, with the use of the Hobart mixer. However, the use of acid was not warranted, as HA does not require an acidic environment to maintain surface charge repulsion. When manufacturing HA composites low weight percent were initially

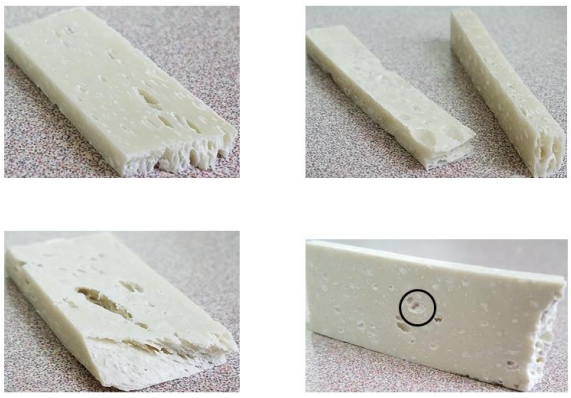

Figure 6.10: Hydroxyapatite composites
Top left) 0.5%; Top Right) 1%; Bottom Left) 5%; Bottom Right) 20% (circle indicating void space of powders)

tested as a proof of concept, then higher weight percent composites were manufactured in an attempt to mimic natural bone with higher weight percent HA. However, higher weight percent composites were noticed to be highly flawed, mainly due to the HA powder aggregates that were not dispersed throughout the CNF. This produced void spaces within the CNF system and lead to

premature failures. This was noticed exclusively with previous manufacture processing, speed 2 for 3 minutes, the image of multiple Wt% HA CNF composites can be seen in Figure 6.10.

Preliminary flexural modulus associated with low weight percent composites were shown to be sufficiently high, with 0.5 Wt% HA composite specimens displaying flexural moduli that

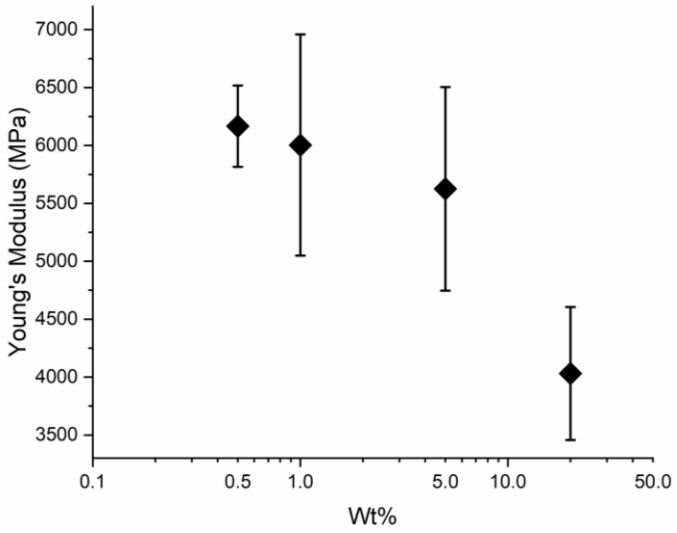

Figure 6.11: Flexural Modulus of hydroxyapatite composites

were comparable to previously made mineral oxide composites. When increased to 1 Wt% it was observed that specimens exceeded that of the 500 N force transducer on the INSTRON, this caused premature test conclusions due to a safety feature of the instrument. This leads to inconclusive results for test specimens while causing specimens to become null and void for the test. As such testing specimens were cut in half widthwise as to not interfere with the elastic modulus (Eq 4.1). This proved to be effective in allowing specimens to be tested successfully while recording specimens without exceeding the 500 N transducer. However, this did lead to so discrepancy within the testing as pore location was then limited within the decreased width, along with pore location fiber reinforcement of bending area was also decreased. Flexural modulus of HA composites is shown in Figure 6.11.

After testing flexural modulus porosity of all HA composites were calculated. All porosities of manufactured HA composites are shown in Figure 6.12. At 0.5 Wt% porosity was shown to be relatively high at 24%, at 1 Wt% it was shown that porosity increased, however on further inspection of 1Wt% HA discrepancies were shown to arise. As specimens were cut in half widthwise to mitigate load cell overloading, this also increased density shown from samples, this differentiated specimens from previously tested composites. Additionally, 5% HA composites were shown to be lower than that of 1 %, as these samples also were manufactured in a manner to mitigate load cell overloading, and due to increased weight of HA additives higher densities were shown to arise creating a higher ration of calculated CNF vs know densities of CNF, this, in turn, lowered porosities of samples. 20% HA showed similar problems as weights of CNF present in specimens were significantly lower than previously tested metal oxide specimens.

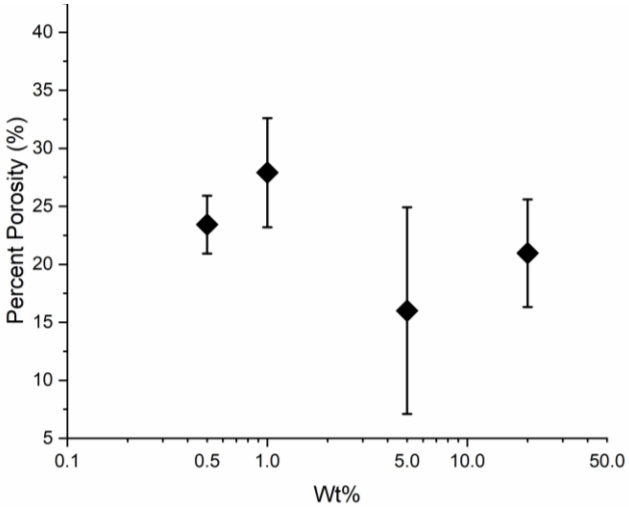

Figure 6.12: Porosity of HA composites

Shore D hardness of HA composites was shown to increase with initial impregnation of HA in CNF as shown in Figure 6.13, with 0.5 Wt% composite displaying Shore D hardness of 76 and 1 Wt% displaying a Shore D hardness of 84. It was then shown that Shore D hardness of HA composites relatively plateaued, staying near this 84 Shore D hardness. The variation between

individual specimens was similar for many Wt% HA composites, except for specimens at 20 Wt% which showed higher variation than any other HA composite. This was likely due to the void spaces of HA powder which did not provide sufficient resistant for the indenter.

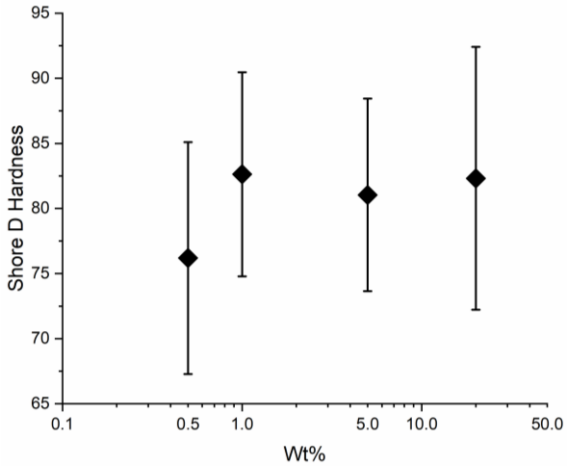

Figure 6.13: Shore D hardness of HA composites

6.5 Discussion

Following characterization of as-synthesized HA, it was shown that 20 nm crystals were produced which is analogs of known sizes of naturally occurring HA. However, it was discovered that even with *in situ* BM, aggregates of HA were still discovered, whether this was from hydrogen bonding with leftover water in the HA lattice or charge bonding between the HA is still unknown. It was discovered that BM i*n situ* did, in fact, break apart many of these aggregates, along with this BM did not cause any chemical impurities to arise in synthesized HA. After synthesis of HA *In situ* powders, implementation of said powders into CNF was conducted, with initial success, it was shown that HA would not homogenously disperse throughout the CNF through previous mixing procedures. This was especially true with higher Wt% HA composites. This lack of dispersion caused void areas, void areas lead to weaker flexural modulus for specimens.

One solution to monodisperse HA is the use of a supermasscolloider, similarly to the masscolloider used to break down fibers of cellulose to create the CNF. This device uses grinding plates in close proximity to tear fibers apart, as such it would be able to break down any of the aggregates and evenly disperse them throughout the CNF as it is being made. Additionally, previously made CNF HA composites cell culture testing has been successful. This, however, seems to be more positive for lower weight composites than higher weight composites. The cause of this is still unknown and is to be investigated further with more dispersed composites. One cause may be the fact that HA is concentrated in some locations which have been shown to potentially be toxic to cells in close proximity to higher concentrations. Also, as there is no flow of nutrients it is difficult to give the cell the required means to effectively grow on CNF HA composites. As such a larger organism study should be conducted to obtain a better understanding of the CNF system as a whole.

CHAPTER 7

WATER DECOMPOSITION OF CELLULOSE NANO-FIBRILS

7.1 Water Decomposition of CNF Composites

As mentioned, potential complications surrounding PLA/ PGA medical devices, dissolution rate, and acid decalcification, have been a leading concern in their orthopedic uses. As they tend to lose mechanical properties within the first 5-8 weeks after implantation and a complete loss in mass within 6-12 months[31]. During which time the devices experience non-specific scission of the ester groups, releasing acids into the surrounding local environment and typically cause aseptic loosing of fixations. If acids are not efficiently excreted by the host local decalcification can occur, leading to improper bone formation and increased degradation time of bone fiction devices[31]. With ideal bioabsorbable orthopedics requiring initial substantial modulus, then a sharp decrease in modulus within the first two weeks of bone healing during vascularization phase. Proceeding two weeks the fixation device should have a gradual decrease in modulus over a 2-month period. After 2 months cortical bone mechanical properties are reestablished meaning fixation modulus is minimally required for stabilization of the bone. Material over this time should resist physical changes, both swelling and softening should be minimal for the first 2 months. Allowing cell propagation into the orthopedic device reinforcing the orthopedic and reducing the need for it after a period of time.

7.2 Methods

7.2.1 Materials and Setup

For use in water decomposition testing of CNF specimen's plastic containers were purchased as water baths, each water bath had a water flow inlet and outlet drilled in at a specified

waterline. A chiller with pumping system (Neslan instruments. INC RTE-5DD) was used to circulate water and heat it to desired temperatures, each water bath and chiller had a designated digital temperature reader, temperatures were kept at a constant 37°C ± 2°C. Within both water bath (49.1L storage container), several sealable glass containers (2 X 4.75 X 6.5 in) were placed within, each glass container housed 550 ml of SBF solution and a holder seen in Figure 7.1.

For nine CNF specimens. Holders were made of acrylic due to acrylics inertness in aqueous solutions, holders were cut using a plasma beam cutter (Full Spectrum PS-36) and washed proceeding cutting to remove possible carbon on cut acrylic, holders were made using dimension as displayed in Figure 7.2.

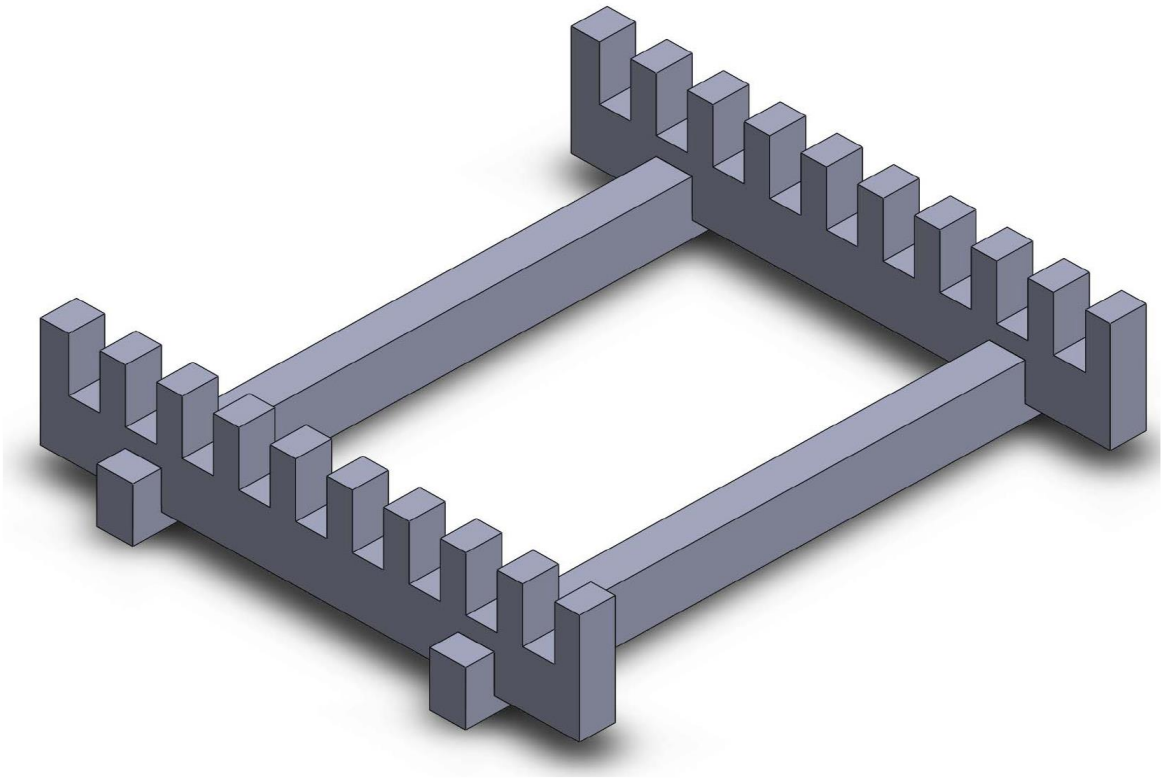

Figure 7.1: Assembled specimen holder

Holders were then epoxied together to prevent movement and possible tearing of held specimens, specimens were held vertically lengthwise and placed into glass containers. A shelving unit was constructed to house the water baths, which can be seen in Figure 7.3, along with the setup for long term water decomposition testing. Each component of the setup is shown, image 1 shows the heat source and water pump for the entire system and the return, 2 is an image of the water bath with specimen containers housing the acrylic holders, 3 shows the thermal detector that was used to monitor the water baths temperature (Digital thermometer 6802II, & Edtech digital thermometer HD200), 4 shows the gravity-driven outlets from the first water bath to the second water bath.

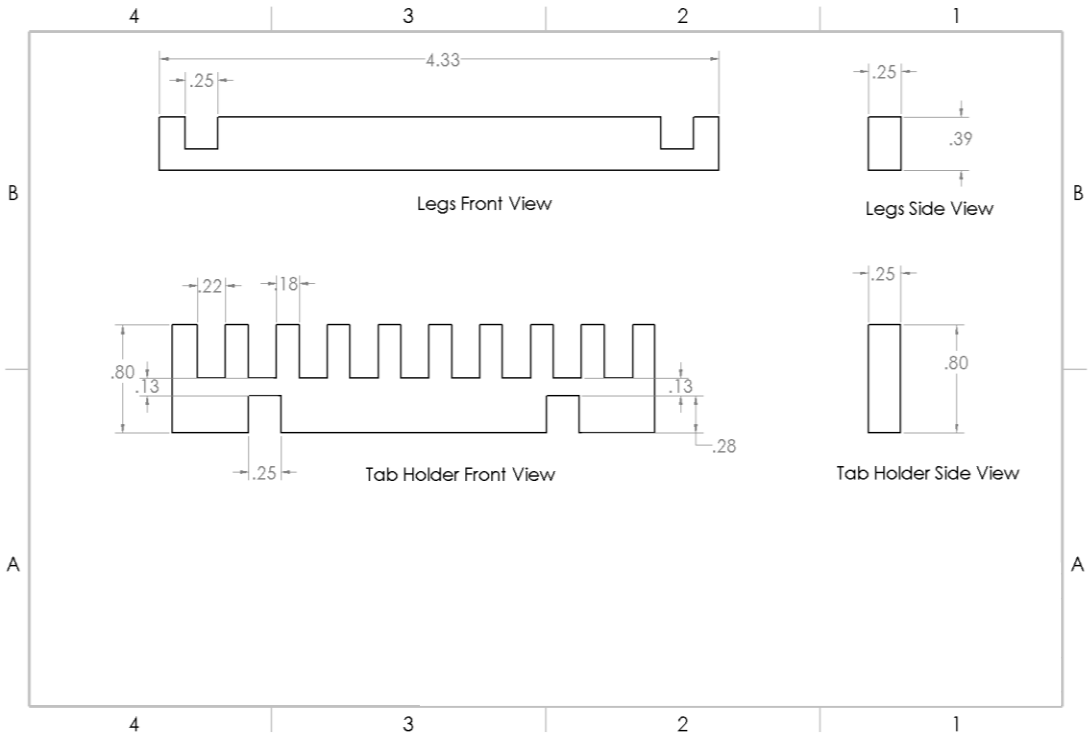

Figure 7.2: Dimensions of individual holder pieces

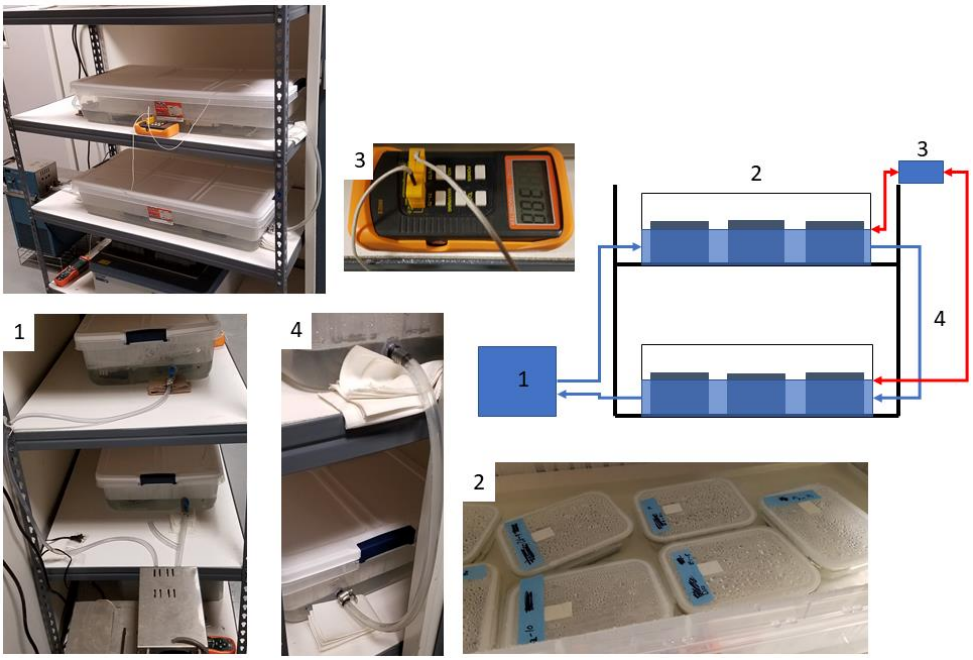

Figure 7.3: Long term set up of water decomposition testing

Short term testing placed glass containers, housing 550 mL of solution and 36 specimen tabs for a total of 4 specimens tested at each time point, into an oven (Model) for ease of testing parameters. Specimens were prepped in three different procedures. Dry specimens were prepped for 48 hours within an oven to remove any remaining moisture. After 48hr specimens were weighed and volumetrically measured then placed into a bag with a desiccant for 24hr to regulate temperature to room temperature. Slightly wet specimens were prepped in a moisture remover before machining, proceeding machining specimens were placed into bags with desiccant packets. Wet specimens were prepped without any drying throughout the machining process and were placed into bags without desiccant packets.

7.2.2 Experimental Procedures

Experiments initially were held for 5 months with 3 specimens tested at each time point. Tests were conducted at 0 hours, 1, 3, and 7 days, then weekly for the remainder 5 months. Total

specimens tested per trail were 69, with each glass container holding 9 specimens each. Additionally, short term testing was conducted at time points 0, 15, 45 min, 1 hr, and hourly for 6 hours later. Weight of specimens was obtained before testing along with volumetric measurements. Upon extraction from glass containers, the specimens were dapped with a lab-grade paper towel to remove excess water, then weighed and new volumetric measurements were taken. After 3-point bending testing, as previously performed in past specimen trials, specimens were Shore D hardness testing was performed. The specimens were then dried to completion after 48hr and weighed again. This procedure is repeated for each time point and until the completion of each trial. From gathered data 3 equations were used to predict material loss Eq. 7.1, water gain Eq. 7.2 in tandem with Eq. 7.3, and volume increase Eq. 7.4 in tandem with Eq. 7.5.

$W_L = W_I - W_d$ (Eq. 7.1)

W_L = Weight loss

W_I = Initial Wight

W_d = Dry Weight after Testing

$W_G = W_W - W_I$ (Eq. 7.2)

$W_{\%} = \frac{W_G}{W_I}$ (Eq. 7.3)

W_G = Weight Gain

W_W = Wet Weight

W_I = Weight Initial

$W_{\%}$ = Water percent

$V_G = V_W - V_I$ (Eq. 7.4)

$V_{\%} = \frac{V_G}{V_I}$ (Eq. 7.5)

V_G = Volume Gain

V_W = Wet Volume

V_I = Volume Initial

$V_{\%}$ = Volume Increase percent

7.3 Results

7.3.1 Long Term Results

Long term testing of pure CNF specimens demonstrated poor initial results. With the material displaying significantly decreased flexural modulus in just a meager 24 hours as shown in Figure 7.4. After this initial 24 hours modulus began to decrease gradually and plateau below 100 MPa. Between day 20 to day 28, it was noticed that Young's modulus increased, this was investigated, it was noticed that within the containers microbial growth was present. As specimens were not initially sanitized and were not kept in a sanitary environment, growths could have been the cause of numerous sources, growth can be seen in Figure 7.5.

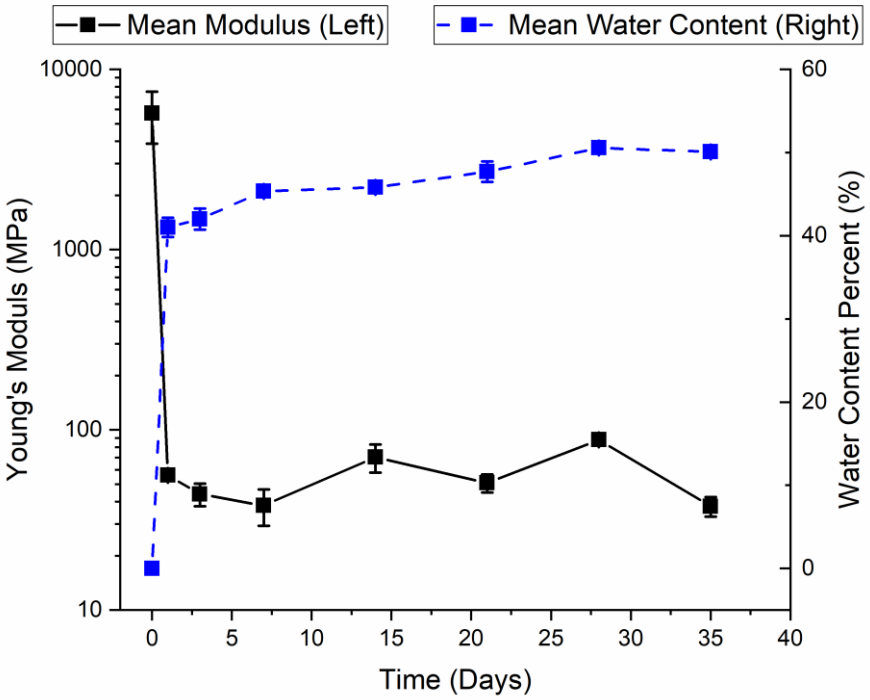

Figure 7.4: Young's Modulus (left axis) and water content percent (right axis) vs time

Along with this modulus loss the percent water uptake recorded also had a tremendous increase in only 24 hours increasing to around 40%. After this initial increase, the water uptake

plateaued akin to that of Young's modulus. The one aspect of long-term testing that showed promise for the system was material loss over time, which was minimal at best, displayed in Figure 7.6.

Figure 7.5: Image of microbial growth

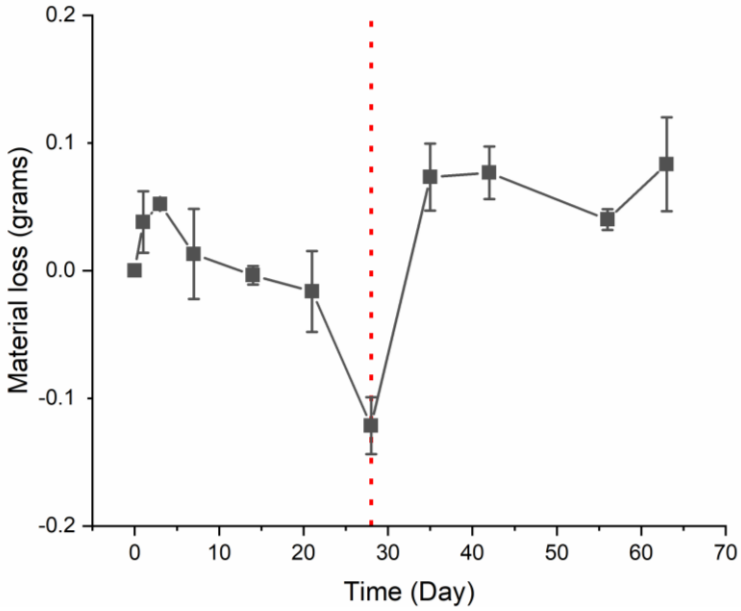

Figure 7.6: Material loss vs time (Days), red line additional sodium azide

As seen in the material loss within the days 20-28 there was an increase in the mass of the specimens, this increase coincides with the increased modulus and verifies the evidence of microbial growth and the propagation of this growth throughout the CNF specimens reinforcing the specimens. After day 28 microbial growths were shown to be eradicated using additional sodium azide, subsequently after this addition modulus decrease, and material loss returned to their expected trends. However negative results were, this test is the first of its kind on this material system as a bulk, displaying areas in much need of engineering changes.

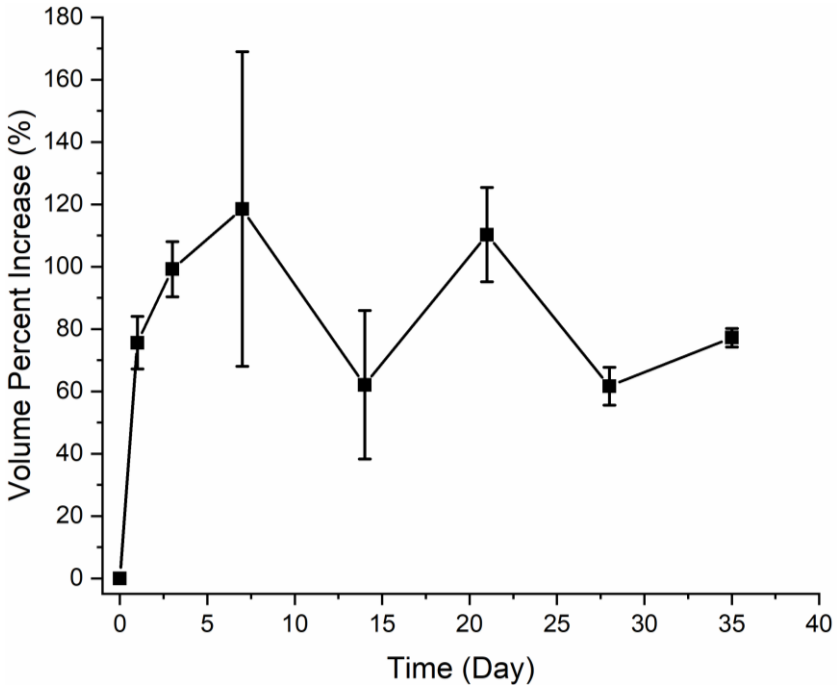

Figure 7.7: Volumetric change percent vs time (Days)

Proceeding material loss volume change was investigated, this was done using Eq. 7.5 to view the volume percent change displayed in Figure 7.7, with 0 being initial volumes. After 1 day of being in solution volume gain was recorded at 78% this is over a 3/4 increase in volume in just 24 hours, proceeding this volume were shown to increase again. At 7 days a maximum volume increase was displayed, contradictory to this increasing trend at day 14 there was shown to be a

decrease in percent gain then again at day 21 volume percent increased, and this oscillating volume percent continues. The cause of this discrepancy is not yet known.

Water percent increases also led to the material swelling and a decrease in shore hardness. This seems to be a nontrivial notion for the material, as in bulk CNF is extremely hydrophilic and expands when wet, as evident to the 3Wt% slurry precursor. As the material became wetted and swelled it also softened, making it easy for the micro indenter to penetrate the system. Shore D hardness of all testing incidents was taken as shown in Figure 7.8. From initial time point, Shore D was shown to be 86, following this at 24 hours after conducting water decomposition testing shore hardness was shown to be 18. This Shore D was then held relatively consistent with the remainder of the test, with slight variations at day 28 and 35 which displayed Shore D hardness's of 10 and 21, respectively. From the results of Shore D hardness, a correlation between water percent gained and loss in the durability of samples was discovered.

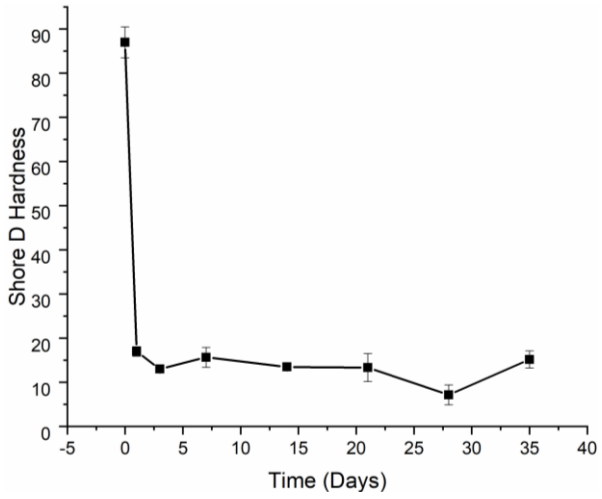

Figure 7.8: Shore D hardness vs time (Days)

7.3.2 Short Term Results

From results gathered in long term testing a short 5-hour testing period was considered, this allowed for a more precise monitorization of the material changes and obtain a baseline for when material changes occur. For this test, three different initial water contents were investigated, with mostly dry, semi-wet, and wet. This was to view if the material properties changed significantly even when the material started out in a wetted state. 4 testing specimens were examined at each time point. When removed each specimen was dapped onto a paper towel to

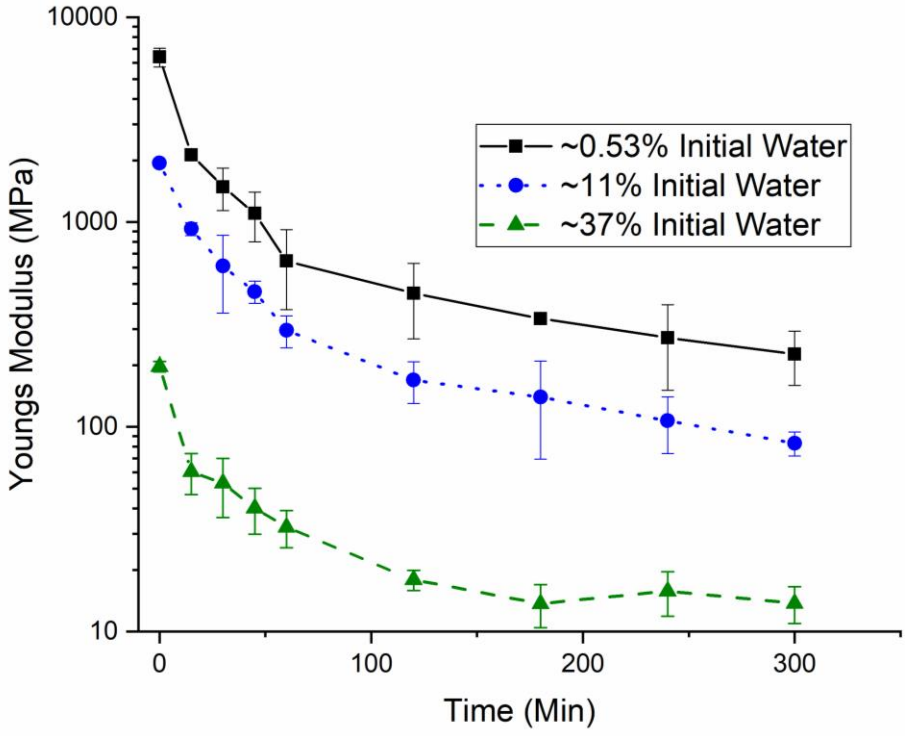

Figure 7.9: Young's modulus over time of different initial water contents

remove the excess water on the edges of the material. Specimens were weighed and volumetrically measured.

As shown in Figure 7.9, time 0-minute test specimens showed increased flexural modulus when compared to its later counterparts when in vitro testing, this was displayed for all initial water

content specimens. However, initial starting modulus for each type of specimen was different, with the driest specimen showing significantly higher Young's modulus when compared to the wettest specimens, with the semi-wet specimens falling somewhere in between.

Driest specimens began at around 7 GPa with an initial sudden decrease in modulus around 15 mins to 50 mins, after this time gradually decrease in Young's modulus is observed over time. Similarly, with semi-wet specimens began at 2 GPa within the first-hour modulus was shown to decrease at a steady rate then proceeding this time gradual decrease in Young's modulus is noted. With the wettest initial CNF specimen, this sudden decrease in modulus is noticed within the first 15 mins as similarly with the first two initial wetted samples. After 15 mins flexural loss became gradual until the finishing of the 5-hour test. Displayed with all specimens after 1-hour flexural modulus loss was gradual until the end of the testing period.

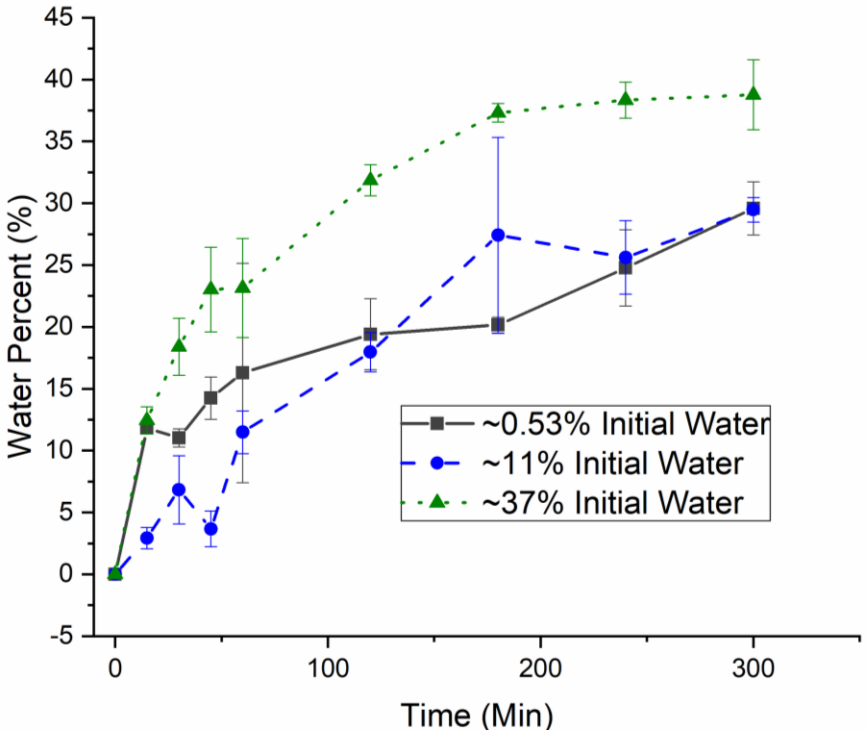

Figure 7.10: Water content percent vs Time (Min) of different initial water contents

For each initial water content specimens, water gains were calculated and shown in Figure 7.10. For 0.57% initial within the first 15 minutes, water percent gained was 14 along with 37% initial, 11% initial content showed the lowest water gain in the first hour. After the first two hours, 0.57% water percent gain was 17% along with 11% initial which was slightly lower at 16%. However, at 2 hours, 37% initial water percent showed a water gain of 33%, this trend of wettest initial water content CNF displaying higher water percent gain continued for the duration of the test. At 180 minutes there was a shift in driest initial and semi-dry initial water content CNF specimens, with driest at 17% and semi-wet at 27%. However, at 240 minutes water percent of driest CNF specimens and wettest CNF specimens were shown to become similar and this similarity remained for the remainder of the test.

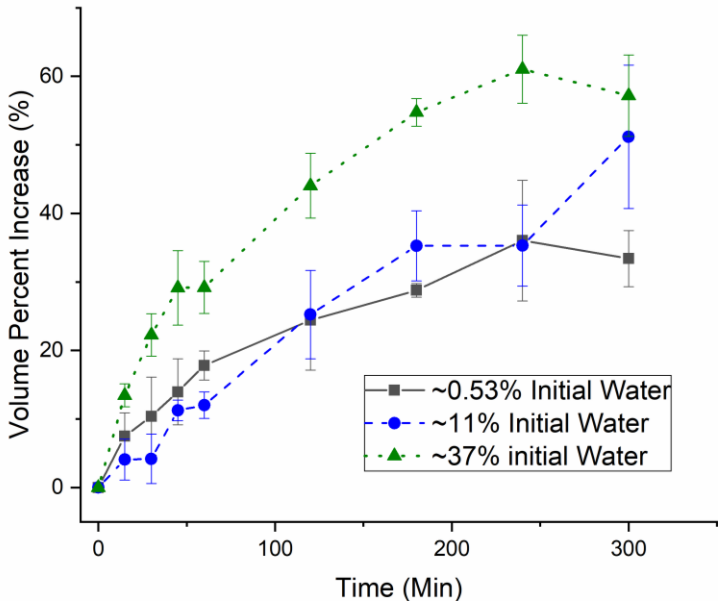

Figure 7.11: Volume percent increase of day trial CNF

Volume increase for all specimens were calculated using Eq 7.4 and 7.5 after is shown in Figure 7.11, for driest CNF samples a gradual increase in volume was recorded with time points 15 minutes to 1 hour increasing slowly to 20% volume increase. Alternatively, for semi-wet specimens, this increase was seen to be sporadic, with increase happening in increments with the

total volume increase after 1 hour only reaching 16%, while wettest specimens proceeding the 1st hour showed a volume increase that was much higher at 30%. At 2 hours driest and wettest specimens displayed nearly similar in volume percent residing at 22%, while wettest specimens displayed 43% volume increase. Volumes for driest and semi-dry specimens after 2 hours were shown to interject on time periods, then following at alternative time periods semi-wet specimens were shown to be higher than dryer specimens, this pattern was shown to persist for the remainder of testing periods. Whilst wettest specimens continued to increase in volume until time 240 minutes whereafter volume showed a decrease. At the conclusion of volume increase analysis, wettest specimens were shown to increase the most followed by semi-wet and finally driest CNF specimens. However, why there was a sudden drop in volume displayed by wettest specimens is not yet known and will require additional testing.

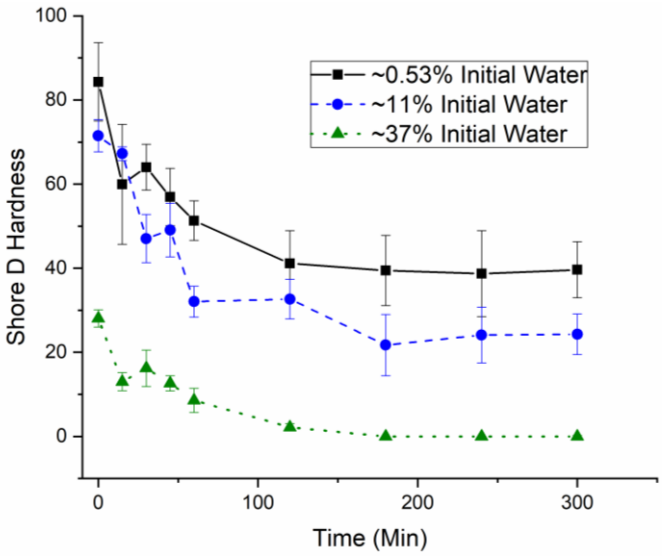

Figure 7.12: Shore D hardness of initial water content CNF specimens vs time (minutes)

Shore D hardness of all initial water content specimens was taken proceeding each individual three-point bending test and averaged for each sampling period, shown in Figure 7.12.

As predicted from other tests and calculations driest CNF specimens displayed the highest Shore D hardness, followed by semi-wet CNF and finally by wettest CNF specimens. Initial time period Shore D hardness was 88, 75, and 30 for driest, semi-dry, and wettest CNF samples, respectively. At 15 minutes driest samples displayed a sharp decrease in Shore D hardness, along with wettest CNF specimens. Semi-wet specimens displayed slightly decreased Shore D hardness of 74 at minute 15. Following this time point for driest and wettest CNF samples a gradual decrease in Shore D hardness was displayed until hour 2 when thereafter Shore D hardness plateaued. For semi-wet samples, after 15 minutes there was a sharp decrease followed by a slight increase at minute 45. Proceeding at 1 hour a decrease in Shore D hardness is noticed and maintained until hour 2, where after a plateau is displayed.

7.4 Discussion

Testing of CNF specimens in aqueous solution for maintained periods of time has not been investigated previously, as such a unit that can assess materials decomposition in aqueous solutions at biological temperatures for long periods of time was established. However, from the initial 24-hour data, it was shown that this may not be an effective method of testing for pure CNF specimens and many other testing composites in the future. As shown CNF specimens degraded expediently inside aqueous solution loosing significant amount of flexural modulus within the first 24 hours and then maintaining this low flexural modulus, additionally water gained within the first 24 hours was substantial, reaching close to 40% gained, along with an increase in volume at 75% gain and displayed extremely low Shore D hardness.

Following poor initial testing with long term testing. one-day testing proved to be an effective way to screen specimens before a long-term investigation of materials were undertaken. From one day trails, it was found that completely dry specimens displayed the most promise with

higher flexural modulus and shore D hardness over 5 hours along with lowest water gain and volume increase over the sample time period. Additionally, it was shown that semi-wet specimens showed the least consistent results from water content, volume gain, and Shore D hardness, with initial hours showing results that were all over the place. Wettest specimens showed the highest water and volume gain, along with lowest Shore D hardness and flexural modulus, this was most likely due to water being capable of penetrating the already spongy material and deteriorate the specimens further.

However, testing methods within this set up are ultimately flawed when compared to the intended use of devices. As bone tissue interfaces do not contain enormous amounts of fluid, devices would only be exposed to small amounts of fluids and would only be exposed to fluids on one side. This means current testing would be examples of a worst-case scenario where the wound became extremely septic. One such solution to this flaw would be the use of a diffusion interface on one side of the device which would act as the tissue interface, this would simulate a more accurate environment for the device. Along with these changes, composite materials will need to be investigated, as some materials display low solubility, they could provide support to the CNF as it softens.

CHAPTER 8

CONCLUSION

8.1 Summary

With CNF being an abundant relatively new material research of said material has been taken on by a plethora of research groups each investigated different applications. One such application which was investigated throughout this thesis is within biomedical materials. As explained biomaterial for the intended use in bioabsorbable orthopedics requires a specific flexural modulus that degrades over time. Additionally, the material should display marginal signs of being biocompatible, not eliciting negative immune-responses or cause harm to host tissue over time.

Within chapter 1 the use of composite materials within CNF was investigated, these composite materials were mineral oxides that are already commonly used within orthopedics currently. It was shown that changes within the CNF environment such as pH adjustments can facilitate these mineral oxides with initial use characteristics. As many mineral oxides have surface charges pH of CNF environment is crucial in maintaining these charges. This inhibits individual particles of the mineral oxide from aggregating together, this was backed by SEM imaging of thin films of dried CNF composite films. In which it was shown particles originally around 20 nm were preserved in CNF that was treated with acid levels near particles isopiestic point.

Physical characteristics of mineral oxide CNF composites were investigated in chapter 3. The three characteristics analyzed from composite CNF were flexural modulus or Young's modulus, porosity, and Shore D hardness. For all chosen mineral oxide composites these physical characteristics change drastically, mainly due to mineral oxides hydrophilicity. As this would cause composites to become more plastic than elastic, tearing instead of breaking. This caused

some composite specimens to have lower flexural modulus then others. This also caused the specimens to become soft with low durability, decreasing their Shore D hardness. Increase in water content also causes discrepancies in porosity calculations leading to unreliable data and skewed results, usually leading to porosity results that are lower than they should be. It was found that titanium dioxide and aluminum oxide composites showed the most promise with increased flexural modulus, Shore D hardness, and porosity.

Chapter 4 investigated pure CNF that was mechanically manipulated for set periods of time at various speed, then at a set speed for various times. From varying speed testing, it was shown that flexural modulus, Shore D hardness, and porosity would change depending on the speed used. Speeds of 1 (72 rpm) produced some of the highest flexural moduli, along with the lowest porosity, as slow speed did not incorporate air into the system. Other speeds such as speed 3 and 4 also showed improved flexural modulus's while maintaining some porosity, showing that potential fiber rearrangement could have taken place resulting in stronger specimens. Speed 2 provided specimens with the highest porosity yet decreased flexural modulus when compared to all other speed variant specimens. As such speed 2 was chosen for time variation testing when the time was increased it was shown that flexural modulus would increase, while still displaying constant porosities. Furthermore, it was shown that longer times did not improve the specimens by a significant amount, suggesting that there is an optimum time that should be taken into account.

As hydroxyapatite is a known naturally occurring mineral its synthesis and use in CNF was investigated in chapter 5. Synthesis of HA was done so in a manner that was simplistic and could create HA that was similar to bone HA in chemistry and size. Throughout synthesis the use of *in situ* ball milling was utilized, this allowed for control over particle size of synthesized HA. FT-IR was used to monitor HA powders for chemical compositions and any impurities that may arise in

the use of *in situ* ball milling, as no such impurities were shown it was assumed that ball milling did not distribute any impurities into synthesized HA. It was found however that CO_3^- substitutions in HA would occur, this was later found out to be caused by CO_2 in the overhead space inside the hydrothermal reactor, and as carbonated HA has been shown to be common in the natural bone it was an adventitious impurity. SEM imaging was used to observe the morphology of synthesized HA, particle size was shown to be roughly near 20 nm which was theoretically calculated from XRD and visually from SEM images. HA CNF composites were produced and tested for similar physical characteristic as mineral oxides. Initially at low Wt% results were shown to be promising, with 1 Wt% exceeding the load cell, leading to shortening widths of specimens. This however created specimens that were more susceptible to premature failure due to porous structures. At higher Wt%'s it was shown that HA would aggregate together creating void spaces of powders which did not improve structural properties of CNF.

Degradation of CNF in aqueous solutions was investigated in chapter 6. Initially, long term trials were to be conducted, however, after the first 24 hours, poor results resulted in the use of shorter-term trials of water decomposition. Additionally, with long term trials, it was discovered that the use of our antimicrobial sodium azide was administered in low concentrations allowing for growth to occur on CNF, this cause increases in modulus and caused skews in material loss displaying more weight than original specimens. Additionally, volume gain was shown to be significantly high for specimens after a few days, with variations in volumes occurring over time. Through day trials three different initial water content specimens were investigated. It was shown that driest specimens of CNF outperformed all other initial water contents in all characteristics viewed. Semi-dry specimens followed with wettest initial specimens displaying the worst progression of all characteristics. Still, water decomposition of pure CNF was shown to be

expedient even with initially dry conditions, as such providing an additional necessity for additives that can provide structural support to the expedient degrading CNF.

8.2 Future Work and Recommendations

From work described only low Wt% of composites has been investigated, as the natural bone is comprised mainly of minerals with low Wt% being collagen, higher mineral oxide and HA Wt% percent composites should be investigated. With considerations being taken from void space of powders being produced from 20 Wt% HA, monodispersity of the mineral should be of high priority. Additionally, the manufacturing of mixed composites should be investigated as HA or titanium would be potentially stiff materials but may not provide sufficient contrasting when imaging, as such material such as iron oxide, should be incorporated to allow for appropriate contrasting with radiology. Potential solutions which were discussed include the use of the mass more colloid to grind mineral oxide into CNF as CNF is being mechanically deconstructed, this would allow for even distribution throughout the CNF. However, due to time constraints and personnel changes the user of this device was never investigated. The use of the industrial mixer when producing CNF composites could also be used in the future with varying speeds and times to view effects with higher Wt%'s, as this could potentially create dispersed mineral CNF composites.

With physical characteristics, steps should be taken to ensure testing procedures and equipment meet standards within the orthopedic. Additional equipment to invest in is a four-point bending attachment for the INSTRON as this is used in many ASTM's that refer specifically with orthopedic fixation devices. Along with new equipment for the INSTRON a surrounding enclosure should be invested in, as some specimens experience catastrophic failure resulting in debris projecting from the testing site, one such adventitious enclosure would be a big box which would

also provide biological temperature for the duration of the testing. Proper analysis of porosity, i.e pore distribution, and interconnectivity, should be established as current methods used to have many flaws, especially with composites, and only displaying apparent percent porosity. Shore D hardness testing should be standardized with locations on each specimen being indicated and tested with a mean value of Shore D hardness being calculated henceforth, this would display proper durability of testing specimens instead of allowing users to determine Shore D hardness at their own discretion.

With many potential composite materials focus should be established, this means that only two potential composite materials should be investigated in earnest instead of limited research on all materials. This would allow for increased understanding of materials used and would direct the system in new directions, the materials in consideration are HA and glass fibers or bioactive glass. As these two materials have shown in literature promise with osteoinduction and cellular interactions. Additionally, they have both been shown to provide similar PLA and PGA structures with flexural modulus near 20 GPa which is a goal with this material system. Bioabsorbable orthopedics requires a multitude of physical characteristics one should be targeted at a time, mainly flexural modulus, then the material should be engineered to degrade in aqueous and biological fluids at a controlled rate. Physical models and prototypes of bone fixation plates and bone screws should be manufactured as well and tested, as testing specimens do not have the necessary holes for attachment, they do provide false positives for potential materials. As screw holes add a new potential weak point in the device abundant testing will need to be performed to confirm that materials can maintain this 20 GPa flexural modulus. Additionally, testing of CNF screws and pins should be investigated in tandem with bone fixation plates.

As with many orthopedic devices in the future testing of devices will need to be outsourced to labs and facilities that have been certified and adhere strictly to the ASTM standards and standards set by the FDA. Such testing would consist of physical properties of the material and cellular interactions. A cellular culture which is the preliminary step before animal trials will need to be completed in the respectively close future, with clinical hopefully proceeding animal trials. However, as the material is still relatively new and outsourcing to other facilities to perform testing is costly, more testing in-house will need to be done at expedient paces while adhering to the strict testing methods set out by ASTM and ISO.

REFERENCES

1. Clarke B. Normal Bone Anatomy and Physiology. :131-139. doi:10.2215/CJN.04151206
2. Nobakhti S, Shefelbine SJ. On the Relation of Bone Mineral Density and the Elastic Modulus in Healthy and Pathologic Bone. *Curr Osteoporos Rep*. 2018;16(4):404-410. doi:10.1007/s11914-018-0449-5
3. Murphy W, Black J, Hastings G. Cancellous Bone. *Handb Biomater Prop Second Ed*. 2016:v-vi. doi:10.1007/978-1-4939-3305-1
4. Barrère F, Blitterswijk CA Van. Bone regeneration : molecular and cellular interactions with calcium phosphate ceramics. 2006;1(3):317-332.
5. Chaudhry AA, Knowles JC, Rehman I, Darr JA. Rapid hydrothermal flow synthesis and characterisation of carbonate- and silicate-substituted calcium phosphates. 2012;28(3):448-461. doi:10.1177/0885328212460289
6. Fathi MH, Hanifi A, Mortazavi V. Preparation and bioactivity evaluation of bone-like hydroxyapatite nanopowder. 2007;2:536-542. doi:10.1016/j.jmatprotec.2007.10.004
7. Iain H. Kalfas, M.D. FAC. Principles of bone healing. *Nurosurg Focus 10*. 2001;10(4):1-4. doi:10.3171/foc.2001.10.4.2
8. Bacabac RG, Mullender MG. Mechanobiology of bone tissue Mecanobiologie du tissu osseux. 2005;53:576-580. doi:10.1016/j.patbio.2004.12.005
9. Gusmão CVB de, Belangero WD. How Do Bone Cells Sense Mechanical Loading? *Rev Bras Ortop (English Ed*. 2015;44(4):299-305. doi:10.1016/s2255-4971(15)30157-9
10. Xiao Y, Xiang L, Shao J. Bone morphogenetic protein. 2007;362:550-553. doi:10.1016/j.bbrc.2007.08.045
11. Ashman RB, Jae Young Rho. Elastic modulus of trabecular bone material. *J Biomech*. 1988;21(3):177-181. doi:10.1016/0021-9290(88)90167-4
12. Rho JY, Tsui TY, Pharr GM. Elastic properties of human cortical and trabecular lamellar bone measured by nanoindentation. *Biomaterials*. 1997;18(20):1325-1330. doi:10.1016/S0142-9612(97)00073-2
13. Rho JY, Ashman RB, Turner CH. Young's modulus of trabecular and cortical bone material: Ultrasonic and microtensile measurements. *J Biomech*. 1993;26(2):111-119. doi:10.1016/0021-9290(93)90042-D
14. Bayraktar HH, Morgan EF, Niebur GL, Morris GE, Wong EK, Keaveny TM. Comparison of the elastic and yield properties of human femoral trabecular and cortical bone tissue. *J Biomech*. 2004;37(1):27-35. doi:10.1016/S0021-9290(03)00257-4
15. Thomsen P. Material Science , Surface Science , Engineering , Biological Responses. 2001.

16. Nasab MB, Hassan MR, Sahari B Bin. Metallic Biomaterials of Knee and Hip - A Review. 2010;M:69-82.

17. Navarro M, Michiardi A, Castan O, Planell JA. Biomaterials in orthopaedics. 2008;(July):1137-1158. doi:10.1098/rsif.2008.0151

18. Gepreel MA, Niinomi M. Biocompatibility of Ti-alloys for long-term implantation. *J Mech Behav Biomed Mater*. 2013;20:407-415. doi:10.1016/j.jmbbm.2012.11.014

19. Goatman, Irena Ph D. Characteristics of Metals Used in Implants. 1997;11(6):383-389.

20. Köse N. Biological Response to Orthopedic Implants and Biomaterials. *Musculoskelet Res Basic Sci*. 2016:3-14. doi:10.1007/978-3-319-20777-3

21. Eglin D, Alini M. DEGRADABLE POLYMERIC MATERIALS FOR OSTEOSYNTHESIS : TUTORIAL. 2008;16:80-91. doi:10.22203/eCM.v016a09

22. Chen Q, Thouas GA. Metallic implant biomaterials. *Mater Sci Eng R*. 2015;87:1-57. doi:10.1016/j.mser.2014.10.001

23. Ontakis GMK, Agkalos JEP, Osounidis TIT, Elissas JM, Atonis PK. Bioabsorbable materials in orthopaedics. 2007;73:159-169.

24. Field JR. Bone Plate Fixation : Its Relationship with Implant Induced Osteoporosis. 2016;(April 1997). doi:10.1055/s-0038-1632576

25. Long PH. Medical Devices in Orthopedic Applications. *Toxicol Pathol*. 2008:85-91. doi:10.1177/0192623307310951

26. Azevedo CRF, Hippert E. Failure analysis of surgical implants in Brazil. *Eng Fail Anal*. 2002;9(6):621-633. doi:10.1016/S1350-6307(02)00026-2

27. Aksakal B, Yildirim ÖS, Gul H. Metallurgical Failure Analysis of Various Implant Materials Used in Orthopedic Applications. *J Fail Anal Prev*. 2004;4(3):17-23. doi:10.1361/15477020419794

28. Geringer J, Forest B, Combrade P. Wear analysis of materials used as orthopaedic implants. *Wear*. 2006;261(9):971-979. doi:10.1016/j.wear.2006.03.022

29. Hallab NJ, Jacobs JJ. Biologic effects of implant debris. *Bull NYU Hosp Jt Dis*. 2009;67(2):182-188. http://www.ncbi.nlm.nih.gov/pubmed/19583551.

30. Balamurugan A, Rajeswari S, Balossier G. Corrosion aspects of metallic implants — An overview. 2008;(October 2018). doi:10.1002/maco.200804173

31. Maurus PB, Kaeding CC. Bioabsorbable Implant Material Review. 2004:158-160. doi:10.1053/j.otsm.2004.07.015

32. Kadir DM, State K, Hospital S, Ilorin S, Ibraheem G. Removal of Orthopaedic Hardware : A 5 year Review. 2013;(December).

33. Vieira AC, Vieira JC, Ferra JM, Magalhães FD, Guedes RM, Marques AT. Mechanical Study of PLA-PCL Fibers during In Vitro Degradation.

34. Athanasiou KA, Niederauer GG, Agrawal CM. Sterilization, toxicity, biocompatibility and clinical applications of polylactic acid / polyglycolic acid copolymers. *Biomaterials*. 1996;17(2).

35. Vert M, Mauduit J, Li S. Biodegradation of PLA / GA polymers : increasing complexity. 1994;15(15):1209-1213.

36. Rezwan K, Chen QZ, Blaker JJ, Roberto A. Biodegradable and bioactive porous polymer / inorganic composite scaffolds for bone tissue engineering. 2006;27:3413-3431. doi:10.1016/j.biomaterials.2006.01.039

37. Suming Li. Hydrolytic degradation characteristics of aliphatic polyesters derived from lactic and glycolic acids Article. 1998;(april). doi:10.1002/(SICI)1097-4636(1999)48

38. Jorfi M, Foster EJ. Recent advances in nanocellulose for biomedical applications. 2015;41719:1-19. doi:10.1002/app.41719

39. Dufresne A. 1. Cellulose and potential reinforcement. In: *Nanocellulose: From Nature to High Performance Tailored Materials*. 2nd ed. De Gruyter; 2017:1-46. doi:10.1515/9783110480412-002

40. Hossen MR, Dadoo N, Holomakoff DG, Co A, Gramlich WM, Mason MD. Wet stable and mechanically robust cellulose nano fi brils (CNF) based hydrogel. *Polymer (Guildf)*. 2018;151:231-241. doi:10.1016/j.polymer.2018.07.016

41. Lin N, Dufresne A. Nanocellulose in biomedicine : Current status and future prospect. *Eur Polym J*. 2014;59:302-325. doi:10.1016/j.eurpolymj.2014.07.025

42. Eatemadi A, Daraee H, Zarghami N, Yar HM, Akbarzadeh A. Nanofiber: Synthesis and biomedical applications. *Artif Cells, Nanomedicine Biotechnol*. 2016;44(1):111-121. doi:10.3109/21691401.2014.922568

43. Nechyporchuk O, Belgacem MN, Bras J. Production of cellulose nanofibrils: A review of recent advances. *Ind Crops Prod*. 2016;93:2-25. doi:10.1016/j.indcrop.2016.02.016

44. Parenteau-bareil R, Gauvin R, Berthod F. Collagen-Based Biomaterials for Tissue Engineering Applications. 2010:1863-1887. doi:10.3390/ma3031863

45. Siqueira P, Siqueira É Der, Lima AE De, et al. Three-Dimensional Stable Alginate-Nanocellulose Gels for Biomedical Applications : Towards Tunable Mechanical Properties and Cell Growing. 2019:1-22. doi:10.3390/nano9010078

46. Yong K, Mooney DJ. Progress in Polymer Science Alginate : Properties and biomedical applications. *Prog Polym Sci*. 2012;37(1):106-126. doi:10.1016/j.progpolymsci.2011.06.003

47. Martins M, Barros AA, Quraishi S, et al. The Journal of Supercritical Fluids Preparation of macroporous alginate-based aerogels for biomedical applications. *J Supercrit Fluids*. 2015;106:152-159. doi:10.1016/j.supflu.2015.05.010

48. Jayakumar R, Menon D, Manzoor K, Nair S V, Tamura H. Biomedical applications of chitin and chitosan based nanomaterials — A short review. *Carbohydr Polym*. 2010;82(2):227-232. doi:10.1016/j.carbpol.2010.04.074

49. Anitha A, Sowmya S, Kumar PTS, et al. Progress in Polymer Science Chitin and chitosan in selected biomedical applications. *Prog Polym Sci*. 2014;39(9):1644-1667. doi:10.1016/j.progpolymsci.2014.02.008

50. Jayakumar R, Prabaharan M, Nair S V, Tamura H. Novel chitin and chitosan nano fibers in biomedical applications. *Biotechnol Adv*. 2010;28(1):142-150. doi:10.1016/j.biotechadv.2009.11.001

51. Holomakoff DG. NANOCELLULOSE FIBERS AS A POTENTIAL MATERIAL FOR ORTHOPEDIC IMPLANTATION APPLICATION By. 2017;(August).

52. Mason MD, Holomakoff DG, Hossen MR. CONTROLLED POROSITY STRUCTURAL MATERIAL WITH NANOCELLULOSE FIBERS. 2017;(12). https://patents.google.com/patent/WO2017165465A1/en?q=bone&oq=nanocellulose+bone.

53. Rodríguez K, Sundberg J, Gatenholm P, Renneckar S. Electrospun nanofibrous cellulose scaffolds with controlled microarchitecture. *Carbohydr Polym*. 2014;100:143-149. doi:10.1016/j.carbpol.2012.12.037

54. Alexandrescu L, Syverud K, Chinga-carrasco AGG. Cytotoxicity tests of cellulose nanofibril-based structures. 2013:1765-1775. doi:10.1007/s10570-013-9948-9

55. Bhattacharya M, Malinen MM, Lauren P, et al. Nano fi brillar cellulose hydrogel promotes three-dimensional liver cell culture. 2012;164:291-298. doi:10.1016/j.jconrel.2012.06.039

56. Babes L, Jacques J, Jeune L, Jallet P. Synthesis of Iron Oxide Nanoparticles Used as MRI Contrast Agents : A Parametric Study. 1999;482:474-482.

57. Kumar A, Gupta M. Synthesis and surface engineering of iron oxide nanoparticles for biomedical applications. 2005;26:3995-4021. doi:10.1016/j.biomaterials.2004.10.012

58. Amstad E, Reimhult E. Nanoscale Stabilization and functionalization of iron oxide nanoparticles for biomedical. 2011:2819-2843. doi:10.1039/c1nr10173k

59. Kunz PC, Meyer H, Barthel J, Sollazzo S, Schmidt AM. Electronic Supplementary Information (ESI) for Metal carbonyls supported on iron oxide nanoparticles to trigger the CO-gasotransmitter release by magnetic heating. 2013;98(1997):1-14.

60. Baalousha M. Aggregation and disaggregation of iron oxide nanoparticles : Influence of particle concentration , pH and natural organic matter. *Sci Total Environ*. 2008;407(6):2093-2101. doi:10.1016/j.scitotenv.2008.11.022

61. Schindelin J, Arganda-carreras I, Frise E, et al. Fiji : an open-source platform for biological-image analysis. 2019;9(7). doi:10.1038/nmeth.2019

62. Standard Specification and Test Method for Metallic Bone Plates 1. *ASTM B Stand*. 2017:1-12. doi:10.1520/F0382-17.Copyright

63. AMERICAN SOCIETY FOR TESTING AND MATERIALS. ASTM D790 − 17 - Flexural Properties of Unreinforced and Reinforced Plastics and Electrical Insulating Materials. *Annu B ASTM Stand*. 2017:12. doi:10.1520/D0790-17.2

64. November R. Engineering of Carbonate Apatite Bone Substitute Based on Composition-Transformation of Gypsum and Calcium Hydroxide. 2010;2010(May):344-352. doi:10.4236/eng.2010.25045

65. Tan L, Yu X, Wan P, Yang K. Biodegradable Materials for Bone Repairs : A Review. *J Mater Sci Technol*. 2013;29(6):503-513. doi:10.1016/j.jmst.2013.03.002

66. Ratnayake JTB, Gould ML, Shavandi A, Mucalo M, Dias GJ. Development and characterization of a xenograft material from New Zealand sourced bovine cancellous bone. 2016:1054-1062. doi:10.1002/jbm.b.33644

67. Suchanek WL, Shuk P, Byrappa K, Riman RE, Tenhuisen KS, Janas VF. Mechanochemical – hydrothermal synthesis of carbonated apatite powders at room temperature. 2002;23:699-710.

68. Giles R. Scuderi MD, Alfred J. Tria JMD. *Knee Arthroplasty Handbook Techniques in Total Knee and Revision Arthroplasty*.; 2006.

69. Tang Z, Li X, Tan Y, Fan H. The material and biological characteristics of osteoinductive calcium phosphate ceramics. 2018;(September 2017):43-59. doi:10.1093/rb/rbx024

70. Boutinguiza M, Pou J, Comesaña R, Lusquiños F, Carlos A De, León B. Biological hydroxyapatite obtained from fi sh bones. *Mater Sci Eng C*. 2012;32(3):478-486. doi:10.1016/j.msec.2011.11.021

71. Lee S, Balázsi C, Balázsi K, et al. ｜ Original Article ｜ Comparative Study of Hydroxyapatite Prepared from Seashells and Eggshells as a Bone Graft Material. 2014;11(2):113-120. doi:10.1007/s13770-014-0056-1

72. Johnson GS, Mucalo MR. The processing and characterization of animal- derived bone to yield materials with biomedical applications Part 1 : Modifiable porous implants from bovine condyle cancellous bone and characterization of bone materials as a function of processing. 2000;1:427-441.

73. Dorozhkin S V. Calcium orthophosphate-based biocomposites and hybrid biomaterials. 2009:2343-2387. doi:10.1007/s10853-008-3124-x

74. Zakaria SM, Hussein S, Zein S, Othman MR, Yang F, Jansen JA. Nanophase Hydroxyapatite as a Biomaterial in Advanced Hard Tissue Engineering : A Review. 2013;19(5). doi:10.1089/ten.teb.2012.0624

75. Geng Z, Yuan Q, Zhuo X, Li Z, Cui Z, Zhu S. Synthesis , Characterization , and Biological Evaluation of Nanostructured Hydroxyapatite with Different Dimensions. 10:1-13. doi:10.3390/nano7020038

76. Kong LB, Ma J, Boey F. Nanosized hydroxyapatite powders derived from coprecipitation process. 2002;7:1131-1134.

77. Fathi MH, Hanifi A. Evaluation and characterization of nanostructure hydroxyapatite powder prepared by simple sol – gel method. 2007;61:3978-3983. doi:10.1016/j.matlet.2007.01.028

78. Sadat-shojai M, Khorasani M, Jamshidi A. Hydrothermal processing of hydroxyapatite nanoparticles — A Taguchi experimental design approach. *J Cryst Growth*. 2012;361:73-84. doi:10.1016/j.jcrysgro.2012.09.010

79. Jamie Y, Chye S, Loo J, Lee J, Ma J. Investigation of the bioactivity and biocompatibility of different glass interfaces with hydroxyapatite , fluorohydroxyapatite and 58S bioactive glass. 2007;30:205-216.

80. Liu HS, Chin TS, Lai LS, et al. Hydroxyapatite Synthesized by a Simplified Hydrothermal Method. 1997;8842(95):19-25.

81. Poinern GJ, Brundavanam R, Le XT, Djordjevic S, Prokic M, Fawcett D. Thermal and ultrasonic influence in the formation of nanometer scale hydroxyapatite bio-ceramic. *Int J Nanomedicine*. 2011;6:2083-2095.

82. Giraldo-Betancur AL, Espinosa-Arbelaez DG, Del Real-López A, et al. Comparison of physicochemical properties of bio and commercial hydroxyapatite. *Curr Appl Phys*. 2013;13(7):1383-1390. doi:10.1016/j.cap.2013.04.019

83. Walters MA, Lang YC, Blumenthal NC, Legeros RZ, Konsker ILA. A Raman and Infrared Spectroscopic Investigation of Biological Hydroxyapatite. 200(1990):193-200.

84. Kotake N, Kuboki M, Kiya S, Kanda Y. Influence of dry and wet grinding conditions on fineness and shape of particle size distribution of product in a ball mill. *Adv Powder Technol*. 2011;22(1):86-92. doi:10.1016/j.apt.2010.03.015

85. Malina D, Biernat K, Sobczak-Kupiec A. Studies on sintering process of synthetic hydroxyapatite. *Acta Biochim Pol*. 2013;60(4):851-855.

BIOGRAPHY OF THE AUTHOR

Mitchell Chesley was born in Waterville January 1st, 1995. He graduated from Gardiner Area High School spring of 2013, before continuing on for a Batcheler's in Bioengineering at the University of Maine. In spring of 2017 he graduated from the University of Maine with his Batcheler's in Bioengineering and proceeded work on campus with the Mason lab as a Research specialist. In spring of 2018 he began his graduate careers in biomedical engineering at the University of Maine. Mitchell is a candidate for the Master of Science degree in Biomedical Engineering from the University of Maine in August of 2019.